

Jordan Journal of Mechanical and Industrial Engineering (JJMIE)

JJMIE is a high-quality scientific journal devoted to fields of Mechanical and Industrial Engineering. It is published by the Hashemite University in corporation with the Jordanian Scientific Research Support Fund.

EDITORIAL BOARD

Editor-in-Chief

Prof. Mousa S. Mohsen

Editorial board

Prof. Bilal A. Akash
Hashemite University

Prof. Adnan Z. Al-Kilany
University of Jordan

Prof. Ayman A. Al-Maaitah
Mutah University

Prof. Moh'd A. Al-Nimr
Jordan University of Science and Technology

Prof. Ali A. Badran
University of Jordan

Prof. Naseem M. Sawaqed
Mutah University

Assistant Editor

Dr. Ahmad Al-Ghandoor
Hashemite University

THE INTERNATIONAL ADVISORY BOARD

Abu-Qudais, Mohammad
Jordan University of Science & Technology, Jordan

Abu-Mulaweh, Hosni
Purdue University at Fort Wayne, USA

Afaneh Abdul-Hafiz
Robert Bosch Corporation, USA

Afonso, Maria Dina
Institute Superior Tecnico, Portugal

Badiru, Adedji B.
The University of Tennessee, USA

Bejan, Adrian
Duke University, USA

Chalhoub, Nabil G.
Wayne State University, USA

Cho, Kyu-Kab
Pusan National University, South Korea

Dincer, Ibrahim
University of Ontario Institute of Technology, Canada

Douglas, Roy
Queen's University, U. K

El Bassam, Nasir
International Research Center for Renewable Energy,
Germany

Haik, Yousef
United Arab Emirates University, UAE

Jaber, Jamal
Al- Balqa Applied University, Jordan

Jubran, Bassam
Ryerson University, Canada

Kakac, Sadik
University of Miami, USA

Khalil, Essam-Eddin
Cairo University, Egypt

Mutoh, Yoshiharu
Nagaoka University of Technology, Japan

Pant, Durbin
Iowa State University, USA

Riffat, Saffa
The University of Nottingham, U. K

Saghir, Ziad
Ryerson University, Canada

Sarkar, MD. Abdur Rashid
Bangladesh University of
Engineering & Technology, Bangladesh

Siginer, Dennis
Wichita State University, USA

Sopian, Kamaruzzaman
University Kebangsaan Malaysia, Malaysia

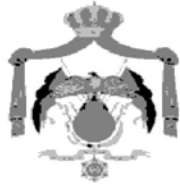
Tzou, Gow-Yi
Yung-Ta Institute of Technology and
Commerce, Taiwan

EDITORIAL BOARD SUPPORT TEAM

Language Editor Publishing Layout
Dr. Abdullah Jaradat MCPD. Osama AlShareet

SUBMISSION ADDRESS:

Prof. Mousa S. Mohsen, Editor-in-Chief
Jordan Journal of Mechanical & Industrial Engineering,
Hashemite University, PO Box 330127, Zarqa, 13133, Jordan
E-mail: jjmie@hu.edu.jo



Hashemite Kingdom of Jordan



Hashemite University

Jordan Journal of
Mechanical and Industrial Engineering

JJMIIE

An International Peer-Reviewed Scientific Journal

<http://jjmie.hu.edu.jo/>

ISSN 1995-6665

Jordan Journal of Mechanical and Industrial Engineering (JJMIE)

JJMIE is a high-quality scientific journal devoted to fields of Mechanical and Industrial Engineering. It is published by the Hashemite University in corporation with the Jordanian Scientific Research Support Fund.

Introduction: The Editorial Board is very committed to build the Journal as one of the leading international journals in mechanical and industrial engineering sciences in the next few years. With the support of the Ministry of Higher Education and Scientific Research and Jordanian Universities, it is expected that a heavy resource to be channeled into the Journal to establish its international reputation. The Journal's reputation will be enhanced from arrangements with several organizers of international conferences in publishing selected best papers of the conference proceedings.

Aims and Scope: Jordan Journal of Mechanical and Industrial Engineering (JJMIE) is a refereed international journal to be of interest and use to all those concerned with research in various fields of, or closely related to, mechanical and industrial engineering disciplines. Jordan Journal of Mechanical and Industrial Engineering aims to provide a highly readable and valuable addition to the literature which will serve as an indispensable reference tool for years to come. The coverage of the journal includes all new theoretical and experimental findings in the fields of mechanical and industrial engineering or any closely related fields. The journal also encourages the submission of critical review articles covering advances in recent research of such fields as well as technical notes.

Guide for Authors

Manuscript Submission

High-quality submissions to this new journal are welcome now and manuscripts may be either submitted online or mail.

Online: For online submission upload one copy of the full paper including graphics and all figures at the online submission site, accessed via E-mail: jjmie@hu.edu.jo. The manuscript must be written in MS Word Format. All correspondence, including notification of the Editor's decision and requests for revision, takes place by e-mail and via the Author's homepage, removing the need for a hard-copy paper trail.

By Mail: Manuscripts (1 original and 3 copies) accompanied by a covering letter may be sent to the Editor-in-Chief. However, a copy of the original manuscript, including original figures, and the electronic files should be sent to the Editor-in-Chief. Authors should also submit electronic files on disk (one disk for text material and a separate disk for graphics), retaining a backup copy for reference and safety.

Note that contributions may be either submitted online or sent by mail. Please do NOT submit via both routes. This will cause confusion and may lead to delay in article publication. Online submission is preferred.

Submission address and contact:

Prof. **Mousa S. Mohsen**, Editor-in-Chief
Jordan Journal of Mechanical & Industrial Engineering,
Hashemite University,
PO Box 330127, Zarqa, 13133 , Jordan
E-mail: jjmie@hu.edu.jo

Types of contributions: Original research papers

Corresponding author: Clearly indicate who is responsible for correspondence at all stages of refereeing and publication, including post-publication. Ensure that telephone and fax numbers (with country and area code) are provided in addition to the e-mail address and the complete postal address. Full postal addresses must be given for all co-authors.

Original material: Submission of an article implies that the work described has not been published previously (except in the form of an abstract or as part of a published lecture or academic thesis), that it is not under consideration for publication elsewhere, that its publication is approved by all authors and that, if accepted, it will not be published elsewhere in the same form, in English or in any other language, without the written consent of the Publisher. Authors found to be deliberately contravening the submission guidelines on originality and exclusivity shall not be considered for future publication in this journal.

Supplying Final Accepted Text on Disk: If online submission is not possible: Once the paper has been accepted by the editor, an electronic version of the text should be submitted together with the final hardcopy of the manuscript. The electronic version must match the hardcopy exactly. We accept MS Word format only. Always keep a backup copy of the electronic file for reference and safety. Label the disk with your name. Electronic files can be stored on CD.

Notification: Authors will be notified of the acceptance of their paper by the editor. The Publisher will also send a notification of receipt of the paper in production.

Copyright: All authors must sign the Transfer of Copyright agreement before the article can be published. This transfer agreement enables Jordan Journal of Mechanical and Industrial Engineering to protect the copyrighted material for the authors, but does not relinquish the authors' proprietary rights. The copyright transfer covers the exclusive rights to reproduce and distribute the article, including reprints, photographic reproductions, microfilm or any other reproductions of similar nature and translations.

PDF Proofs: One set of page proofs in PDF format will be sent by e-mail to the corresponding author, to be checked for typesetting/editing. The corrections should be returned within 48 hours. No changes in, or additions to, the accepted (and subsequently edited) manuscript will be allowed at this stage. Proofreading is solely the author's responsibility. Any queries should be answered in full. Please correct factual errors only, or errors introduced by typesetting. Please note that once your paper has been proofed we publish the identical paper online as in print.

Author Benefits

Page charge: Publication in this journal is free of charge.

Free off-prints: Three journal issues of which the article appears in along with twenty-five off-prints will be supplied free of charge to the corresponding author. Corresponding authors will be given the choice to buy extra off-prints before printing of the article.

Manuscript Preparation:

General: Editors reserve the right to adjust style to certain standards of uniformity. Original manuscripts are discarded after publication unless the Publisher is asked to return original material after use. If online submission is not possible, an electronic copy of the manuscript on disk should accompany the final accepted hardcopy version. Please use MS Word for the text of your manuscript.

Structure: Follow this order when typing manuscripts: Title, Authors, Affiliations, Abstract, Keywords, Introduction, Main text, Conclusions, Acknowledgements, Appendix, References, Figure Captions, Figures and then Tables. For submission in hardcopy, do not import figures into the text - see Illustrations. For online submission, please supply figures imported into the text AND also separately as original graphics files. Collate acknowledgements in a separate section at the end of the article and do not include them on the title page, as a footnote to the title or otherwise.

Text Layout: Use double spacing and wide (3 cm) margins. Ensure that each new paragraph is clearly indicated. Present tables and figure legends on separate pages at the end of the manuscript. If possible, consult a recent issue of the journal to become familiar with layout and conventions. All footnotes (except for table and corresponding author footnotes) should be identified with superscript Arabic numbers. To conserve space, authors are requested to mark the less important parts of the paper (such as records of experimental results) for printing in smaller type. For long papers (more than 4000 words) sections which could be deleted without destroying either the sense or the continuity of the paper should be indicated as a guide for the editor. Nomenclature should conform to that most frequently used in the scientific field concerned. Number all pages consecutively; use 12 or 10 pt font size and standard fonts. If submitting in hardcopy, print the entire manuscript on one side of the paper only.

Corresponding author: Clearly indicate who is responsible for correspondence at all stages of refereeing and publication, including post-publication. The corresponding author should be identified with an asterisk and footnote. Ensure that telephone and fax numbers (with country and area code) are provided in addition to the e-mail address and the complete postal address. Full postal addresses must be given for all co-authors. Please consult a recent journal paper for style if possible.

Abstract: A self-contained abstract outlining in a single paragraph the aims, scope and conclusions of the paper must be supplied.

Keywords: Immediately after the abstract, provide a maximum of six keywords (avoid, for example, 'and', 'of'). Be sparing with abbreviations: only abbreviations firmly established in the field may be eligible.

Symbols: All Greek letters and unusual symbols should be identified by name in the margin, the first time they are used.

Units: Follow internationally accepted rules and conventions: use the international system of units (SI). If other quantities are mentioned, give their equivalent in SI.

Maths: Number consecutively any equations that have to be displayed separately from the text (if referred to explicitly in the text).

References: All publications cited in the text should be presented in a list of references following the text of the manuscript.

Text: Indicate references by number(s) in square brackets in line with the text. The actual authors can be referred to, but the reference number(s) must always be given.

List: Number the references (numbers in square brackets) in the list in the order in which they appear in the text.

Examples:

Reference to a journal publication:

- [1] M.S. Mohsen, B.A. Akash, "Evaluation of domestic solar water heating system in Jordan using analytic hierarchy process". Energy Conversion & Management, Vol. 38, No. 9, 1997, 1815-1822.

Reference to a book:

- [2] Strunk Jr W, White EB. The elements of style. 3rd ed. New York: Macmillan; 1979.

Reference to a conference proceeding:

- [3] B. Akash, S. Odeh, S. Nijmeh, "Modeling of solar-assisted double-tube evaporator heat pump system under local climate conditions". 5th Jordanian International Mechanical Engineering Conference, Amman, Jordan, 2004.

Reference to a chapter in an edited book:

- [4] Mettam GR, Adams LB. How to prepare an electronic version of your article. In: Jones BS, Smith RZ, editors. Introduction to the electronic age, New York: E-Publishing Inc; 1999, p. 281-304

Free Online Color: If, together with your accepted article, you submit usable color and black/white figures then the journal will ensure that these figures will appear in color on the journal website electronic version.

Tables: Tables should be numbered consecutively and given suitable captions and each table should begin on a new page. No vertical rules should be used. Tables should not unnecessarily duplicate results presented elsewhere in the manuscript (for example, in graphs). Footnotes to tables should be typed below the table and should be referred to by superscript lowercase letters.

PAGES	PAPERS
113 – 118	Declination of the Aggregate Energy Intensity of the Jordanian Industrial Sector Between Years 1998 and 2005 <i>A. Al-Ghandoor, I. Al-Hinti</i>
119 – 128	Inverse Design of Impeller Blade of Centrifugal Pump with a Singularity Method <i>Wen-Guang LI</i>
129 – 132	CFD Simulations of Drag and Separation Flow Around Ellipsoids <i>Yazan Taamneh</i>
133 – 138	Mhd Heat and Mass Transfer Free Convection Flow Near the Lower Stagnation Point of an Isothermal Cylinder Imbedded in Porous Domain with the Presence of Radiation <i>Ziya Uddin , Manoj Kumar</i>
139 - 144	A Correlation for the Prediction of Nucleate Pool Boiling Performance of Pure Liquids from Enhanced Tubes <i>Ali H. Tarrad</i>
145 – 148	Fabrication and Analysis of Valve-less Micro-pumps <i>Shireen Al-Hourani , Mohammad N. Hamdan , Ahmad A. Al-Qaisia , “Moh’d Sami” Ashhab</i>
149 – 160	Economic Design of Joint \bar{X} and R Control Charts Using Differential Evolution <i>Rukmini V. Kasarapu, Vijaya B. Vommi</i>
161 – 166	Main Factors Causing Workers Turnover in Jordan Industrial Sector <i>Wisam M. Abu Jadayil</i>
167 - 176	Computer Aided Design Tools in the Development of Surface Micromachined Mechanisms <i>Mohammad I. Kilani</i>
177 - 184	Exploration Algorithm Technique for Multi-Robot Collaboration <i>Mohammad Al-Khawaldah , Omar Badran and Ibrahim Al-Adwan</i>
185 - 192	A Hybrid Power-plant System To Reduce Carbon Emissions <i>Munzer S. Y. Ebaid , Mohamad Y. Mustafa</i>
193 – 196	Decision Making Using Multiple Rates of Return: An Alternative Approach <i>Ahmad Jaradat , Khaldoun K. Tahboubb</i>

Declination of the Aggregate Energy Intensity of the Jordanian Industrial Sector Between Years 1998 and 2005

A. Al-Ghandoor^{*,a}, I. Al-Hinti^b

^a Department of Industrial Engineering, The Hashemite University, Zarqa, Jordan

^b Department of Mechatronics Engineering, German Jordanian University, Amman, Jordan

Abstract

This paper uses the refined Laspeyers method decomposition technique to explain factors that impact aggregate energy intensity in the Jordanian industrial sector during the period 1998-2005. This kind of study is useful to evaluate the past and predict the future trends for energy-policy evaluation. The Jordanian industrial aggregate energy intensity has decreased from approximately 40.6 to 25.7 MJ/US\$ in 1998 and 2005, respectively. The analysis showed that the efficiency and structural effects contribute to decreases of around 33 and 67% respectively of total aggregate energy intensity decline in the industrial sector.

© 2011 Jordan Journal of Mechanical and Industrial Engineering. All rights reserved

Keywords: Decomposition; Laspeyers index; Jordan, Energy; Efficiency; Structural; Intensity.

1. Introduction

Jordan, which is a relatively small country of about 5.6 million inhabitants, lies in the heart of the Middle East. It is among the low income countries of the region with an average GDP per capita of about US\$ 2550 in 2006, compared to US\$ 10,000–18,000 for neighboring oil exporting Arab Gulf States [1,2]. The country suffers from an ever-present lack of sufficient supplies of natural resources including water, minerals, crude oil and natural gas. Being a non-oil producing country, there has been an increasing anxiety about energy consumption and its harmful impact on the national economy as well as local environment. At present, Jordan depends profoundly on imported crude oil and natural gas from neighboring Arab countries as main sources of energy which causes a drain of scarce hard currency. The annual energy bill has been hurriedly escalating over the past few years and exceeded US\$ 3 billion in year 2006 due to high rates of population and economic growth combined with the successive increase in oil price.

The industrial sector's aggregate energy intensity, defined here as energy consumption divided by the value added output¹ (MJ/\$), is a key parameter for describing industrial energy efficiency. Decomposition techniques have been conducted extensively to better understand the

historical variations in energy use. Extensive research has been conducted to better understand the historical variations in aggregate energy intensity, and two main factors have been identified [3-5]: changes in the structure of production output over time (i.e. structural effect), and changes in energy efficiencies of individual industries (i.e. efficiency effect, also referred to as the intensity effect in some literature)². The impact of the structural effect on aggregate energy intensity and aggregate energy use has been an important subject of research since 1978 [6].

Numerous decomposition studies have been widely used since the early 1980s to decompose the aggregate energy intensity changes into structural, and efficiency effects. Also, the decomposition analysis has been used to decompose the energy consumption changes into production, structural, and efficiency effect. This analysis has been utilized in different countries: Sweden [7]; United Kingdom [8]; Canada [9]; China [10-11]; Spain [12]; Thailand [13]; Turkey [14]; USA [15]. Related literature can be found in [16-19]. This technique is based on economic index numbers; over one hundred of such indexes have been described by Economic index numbers by [20]. Comparisons and linkages between decomposition methods and economic index numbers can be found in literature [21, 4]. Also, decomposition analysis can be used to study the effect of economic growth and vehicle

* Corresponding author: gandoor2002@yahoo.com.

¹ Value added has been deflated and expressed in 1999 constant dollars, and so value added output refers to 1999 constant dollar value added

² Aggregate energy intensity and energy intensity are different terms. Aggregate energy intensity refers to the total energy consumption divided by the total value added output of all industries within the industrial sector, while energy intensity, on the other hand, is the energy consumption divided by the value added output of each industry within the industrial sector. To avoid confusion, energy efficiency and efficiency effect will refer to energy intensity and intensity effect, respectively. If energy intensity decreases, this means that energy efficiency increases and vice versa.

ownership on transportation carbon dioxide emission and energy consumption [22].

In Jordan, there are several studies that analyzed current and future energy requirements for different sectors and industries [23-27]; however, few decomposition studies have been reported recently in Jordan. While the previous papers conducted by the authors [28-29] were concerned with the electricity intensity and did not take into consideration the fuel consumption in the Jordanian industrial sector, in this paper, the Laspeyers approach decomposition technique is applied to examine the role of structural, and efficiency effects that impact the Jordanian industrial aggregate energy intensity (both fuel and electricity) during the period from 1998 to 2005. Between these years, there was rapid growth in the demand for energy in the Jordanian industries, led by strong growth in industrial activity and increasing penetrations of new facilities that are occupied with new technologies. This kind of research is useful for analysts and policy makers concerned with energy issues in Jordan, especially those interested in future directions of energy demand in Jordan.

The paper is organized as follows: the next section describes the energy consumption in Jordan; section 3 briefs the various data sources utilized in this study; section 4 presents the descriptive analysis of the industrial energy demand and its relation with the economic growth; section 5 demonstrates the analysis using refined Laspeyers decomposition technique; and sections 6 and 7 display the results and the concluding remarks, respectively.

2. Energy consumption in Jordan

In 2006, the total primary and final energy consumption were about 7.2×10^6 and 4.9×10^6 ton oil equivalent (toe), respectively. The second largest consumer, after transportation, is the industrial sector with a contribution ratio of about one quarter of total energy available for all consumers, as shown in Figure 1 [30]. The rate of energy consumption, especially electricity, is rising rapidly due to the high growth rate of population and urbanization.

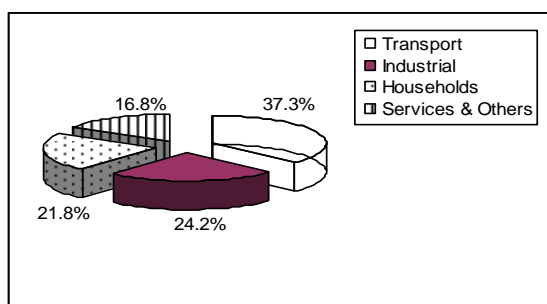


Figure 1. Distribution of final energy consumption in 2006.

3. Data sources and basic assumptions

This study examines and carefully distinguishes between the *site* and *embodied* energy content of electricity. The embodied energy value accounts for the generation and transmission energy losses associated with electricity production, while the site electricity value

includes only the site heat value of electricity (3,600 kJ/kWh). Electricity used in the manufacturing sector mainly originates from two sources: purchased electricity and electricity produced onsite. In this paper, the heat rate of the electricity is defined as the ratio of the site energy content of electricity produced to the total energy content of fuel input used to produce it. The heat rate of the electricity depends on the generation technology mix used to provide the electricity to the manufacturing sector and has been estimated by as 34%. In this study, the embodied energy has been used for the analyses between years 1998 and 2005. All data were retrieved from various years of Jordan's statistical yearbooks as published by different governmental agencies. The focus on this time frame largely reflects the availability of data as required for the purposes of this study. Due to data availability constraint, the Jordanian industrial sector was disaggregated into seven sub-sectors; namely, mining of chemical and fertilizer minerals, paper, plastics, petroleum, cement, iron and steel, and others industries³.

It is worthwhile mentioning here that all disaggregated physical energy quantities in a specific period for all Jordanian industries were calculated by converting the monetary values (which are the only available sources of energy data) of each energy source to its corresponding physical value by using the average fuel price in that period. The energy values used in this study are the summation of fuel energy and the embodied energy of electricity. The source of information for the annual energy consumption is the Jordanian National Electric Power Company [31] and the Department of Statistics [32]. Production output is based on the value added as reported by the Jordan Chamber of Industry and Department of Statistics [32]. Value added represents the unique contribution to the production of a finished product/commodity. Use of this value avoids the issue of 'double counting' when a commodity produced by one industry is used as an input for another industry. A change in the value added from one year to another includes an increase (or decrease) in price resulting from inflation or deflation; such changes do not reflect a change in output. Therefore, before using estimates of the values added as an output measure, they were adjusted for the effect of changes in price using the producer price index (as reported in year 1999) obtained from the Department of Statistics [33].

4. General picture of Jordanian industrial growth and energy demand

Before applying the decomposition technique, a graphic analysis of energy consumption, industrial

³ This disaggregation level is justified since the mining of chemical and fertilizer minerals, paper, plastics, petroleum, cement, and iron and steel sub-sectors are the main intensive industries in Jordan. In 2005, they contributed to about 70% of total energy demand. The "Other" industries include food, tobacco, textiles, wearing apparel, tanning and dressing of leather, wood, publishing and printing media, chemicals, fabricated metals, machinery, transportation, and furniture industries. These industries were grouped together since no individual data is available for each of them and such industries can be considered as electricity non-intensive industries.

As can be seen from Table 2, all types of industries have annual growth of energy use smaller than the annual growth of production output shown in Table 1. This simply means that all industries gained improvement in energy efficiency over the study period and therefore, a general conclusion that can be drawn here is that there was a significant energy efficiency improvement during the 1998-2005 period. Again, this table demonstrates that the role of energy intensive industries has decreased as can be seen from the decrease in energy demand shares for mining of chemicals and fertilizer minerals, and petroleum industries.

But it should be noted that increased prices of energy and increased rates of production the country witnessed during this period would lead to lower ratios of specific energy consumption per final unit produced, i.e. less losses, due to increased awareness and capacity utilization factors. As a result a general conclusion that can be drawn here is that there was a significant improvement in energy utilization efficiency during the period 1998-2005.

4.3. Aggregate energy intensity variation

From the previous data and analysis, one can foresee that aggregate energy intensity should decline during the study period 1998-2005, since the annual growth of energy is less than the annual growth of the Jordanian industrial production output. Figure 4 shows the aggregate energy intensity of the Jordanian industrial sector during the study period. As can be seen from this figure, aggregate energy intensity has decreased from 40.6 MJ/\$ in 1998 to 25.7 MJ/\$ in 2005 at an average decline of 5.24%yr⁻¹. Although the previous analysis and data give some indications of the factors that result in aggregate energy intensity reduction, however, a method to quantify these factors is still needed; the purpose of this study is to quantify and explain the factors affecting this variation. This will be explained in the following section.

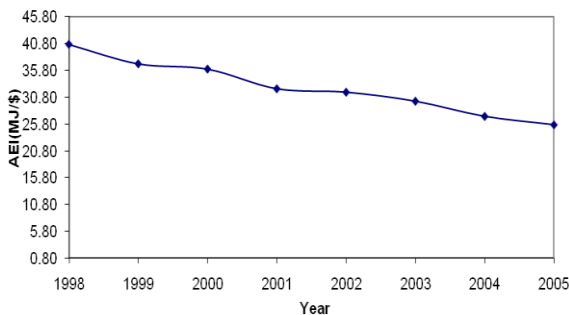


Figure 4. Aggregate energy intensity (AEI) of the Jordanian industrial sector

5. Methodology

The methodology adopted in this study has been used before in [34]. This method of decomposition results in no residual, meaning that it is able to explain all of the changes in the aggregate energy intensity decomposed. Before introducing this method, it is necessary to define the two factors that will be investigated in this study; namely, the structural and efficiency factors. Structural factor is a measure of production shift from/to energy intensive to/from energy non intensive industries while the

efficiency factor is an indication of the amount of energy used per unit of constant value added of individual industries. Decreases in energy intensities mean improvement in energy efficiency and vice versa. Improvement in energy efficiency is associated with the technical characteristics of the equipment being run, including fans, compressors, electric furnaces, etc.

The total change in industrial aggregate energy intensity between T and 0 years can be expressed as follows:

$$(\Delta I_{TOT})_{0,T} = (\Delta I_{STR})_{0,T} + (\Delta I_{EFF})_{0,T} \quad (1)$$

$$(\Delta I_{TOT})_{0,T} = (I_{TOT})_T - (I_{TOT})_0 \quad (2)$$

$$(I_{TOT})_t = \frac{(E_{TOT})_t}{(Y_{TOT})_t} \quad (3)$$

Where,

$(\Delta I_{TOT})_{0,T}$: Total change in aggregate industrial energy intensity between T and 0 years (MJ/\$).

$(\Delta I_{STR})_{0,T}$: Structural effect between T and 0 years (MJ/\$).

$(\Delta I_{EFF})_{0,T}$: Efficiency effect between T and 0 years (MJ/\$).

$(I_{TOT})_t$: Industrial aggregate energy intensity at year t .

$(E_{TOT})_t$: Total industrial energy consumption (TJ).

$(Y_{TOT})_t$: Total industrial production value added (Million \$ in 1999 constant prices) at year t .

The aggregate energy intensity can be expressed as follows:

$$(I_{TOT})_t = \sum_i (E_i)_t / (Y_{TOT})_t \quad (4)$$

Where,

$(E_i)_t$: Energy consumption in industry i at year t (GWh).

equation (4) can be rewritten as:

$$(I_{TOT})_t = \sum_i ((Y_i)_t / (Y_{TOT})_t) ((E_i)_t / (Y_i)_t) = \sum_i (y_i)_t (I_i)_t \quad (5)$$

Where,

$(Y_i)_t$: Production value added of industry i (Million \$ in 1999 constant prices) at year t .

$(y_i)_t$: Production share of industry i ($= (Y_i)_t / (Y_{TOT})_t$) at year t .

$(I_i)_t$: Energy efficiency of industry i ($= (E_i)_t / (Y_i)_t$) at year t .

where the summation is taken over all sub-sectors (industries). The aggregate energy intensity can be expressed in terms of production structure and industry energy efficiency as follows:

Equation 2 can be re-written as:

$$(\Delta I_{TOT})_{0,T} = (I_{TOT})_T - (I_{TOT})_0 = \sum_i (y_i)_T (I_i)_T - \sum_i (y_i)_0 (I_i)_0 \quad (6)$$

equation (6) can be rewritten as:

$$(\Delta I_{TOT})_{0,T} = \sum_i ((y_i)_T - (y_i)_0) (I_i)_0 + \sum_i ((I_i)_T - (I_i)_0) (y_i)_0 + \sum_i ((y_i)_T - (y_i)_0) ((I_i)_T - (I_i)_0) \quad (7)$$

where the first two terms on the right-hand side of Equation (7) are the structural effect $((\Delta I_{STR})_{0,T})$ and the efficiency effect $((\Delta I_{EFF})_{0,T})$ respectively. The third term, which is the interaction, is the residual; this residual is split equally between the structural and efficiency effects:

$$(\Delta I_{STR})_{0,T} = \sum_i ((y_i)_T - (y_i)_0)(I_i)_0 + \frac{1}{2} \sum_i ((y_i)_T - (y_i)_0)((I_i)_T - (I_i)_0) \quad (8)$$

$$(\Delta I_{EFF})_{0,T} = \sum_i ((I_i)_T - (I_i)_0)(y_i)_0 + \frac{1}{2} \sum_i ((y_i)_T - (y_i)_0)((I_i)_T - (I_i)_0) \quad (9)$$

6. Results and Discussion

Figure 5 presents how the aggregate energy intensity varies with time, and how these changes are decomposed by the Refined Laspeyres Method. It is obvious that the aggregate energy intensity has declined over the studied period, at an annual rate of approximately 5.24%. During this period, improvements in energy efficiency contributed largely to this decline, and caused, on average, approximately 3.51% yr^{-1} decline in aggregate energy intensity. This could be attributed to some improvements in energy utilization efficiency, especially in newly established industries which usually tend to employ latest machinery and technologies. Another factor that may contribute to the reported decline in aggregate energy the consecutive increase in energy unit price, which has been adjusted three times during 1998-2005, forced all sectors of the economy, including industries of all categories and sizes, to think carefully about enhancing efficiency in all activities and operations [35]. On the other hand, moving towards non-intensive energy industries, i.e. structural effect, such as electronics, tobacco and clothes, accounts for about 1.73% yr^{-1} decline in aggregate energy intensity. In 1998 there were 9,039 industrial establishments registered in Jordan. However, this figure rose to reach approximately 13,791 in 2005 [32]; the net increase occurred in small industrial firms that usually considered as non-intensive energy consuming industries.

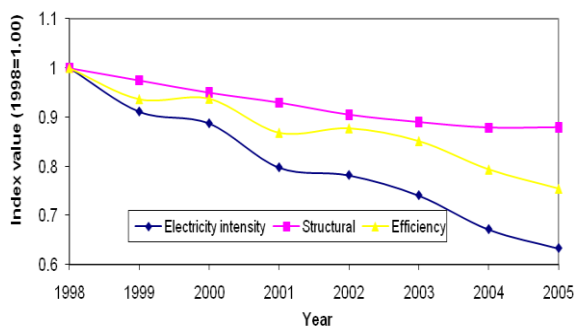


Figure 5. Time series decomposition for the Jordanian industrial energy intensity.

However, during the last decade, it can be said that energy conservation and management measures were taken

more seriously by the top management of large industries in Jordan. For example, the new strategic partner, LFARGE, with Jordan Cement Factories Company worked hard in the last few years to reduce operating costs, including fuel and electricity consumption [36]. Recently, in 2005, MEMR in close cooperation with qualified consultants in the filed of energy management conducted a field study and detailed energy audits for about 15 medium-size industries representing most industrial sub-sectors. The final report concluded that it is possible to save about 15-25% of energy and electricity consumption in these industries with relatively low investments: short pay back periods of less than 14 months [37].

7. Conclusions

In this paper, factors that have influenced changes in aggregate energy intensity of the Jordanian industrial sector were determined. Between 1998 and 2005, aggregate energy intensity of the Jordanian industrial sector decreased from 40.6 $\text{MJ}/\$$ in 1998 to 25.7 $\text{MJ}/\$$ in 2005 (constant 1999 prices). Results of the decomposition analysis prove that efficiency effect to be greater, implying innovation, technical change, diffusion and adaptability to more efficient technologies as main sources of aggregate energy intensity reduction. Contributions to aggregate energy intensity decrease are 33 and 67% for structural and efficiency effects respectively.

To ascertain the relative importance of structural change and intensity change is important not only because it provides policy makers with the energy impact of the policies that have been implemented, but also because a good understanding of this issues helps to improve the credibility of future projections for energy demand and energy-related emissions.

Forecasting of energy use in the future has to be based on information and understanding of the developments in the past; therefore, this kind of analysis may give policy makers and analysts indication of how energy demand, and required capacity, may change into future. This paper can be considered as a milestone for improving and restructuring the Jordanian industrial sector in the near future for purposes of improving its energy utilization efficiency.

References

- [1] Department of Statistics, DoS. Statistical Yearbook 2006. Amman, Jordan, 2007.
- [2] National Population Committee. National population strategy. General Secretariat of National Population Committee. Amman, Jordan, 2005.
- [3] Ang BW, Zhang FQ, Choi KH. Factorizing changes in energy and environmental indicators through decomposition. Energy 1998 ;23 (6): 489-495.
- [4] Liu FL, Ang BW. Eight methods for decomposing the aggregate energy-intensity of industry. Applied Energy 2003; 76 (1): 15-23.
- [5] Choi KH, Ang BW. Decomposition of aggregate energy intensity changes in two measures: ratio and difference. Energy Economics 2003; 25 (6): 615-624.

- [6] Myers J, Nakamura L. Saving energy in manufacturing. Ballinger: Cambridge, MA, 1978.
- [7] Ostblom G. Energy use and structural changes: factors behind the fall in Sweden's energy output ratio. *Energy Economic* 1982; 4(1): 21-28.
- [8] Jenna C, Cattell R. Structural changes and energy efficiency in industry. *Energy Economics* 1983; 5(2): 114-123.
- [9] Gardner T, Elkhafif M. Understanding industrial energy use: structural and energy intensity changes in Ontario industry. *Energy Economics* 1998; 20 (1): 29-41.
- [10] Zhang Z. Why did energy intensity fall in China's industrial sector in the 1990s? The relative importance of structural change and intensity change. *Energy Economics* 2003; 25 (6): 625-638.
- [11] Steenhof P. Decomposition of electricity demand in China's industrial sector. *Energy Economics* 2006; 28 (3): 370-384.
- [12] Gonzalez P, Suarez R. Decomposing the variation of aggregate electricity intensity in Spanish industry. *Energy* 2003; 28 (2): 171-184.
- [13] Bhattacharyya S, Ussanarassamee A. Changes in energy intensities of Thai industry between 1981 and 2000: a decomposition analysis. *Energy Policy* 2005; 33 (8): 995-1002.
- [14] Ediger V, Huvaz O. Examining the sectoral energy use in Turkish economy (1980-2000) with the help of decomposition analysis. *Energy Conversion and Management* 2006; 47 (6): 732-745.
- [15] Alghandoor A, Phelan PE, Villalobos R, Phelan BE. U.S. manufacturing aggregate energy intensity decomposition: the application of multivariate regression analysis. *International Journal of Energy Research* 2008; DOI: 10.1002/ER.1334 (to appear).
- [16] Huntington HG. The impact of sectoral shifts in industry on U.S. energy demand. *Energy* 1989; 14 (6): 363-372.
- [17] Ang BW. Decomposition methodology in industrial energy demand analysis. *Energy* 1995; 20 (11): 1081-1095.
- [18] Ang BW, Zhang FQ. Survey of index decomposition analysis in energy and environment studies. *Energy* 2000; 25 (12): 1149-1176.
- [19] Liu C. A study on decomposition on industry energy consumption. *International Research Journal of Finance and economics* 2006; November 6: 73-77.
- [20] Fisher I. The making of index numbers. Houghton Mifflin: Boston, 1972.
- [21] Boyd GA, Hanson DA, Sterner T. Decomposition of changes in energy intensity: a comparison of the Divisia Index and other methods. *Energy Economics* 1998; 10 (4): 309-312.
- [22] Lu I, Lin S, Lewis C. Decomposition and decoupling effects of carbon dioxide emission from highway transportation in Taiwan, Germany, Japan, and South Korea. *Energy Policy* 2007; 35 (7): 3226-3235.
- [23] Tamimi A. Energy situation in Jordan. *Energy Conversion and Management* 1993; 34 (6), 519-521.
- [24] Jaber JO, Mohsen MS, Probert S, Alees M. Future electricity-demands and greenhouse-gas emissions in Jordan. *Applied Energy* 2001; 69 (1): 1-18.
- [25] Jaber JO. Future energy consumption and greenhouse gas emissions in Jordanian industries. *Applied Energy* 2002; 71 (1):15-30.
- [26] Akash B, Mohsen MS. Current situation of energy consumption in the Jordanian industry. *Energy Conversion and Management* 2003; 44 (9): 1501-1510.
- [27] Al-Ghandoor A, Al-Hinti I, Jaber JO, Sawalha SA. Electricity consumption and associated GHG emissions of the Jordanian industrial sector: Empirical analysis and future projection. *Energy Policy* 2008; 36 (1): 258-267.
- [28] A. Al-Ghandoor, I. Al-Hinti, A. Mukattash, Y. Abdallat. Decomposition analysis of electricity use in the Jordanian industrial sector. *International Journal of Sustainable Energy*, V. 29, 2010, 233-244.
- [29] Al-Ghandoor A., Jaber J., Samhoury M., Al-Hinti I. 2009. Understanding aggregate electricity intensity change of the Jordanian industrial sector using decomposition technique. *International Journal of Energy Research* 33:255-266.
- [30] Ministry of Energy and Mineral Resources (MEMR). Annual Report 2006. Amman, Jordan, 2007.
- [31] National Electric Power Company (NEPCO). Annual report 1998-2005. Amman, Jordan, 1999-2006.
- [32] Department of Statistics, DoS. Statistical Yearbook 1998-2005. Amman, Jordan, 1999-2006.
- [33] Department of Statistics, DoS. Price indices. Amman, Jordan, 2007. Retrieved on Oct. 20 from http://www.dos.gov.jo/sdb_ec/sdb_ec/index.htm.
- [34] Sun J. Changes in energy consumption and energy intensity: A complete decomposition model. *Energy Economics* 1998; 20 (1): 85-100.
- [35] Jaber JO, Jaber Q, Sawalaha S, Mohsen MS. Evaluation of conventional and renewable energy sources for space heating in the household sector, *Renewable and Sustainable Energy Reviews* 2008; 12 (1): 278-289.
- [36] LFARGE, Annual Report 2005, Jordan Cement Factories Company. Amman, Jordan, 2006.
- [37] MEMR. Energy Conservation Study in Selected Industries and Commercial Enterprises in Jordan, Ministry of Energy and Mineral Resources. Amman, Jordan, 2006.

Inverse Design of Impeller Blade of Centrifugal Pump with a Singularity Method

Wen-Guang LI*

Department of Fluid Machinery, Lanzhou University of Technology, 287 Langongping Road, 730050 Lanzhou, China

Abstract

The singularity method has been extensively applied into an analysis of the potential flow through centrifugal pump impellers, i.e. direct problem, but it was little utilized in inverse design of such impeller blades, i.e. inverse problem. In this paper, a singularity method was applied for inversely designing impeller blades. A cubic Bezier curve was established to express mathematically density function of bound vortex intensity along the blade camber line so as to get a smooth and loading carefully controlled blade. The angle of attack and blade loading coefficient were taken into account in the given density function of bound vortex intensity. The direct and inverse problems have been validated with a typical experimental centrifugal pump impeller. Furthermore, the impeller blades were redesigned by using the method, and the three-dimensional turbulent viscous flows inside the original and redesigned impellers were calculated numerically by means of a CFD code Fluent. It was shown that the blade shape and flow pattern on the blade can be controlled easily by altering the density function of bound vortex intensity. The CFD outcomes confirmed that the original impeller hydraulic efficiency was improved by 5% at the design duty, but 9% at off-design condition.

© 2011 Jordan Journal of Mechanical and Industrial Engineering. All rights reserved

Keywords: centrifugal pump; singularity method; impeller; blade; inverse problem; inverse design; CFD

1. Introduction*

The singularity method is an important numerical approach for numerically solving blade-to-blade potential flows within centrifugal impellers and has been substantially involved in the analysis of hydrodynamics of centrifugal pump impellers for years, for instance, Ayyubi and Rao [1], Reddy and Kar [2], Ogawa and Murata [3, 4], [5], Kumar and Rao [5, 6]. Unfortunately, this method was almost applied to solve a direct problem, rather than an inverse one for centrifugal impellers. Betz and Flugge-Lotz [7] initially proposed a singularity approach for inversely establishing radial impeller blades. They realized that a two-dimensional potential internal flow in a centrifugal impeller is a superposition of a uniform inflow at the impeller entrance and a non-uniform flow caused from a series of vortices bound to the blade camber lines. The density of bound vortex intensity was assumed to be varied circumferentially by means of the Fourier series. An analytical equation for calculating the absolute velocity induced by those vortices at a point in the flow domain was derived. Kashiwabaray [8] expanded this method analytically to make it suitable to mixed-flow impellers. In his proposal, the blade shape was determined iteratively by using the prescribed fluid relative velocity profile on both sides of blade. A series of vortex and source (sink) were allocated simultaneously on the blade camber lines. The

density of bound vortex intensity was determined numerically with the difference of the two prescribed velocity profiles and the length of camber line. The intensity of the source (sink) was given by using the blade thickness profile specified. Finally, a blade angle was calculated by means of the tangential condition, causing an updated blade shape. This process was redone unless the blade shape no longer was changed. This method was applicable to the centrifugal impellers with more number of blades (>7). Murata and Miyake et al [9] mapped a S1 stream-surface (blade-to-blade) of revolution onto a two-dimensional rectilinear cascade by using conformational mapping function twice. Similarly, a series of vortex and source (sink) were distributed on the blade camber line; then the densities of the bound vortex and source (sink) intensities were determined by using the relative velocity and blade thickness prescribed. The induced velocity equations in Murata and Miyake et al [9] were more general than those in Betz and Flugge-Lotz [7]. It is believed the blade shape control is hard in those two proposals since the relative velocity profile on both sides of blade must be prescribed together. They seem inconvenient for applications.

It is interesting to notice that a simple and smart singularity approach for solving the blade-to-blade

* Corresponding author. Liwg38@yahoo.com

potential flow on a revolutionary stream-surface was presented by Senoo and Nakase [10]. The method has found significant applications in the analysis of flow inside centrifugal impellers. Recently, it was upgraded with three kinds of density function of bound vortex intensity by Li [11] and was applied to analyze the potential flow in very low specific speed centrifugal pump impellers with various blades and splitters.

Based on this method, a singularity method for designing centrifugal pump impeller blades as an inverse problem has been developed in this paper. The objective is to clarify feasibility of the method for establishing blades and to identify if it can easily control the blade shape. The blade of an experimental centrifugal pump impeller was redesigned as an inverse problem. The hydraulic performance of the original and redesigned impellers was estimated numerically by using CFD code Fluent. As a consequence, more than 5% improvement in the hydraulic efficiency was confirmed.

2. Equations and Methods

2.1. Direct Problem

For convenience, a centrifugal pump impeller is assumed to rotate contraclockwise as it is viewed against its inlet (Fig. 1). The intensity of a contraclockwise bound vortex is assumed to be positive; otherwise, it is negative. Further, the blades of the impeller are curved backward. In that case, the blade angle β_b is positive, which is defined as the angle between a tangent to the blade camber line at a point on a S1 stream-surface of revolution and the reverse direction of impeller rotation at that point. Note that the angle $\beta_b - 90^\circ$ is negative, which is the angle between that tangent and the meridian plane through that point.

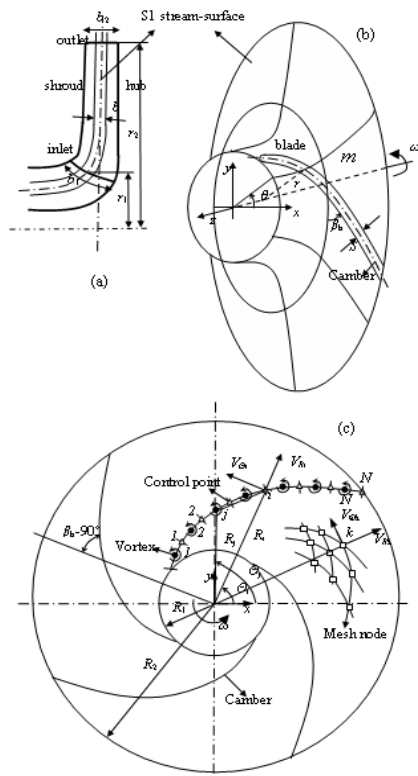


Figure 1. Impeller meridian plane (a) and S1 stream surface (physical surface) (b) as well as computational plane (c), where bound vortices are specified

For a direct problem, the number of blades, blade camber shape, blade thickness, S1 stream-surfaces of revolution and their thickness, the volumetric flow rate through the impeller and rotational speed etc have been known. The following steps are needed to analyze a two-dimensional ideal fluid flow in a centrifugal pump impeller by using the singularity method proposed initially by Senoo and Nakase [10] and updated by Li [11].

1. A S1 stream-surface of revolution in terms of the coordinates $m-\theta$ in the physical surface was mapped onto a circular cascade in terms of the polar coordinates $R-\Theta$ in the computational plane by using the Prasil transformation relations in Senoo and Nakase [10]

$$\begin{cases} R = R_1 e^{\int_0^m \frac{dm}{r}} \\ \Theta = \theta \end{cases} \quad (1)$$

The circular cascade has an inner R_1 and an outer radius R_2 , in which $R_2 = R_1 \exp\left(\int_0^{m_2} 1/r dm\right)$, m_2 is the length of the meridian streamline at the blade exit, r is the radius specifying the stream-surface. Every computation of the flow is carried out in the computational plane; once finished, it will be transformed back to the physical surface via Eq. (1).

2. A series of bound vortices are assumed to be distributed on a blade camber line, so the absolute velocity components induced by these vortices ($j=1,2,\dots,N$) at an observed point i on the blade camber line or a point k in the flow domain in the computational plane are given as follows

$$\begin{cases} V_{\Theta i} = + \frac{Z}{4\pi R_i} \int_0^{s_2} (1 - F_{\Theta}) \lambda ds \\ V_{Ri} = - \frac{Z}{2\pi R_i} \int_0^{s_2} F_R \lambda ds \end{cases} \quad (2)$$

And

$$\begin{cases} F_{\Theta} = \frac{(R_j/R_i)^Z - (R_i/R_j)^Z}{(R_j/R_i)^Z + (R_i/R_j)^Z - 2 \cos[Z(\Theta_i - \Theta_j)]} \\ F_R = \frac{\sin[Z(\Theta_i - \Theta_j)]}{(R_j/R_i)^Z + (R_i/R_j)^Z - 2 \cos[Z(\Theta_i - \Theta_j)]} \end{cases} \quad (3)$$

where s_2 is the length of blade camber line at the blade outlet, Z is the number of blades, λ is the density of bound vortex intensity, which is expressed in terms of the length of blade camber s . The velocity components ($V_{\Theta k}, V_{Rk}$) are for the point k in the flow domain.

3. Provided that the observed point i is on a blade camber line, the fluid relative velocity will be the tangent at this point, i.e. the relative flow angle β_i equals the blade angle β_{bi} . Eventually, a tangential condition is satisfied

$$\tan(\beta_i - 90^\circ) = \frac{W_{\Theta i}}{W_{Ri}} = \tan(\beta_{bi} - 90^\circ) \quad (4)$$

The relative velocity components are related to the absolute velocity via the following equations

$$\begin{cases} W_{Ri} = V_{Ri} + \bar{W}_{Ri} \\ W_{\Theta i} = V_{\Theta i} - \bar{U}_i \end{cases} \quad (5)$$

The velocity components \bar{W}_{Ri} and \bar{U}_i are estimated by using the flow rate through the impeller and the pre-circulation in the impeller entrance as follows

$$\begin{cases} \bar{W}_{Ri} = \frac{Q}{b_i(2\pi R_i - ZS_{ui})} \\ \bar{U}_i = \frac{1}{R_i}(v_{u1}r_1 - u_i r_i) \end{cases} \quad (6)$$

where Q is the flow rate across the impeller, b_i is the thickness of S1 stream-surface, the blade circumferential thickness is $S_{ui} = S_i / \sin \beta_{bi}$, S_i is the blade thickness on S1 stream-surface, $v_{u1}r_1$ is the absolute velocity moment at the impeller entrance, u_i is the impeller speed at the radius r_i , $u_i = r_i \omega$, ω is the angular rotational speed of impeller.

Putting Eq. (2) into (4), the tangential condition is rewritten as

$$\int_0^{s_2} (1 - F_{\Theta}) \lambda ds + 2 \tan(\beta_{bi} - 90^\circ) \int_0^{s_2} F_R \lambda ds = \frac{4\pi R_i}{Z} (\bar{U}_i + \tan(\beta_{bi} - 90^\circ) \bar{W}_{Ri}) \quad (7)$$

This is a system of integral equations in terms of the unknown density of bound vortex intensity λ . In order to get a numerical solution of such an equation system, the continuous density λ needs to be discretized. Here, a continuous blade camber line is divided into small-sized segment elements with a number of N . The density of bound vortex intensity is considered to be constant in each element, but the density in one element may be different from that in another. It is assumed the bound vortex is located at the centre of each element. The intensity of a bound vortex j ($j=1,2,3,\dots,N$) is connected with its density via

$$\mu_j = \lambda_j \Delta s_j \approx \lambda_j \Delta s_j \quad (8)$$

where Δs_j denotes the length of an element in which the vortex j is prescribed. Substituting λds in Eq. (7) with $\lambda_j \Delta s_j$ in Eq. (8), the system of integral equations becomes a system of linear algebraic equations in terms of λ_j

$$\left[\sum_{j=1}^N (1 - F_{\Theta j}) + 2 \tan(\beta_{bi} - 90^\circ) F_{Rj} \right] \Delta s_j \lambda_j = \frac{4\pi R_i}{Z} (\bar{U}_i + \tan(\beta_{bi} - 90^\circ) \bar{W}_{Ri}) \quad (9)$$

where the point i is on the blade camber line, but it is the node with larger radius in an element. The tangential condition has been applied at that point, so the point i ($i=1,2,3,\dots,N$) is considered to be a control point. Note that the total number of control point i equals the number of elements N . In the last element near the blade trailing edge, the Kutta condition must be fulfilled, i.e. $\lambda_N = 0$. In that case, the Eq. (9) represents a set of $N-1$ simultaneous linear algebraic equations in $N-1$ unknown variables.

4. Solve the system of linear equations (9) to determine the unknown λ_j .

5. The induced absolute velocity components in Eq. (2) at the point i on the blade camber line can be calculated by using the λ that has been determined. Subsequently, Eq. (5) is applied to figure out the

relative velocity components W_{Ri} , $W_{\Theta i}$ on the blade pressure and suction sides as follows

$$\begin{cases} W_{si} = \sqrt{W_{Ri}^2 + W_{\Theta i}^2} + \frac{1}{2} \lambda_i \\ W_{pi} = \sqrt{W_{Ri}^2 + W_{\Theta i}^2} - \frac{1}{2} \lambda_i \end{cases} \quad (10)$$

6. Calculate the fluid relative velocity at specified points or a series of node of a mesh in the flow passage, if necessary. Otherwise, go to the next step.

7. The relative velocity components in the physical surface or S1 stream-surface in terms of the coordinates $m-\theta$ are obtained with the following transformation

$$\begin{cases} w_{ri} = (R_i / r_i) W_{Ri} \\ w_{\theta i} = (R_i / r_i) W_{\Theta i} \end{cases} \quad (11)$$

Finally, the Bernoulli equation can be utilized to get the pressure field in the flow passage to a reference pressure. Moreover, the theoretical head of impeller is predicted by

$$H_{th} = (v_{u2} u_2 - v_{u1} u_1) / g \quad (12)$$

And the mean circumferential component of absolute velocity at the blade outlet is written as

$$\bar{v}_{u2} = u_2 - \frac{Z}{2\pi w_{m2}} \int_0^{2\pi} w_{u2} w_{m2} d\theta \quad (13)$$

where the mean meridian component of relative velocity at the blade outlet is

$$\bar{w}_{m2} = \frac{Z}{2\pi} \int_0^{2\pi} w_{m2} d\theta \quad (14)$$

The slip factor is expressed as

$$\sigma = \frac{Z}{2\pi u_2 w_{m2}} \int_0^{2\pi} w_{u2} w_{m2} d\theta - \frac{Q}{u_2 b_2 (2\pi r_2 - Z S_{u2}) \tan \beta_{b2}} \quad (15)$$

2.2. Inverse Problem

For an inverse problem in the singularity method, the number of blades, blade thickness profile, blade leading and trailing edge shapes and positions, S1 stream-surface shape and thickness, flow rate through an impeller and rotating speed of the impeller have been known in advance; just the blade camber line needs to be determined.

Usually, the blade camber line is represented by a relation of radius to warping angle or vice versa. How to establish such a relation is a key issue in the inverse problem. In most cases, a correct relation has to be achieved iteratively based on an initially guessed one. In this paper, the following steps are conducted to get a proper blade camber line.

1. Specify a temporary distribution of blade angle β_b^0 along a meridian streamline from the blade leading edge to trailing edge, subsequently, a relation of initial wrapping angle of blade with r can be established by integrating the blade pattern equation as follows

$$\theta = \int_0^{m_2} \frac{\tan(\beta_b - 90^\circ)}{r} dm \quad (16)$$

For the sake of convenience, the initial blade usually is radial, i.e. $\beta_b = 90^\circ$. Eq. (16) is numerically integrated by simply applying the trapezoid rule. Once the initial

relation $\theta - r$ is available, the initial blade will be mapped onto the computational plane with Eq. (1).

2. Prescribe a profile of density of bound vortex intensity on the blade camber line. A cubic Bezier curve in Rogers [12] is utilized to describe the density of bound vortex intensity to guarantee a sufficient smooth blade camber line achievable. Such a curve is defined by a control polygon with four control vertices A, B, C and D as shown in Fig. 2. Then the density of bound vortex intensity is expressed mathematically as

$$\lambda(s) = (1-t)^3 \lambda_a + 3t(1-t)^2 \lambda_b + 3t^2(1-t) \lambda_c + t^3 \lambda_d \quad (17)$$

where the parameter $t = (s - s_a) / (s_d - s_a)$, $\lambda_b = c \lambda_a$, $\lambda_c = d \lambda_a$, factors c and d are adjustable to correlate λ_a .

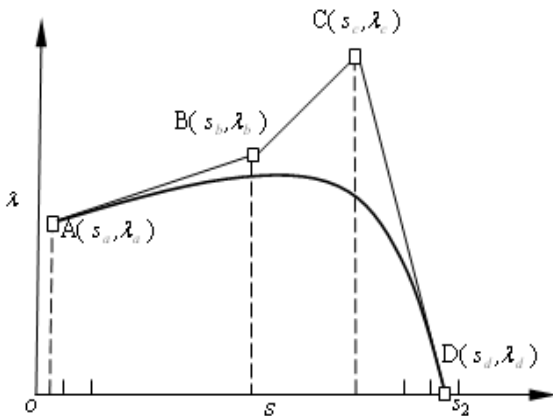


Figure 2. A cubic Bezier curve is used to define density distribution of bound vortex on blade

Firstly, the initial blade camber is divided into N elements equally, and the length of each element is Δs . At point D, the Kutta condition must be yielded, so the coordinates of D are $s_s = s_2 - \Delta s / 2$, $\lambda_d = 0$. At point A, $s_a = 0.5 \Delta s$, the intensity λ_a is determined such a way that a proper angle of attack α must be realized. In doing so, a relative flow angle β_1 to the blade leading edge is estimated as follows

$$\beta_1 = \tan^{-1} \left(\frac{v_{m1}}{u_1 - v_{u1}} \right) \quad (18)$$

and the meridian velocity component at the leading edge is given by

$$v_{m1} = \frac{Q}{(2\pi r_1 - Z S_{u1}) b_1} \quad (19)$$

Secondly, a proper angle of attack is specified. If the impeller is expected to have a better cavitation performance, then $\alpha = 0.5^\circ - 3^\circ$; otherwise, $\alpha = 3^\circ - 5^\circ$. In consequence, the blade angle at the inlet is $\beta_{b1} = \beta_1 + \alpha$. Because of $r_1 \approx r_a$ (radius at point A), then $\beta_{b1} \approx \beta_{ba}$, $u_1 \approx u_a$ and $v_{m1} \approx v_{ma}$. Subsequently, the circumferential component of absolute velocity at point A is written as

$$v_{ua} = u_1 - \frac{v_{m1}}{\tan \beta_{b1}} \quad (20)$$

Finally, the density of bound vortex intensity at point A is given by

$$\lambda_a = \frac{2\pi r_a (v_{ua} - v_{u1})}{Z \Delta s} \quad (21)$$

Points B and C are used to control the peak value of the density and its position on the blade camber line. Usually,

$s_b \in [0.3(s_d - s_a) + s_a, 0.5(s_d - s_a) + s_a]$ and $s_c \in [0.8(s_d - s_a) + s_a, 0.95(s_d - s_a) + s_a]$. The densities λ_b , λ_c are specified with two factors b and c as well as λ_a , but they are subject to two critical conditions: (a) the peak loading coefficient (velocity gradient) on the blade is less than 2, i.e. $\Delta W / W \leq 2$ to avoid a reverse flow on the blade pressure side in Balje [13], where $\Delta W = W_s - W_p$, W_s

is the relative velocity on blade suction side, W_p that on blade pressure side, $W = 0.5(W_s + W_p)$; (b) make sure the theoretical head developed by the designed impeller must be over the head desired.

3. Calculate the relative velocity components $W_{\theta i}$, W_{Ri} by using Eqs. (2), (3), (5), (6) with the specified density profile of bound vortex intensity, the blade angle β_{bi} is updated with Eq. (4).

4. Integrate Eq. (16) once more by applying the updated blade angle β_{bi} . In consequence, the relation between blade warping angle and blade angle is upgraded and a new blade camber line is generated. This computational process isn't stopped until the blade camber line shows little change in its shape. The blade camber line convergence criterion is the relative error (difference of warping angle over the mean value between two successive iterations) is less than 1×10^{-3} .

5. Calculate the relative velocities in the flow passage with Eqs. (2,3, 5 and (6) and transform those velocities into the physical surfaces with Eq. (11). Finally, the impeller theoretical head and slip factor etc are estimated by using Eqs. (12-15).

6. If these primary hydraulic parameters are satisfactory, then this inverse design process will be terminated. Otherwise, a new design should be launched with a modified density profile of bound vortex intensity or other design variables. Nevertheless, the steps (1)-(5) will be carried out until a satisfactory result is achieved.

7. Generate the three-dimensional solid geometry model of the impeller just established and launch CFD stimulations of viscous fluid flow inside the impeller to make sure the impeller has shown a perfect performance and pretty well flow patterns. Otherwise, necessary corrections should be applied to the design variables and a new inverse design is started by following the steps (1) to (5).

3. Results and Discussions

3.1. Direction Problem Validation

In order to validate the method proposed, the ideal fluid flow in the experimental impeller presented in Kamimoto and Hirai [14] was analyzed by using the method. The duty of the impeller at design condition is as follows: $Q = 287 \text{ m}^3/\text{h}$, head $H = 26 \text{ m}$, rotating speed $n = 1750 \text{ r/min}$, specific speed $n_s = 156$ ($n_s = 3.65 n \sqrt{Q} / H^{0.75}$, r/min, m^3/s , m), impeller tip speed $u_2 = 27.5 \text{ m/s}$, flow coefficient $\phi = Q / 2\pi r_2 b_2 u_2 = 0.154$ and head coefficient $\psi = gH / u_2^2 = 0.34$. The geometrical parameters of the impeller as the following: impeller outlet diameter $D_2 = 300 \text{ mm}$, impeller eye diameter $D_e = 150 \text{ mm}$. Four constant-width ($b = 20 \text{ mm}$), constant-thickness ($S = 3 \text{ mm}$), constant-angle ($\beta_b = 30^\circ$) logarithmic spiral blades were installed in the shrouded radial impellers. In spite of a bit high specific speed, the blades were two-dimensional and

without twist along blade span for convenience in experiments in Kamimoto and Hirai [14]. Since this experimental impeller serves a benchmark in the paper, it is not intended to design a new impeller with twist blades. This means the ideal flow analysis and blade redesign were conducted just on one S1 stream-surface of revolution.

The effect of number of elements of discretized bound vortices N on the impeller theoretical head coefficient ψ is shown in Fig. 3. The number of elements does affect the head coefficient moderately; fortunately, this effect is negligible as the number more than 60. In that case, the length of element is around 2.5mm. In the following computations, the number of element is kept to be 60.

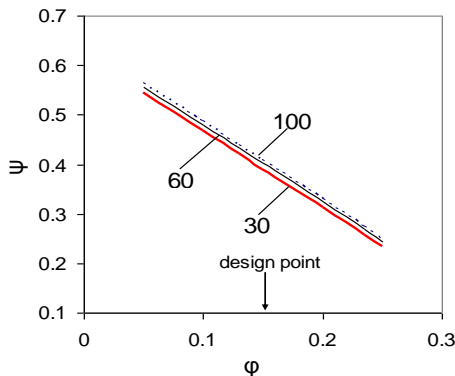


Figure 3. Impeller theoretical head against flow coefficient at various numbers of vortex elements.

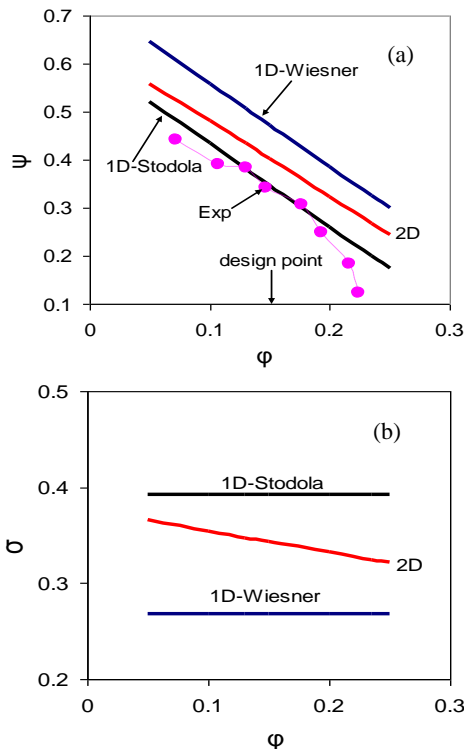


Figure 4. Impeller theoretical head coefficient and slip factor in terms of flow coefficient, the symbols represent experimental data in Kamimoto and Hirai [14].

The impeller theoretical head ψ , which was determined by using the 2D singularity method, is plotted in terms of flow rate coefficient ϕ in Fig. 4a. The head

coefficients evaluated by means of the one-dimensional (1D) Euler turbomachinery head equation with respective corrections of Stodola and Wiesner slip factors are also shown in the figure. The experimental head coefficient in Kamimoto and Hirai [14] is involved in the plot as well. A comparison of 2D computed slip factor to those of Stodola and Wiesner is made in Fig. 4b. The head coefficient given by 2D singularity approach is in between those of the 1D Euler head plus slip factor correction. The slip factor due to the 2D singularity method is in between those of Stodola and Wiesner too. These facts suggest the results provided by 2D singularity method seems reasonable.

Figure 5 illustrates the fluid relative velocities on the blade pressure and suction surfaces as well as blade loading coefficient $\Delta W/W$ in terms of dimensionless blade camber line length. On the suction surface, the relative velocity of the 2D singularity method is fairly close to the experimental profile. On the pressure surface, however, the velocity is much lower than the experimental observation; further, at the nearby $r/r_2 = 0.55$ location, i.e. just behind the blade leading edge, the relative velocity has become zero, causing a maximum difference of velocity between the suction and pressure surfaces. Accordingly, the blade loading coefficient in Fig. 5b has also got a maximum value there. Note that this peak value has been as large as 2. It was indicated that once $\Delta W/W = 2$, a fluid flow would be separated from the blade pressure side by Balje [13]. Obviously, the computed peak loading factor is in very good agreement with such an observation. This suggests the experimental impeller has been subject to an extreme high hydrodynamic loading.

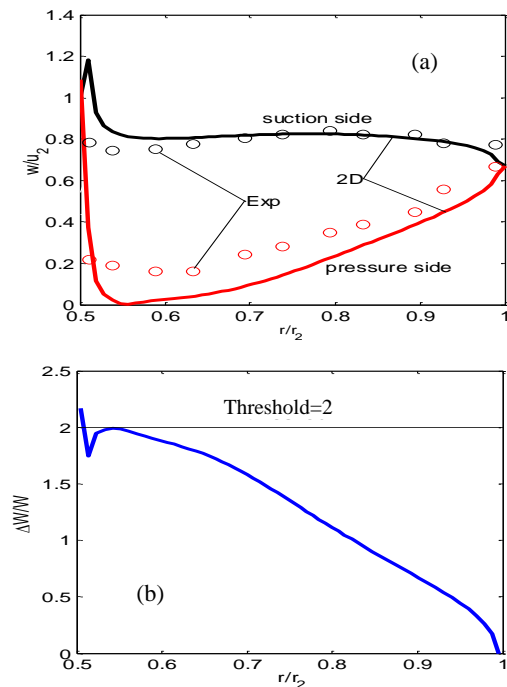


Figure 5. Relative velocity profile and blade loading coefficient on blade pressure and suction surfaces against dimensionless length of blade, the symbols indicate the experimental measurements.

For the 2D singularity method is based on an ideal fluid flow model, there is not a boundary layer in the impeller passages, causing no any hydraulic losses there. This effect causes the estimated impeller theoretical head coefficient

to be higher than the observation (see Fig. 4a). Such a flow model exaggerates the relative velocity difference between the blade suction and pressure sides, i.e. blade loading or hydrodynamic loading. A much under-estimated velocity on the blade pressure surface is responsible for the exaggerated difference. The ignored viscous and three-dimensional effect may be responsible for the disagreement in the impeller head coefficient and relative velocity profile between observation and calculation.

3.2. Inverse Problem Validation

As a known function, the density profile of bound vortex intensity on the blade camber line in Fig. 6a, which has been determined numerically in the direction problem at $\phi = 0.154$, was imbedded into a code which executes the inverse design of blade to identify if the inverse singularity method proposed is feasible or not. As result of this, a converged blade camber line of 70 iterations is shown in Fig. 6b. For that case, the relative error of warping angle actually is 9.94×10^{-4} , slightly less than the tolerance 1×10^{-3} . The original blade camber line precise restoration confirms the inverse singularity method and corresponding numerical scheme are correct and feasible.

3.3. Impeller Redesign

According to Fig. 5, at the design duty, a poor relative velocity profile is demonstrated on the blade pressure side in the original impeller. The drawbacks in the profile are that the peak loading is not only too close to the blade leading edge but also quit near the threshold. In that case, the hydraulic performance and suction characteristics of original impeller may be unsatisfactory, especially at partial flow rate. It is highly on demand to improve the impeller design. Two measures are taken hereby: (1) put more blades into impeller passages to lower the loading coefficient level, (2) move the peak loading coefficient away from the leading edge to somewhere close to the blade trailing edge. In doing so, the number of blades is increased to 5 from 4, and the density profile of bound vortex intensity is updated as shown in Fig. 7, where the peak loading factor has been moved to a position beyond the middle of blade camber line, i.e. $r/r_2 = 0.78$. The peak value of the density has been lowered as low as 17m/s.

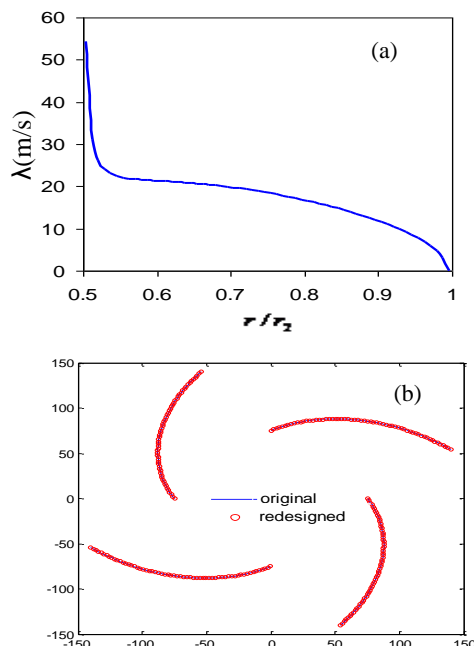


Figure 6. Known density profile of bound vortex intensity (a) and comparison of blade camber line between original and inversely designed impellers (b).

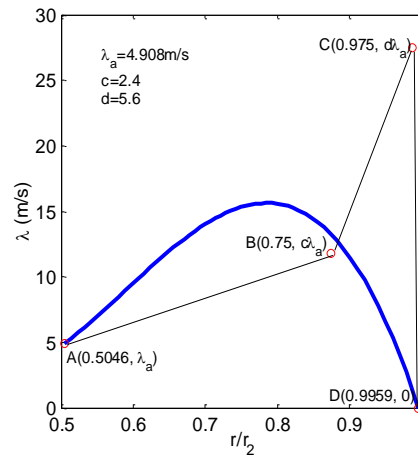
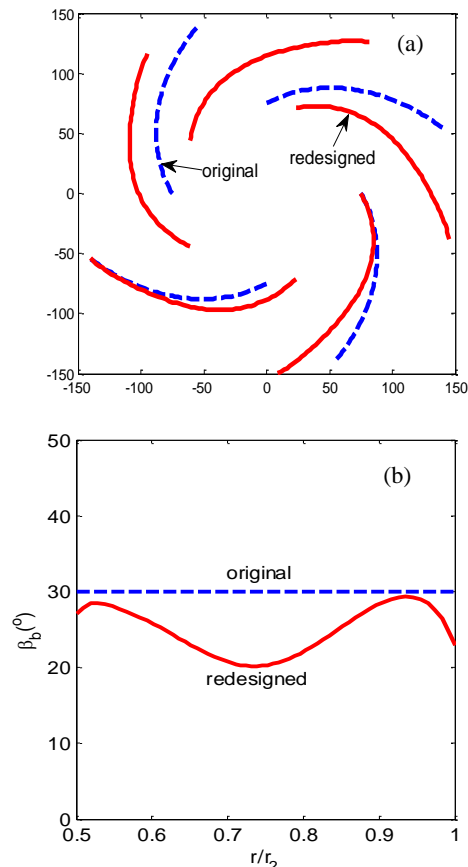


Figure 7. Modified density function of bound vortex intensity that is applied into inverse redesign of blade.



(b) of the blade angle β_b is made as 86.6° blade angle of the redesigned impeller is no longer constant, but takes the shape of 'M'. The inlet and outlet blade angles are decreased to 27° and 22.9° from 30° , respectively. Accordingly, the angle of attack is reduced to just 2° from the initial 7° .

The estimated impeller performance is compared with that of the original one in Fig. 9a. At the design duty, the

theoretical head of original impeller is improved by 1m (water column height). The redesigned impeller is featured with a sharp negative slope head curve.

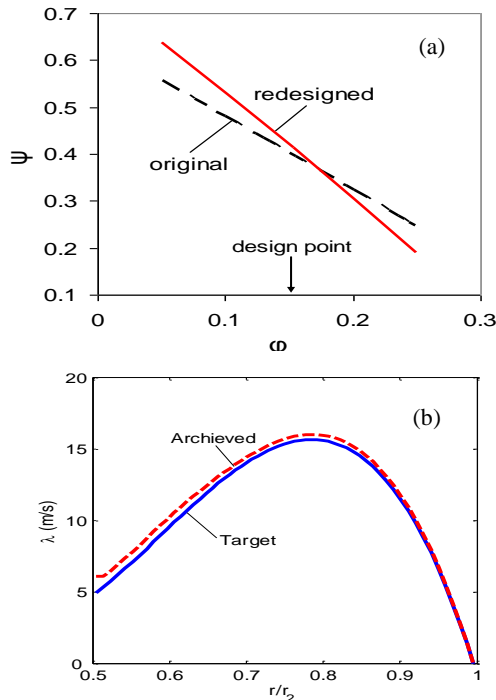


Figure 9. Impeller head coefficient (a) in terms of flow coefficient, target and achieved densities of bound vortex intensity (b).

prescribed and achieved densities of bound vortex intensity are illustrated in Fig.9b. The achieved density was evaluated based on the redesigned impeller as the direct problem. The difference in the density between two impellers does exist. It is increased towards the blade leading edge due to relatively severe bending of blade there. The maximum error is about 20% at the blade leading edge for there is a singularity point. The error is decreased to as low as 2.3% in the middle of blade length.

The blade loading coefficient is shown in Fig. 10a. Compared to Fig. 5b, the peak loading has been moved to the middle of blade length, $r/r_2 = 0.75$, and the peak value is just 1.15, which is obviously less than a threshold of 2. Likewise, the relative velocity profiles on the blade surfaces are very satisfactory (Fig. 10b). The lowest velocity position has been moved to the middle of blade; moreover, its value is much larger than zero. For the redesigned impeller, its hydraulic performance, therefore, is superior to the original impeller, especially at partial flow rate (Fig. 9a). Note that the fluid is accelerated in the 65% blade camber line length long ($0.5 \leq r/r_2 \leq 0.82$) from the leading edge to a point beyond the middle of camber line on the suction side of the redesigned impeller. Such acceleration may suppress the growth of boundary layer on the blade suction surface, and may make positive contribution to reduction of hydraulic losses.

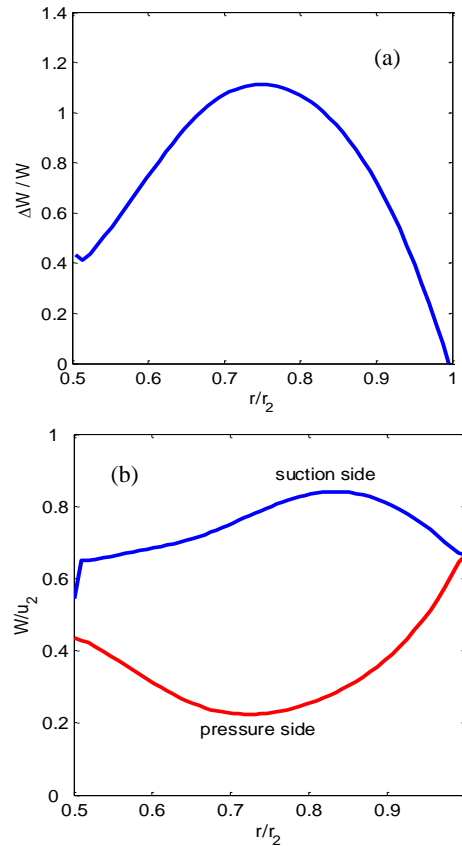


Figure 10. Loading coefficient (a) and relative velocity on blade surface (b).

3.4. CFD Conformation

3D solid geometry models of both the original and redesigned impellers have been generated by using Gambit. The 1/4 (original) and 1/5 (redesigned) of the impellers are taken as the flow domain (Fig. 11), respectively. About 0.7 million tetrahedral cells are meshed and input into a CFD code Fluent to do flow simulations. In the simulations, the fluid is assumed to be steady, incompressible and turbulent. The standard $k-\epsilon$ turbulence is activated to handle the turbulence effects. The non-equilibrium wall function is chosen to estimate wall shear stress and pressure more precisely. The detailed governing equations of flow, turbulence model and wall function can be found in Anonymous [15]. SIMPLE algorithm with the second-order up-wind scheme was applied to solve the governing equations. At the inlet to suction pipe, a normal velocity boundary is applied, which depends on flow rate. On the blade, shroud and hub, the velocity no-slip condition is held. At the outlet to impeller, zero pressure is given. The rest boundaries are subject to the periodic condition. The residual tolerance is 1×10^{-4} . The fluid is water at 20°C.

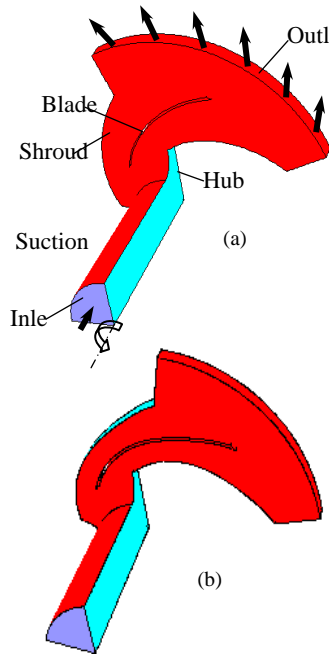


Figure 11. Flow domains of the original (a) and redesigned (b) impellers used in 3D flow CFD simulations.

The impeller theoretical head and hydraulic efficiency were extracted and are represented in Fig. 12 for the turbulent flow of viscous fluid. Obviously, the performance of the original impeller has been improved in great deal when the flow coefficient is in 0.025-0.16. At design duty $\phi = 0.154$, the hydraulic efficiency is raised by 5%, while the low flow coefficient $\phi = 0.1$, the efficiency is increased as high as 9%. These improvements suggest the blade loading control is necessary and takes a positive effect.

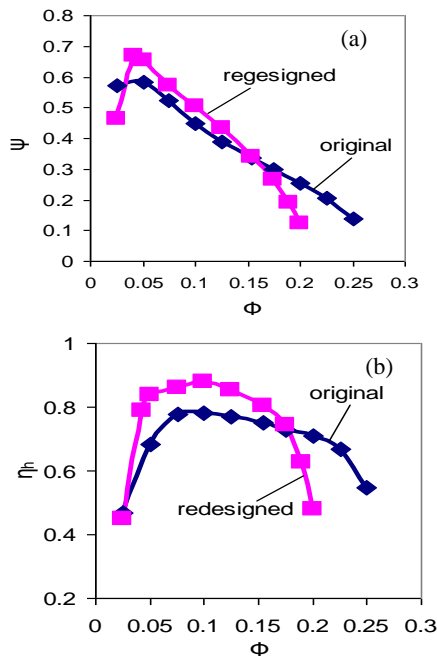


Figure 12. Head theoretical coefficient and hydraulic efficiency of the original (a) and redesigned (b) impellers calculated by CFD viscous fluid model

The relative velocity vector and pressure contour are displayed in Fig. 13 on the middle-span plane of the impellers for the viscous fluid flow. The reference pressure is 10m water column height. Even no significant evidence shows a reverse flow onset on the blade pressure side, it is noticed that a big zone with low velocity exists there in the original impeller. The blade pressure side of the impeller, especially, near the leading edge, is subject to much larger pressure compared to the redesigned impeller. Furthermore, the minimum pressure on the blade suction side in the original impeller is as low as -16.4m. In the redesigned impeller; however, it is just -5.46m.

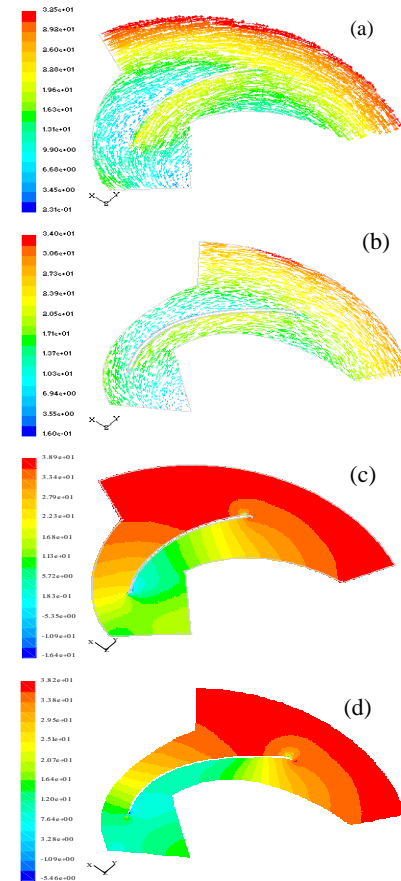


Figure 13. Relative velocity vector and static pressure contour of the original (a) & (c), redesigned (b) & (d) impellers calculated by CFD viscous fluid model.

The pressure on the blade pressure and suction sides and loading coefficient across the blade were extracted from the CFD results and are shown in Fig. 14 at the design condition. The pressure difference and loading coefficient across the blade in the original impeller is higher compared to the redesigned impeller, particularly, near the blade leading edge. Immediately after the leading edge the blade loading is kept to be nearly constant along blade in the original impeller; while it is increased until the beyond the middle of blade length, then decreased toward the trailing edge in the redesigned impeller. This suggests that the blade loading control in the inverse design is effective.

The loading coefficient magnitude and profile of 3D viscous flow are considerable different from those of 2D

potential flow shown in Fig. 5b. The reason for that is no viscous effect is involved in the potential flow model.

It is believed that the inverse singularity method can ensure an impeller to be able to achieve a better performance by using a carefully controlled density of bound vortex intensity on blade camber line. Such a method has a special significance in the redesign of existing centrifugal pump impellers.

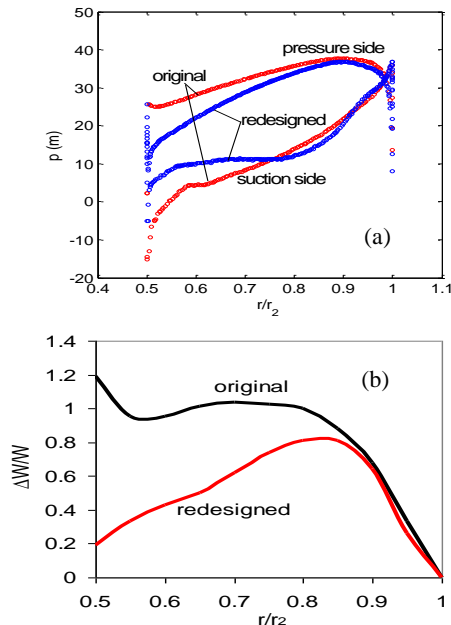


Figure 14. Pressure (a) and loading coefficient (b) on blade surface of the original and redesigned impellers in mid-span calculated by CFD viscous fluid model.

3.5. Discussion

The inverse singularity method proposed is subject to several limitations, for example, 2D, potential flow model; failure of handling viscous effect and secondary flow etc. Fortunately, these limitations can be removed by means of advanced CFD codes. For 2D blades, the blades can be established just on one S1 stream surface. For 3D twist blades, however, the blades should be designed on three or more S1 stream-surfaces. Theoretically, the current method is applicable for that case. However, how to specify density profile of bound vortex intensity along blade span needs to be investigated further. These S1 stream-surfaces of revolution can be determined by using the through-flow theory as indicated in Ghaly [16], Zangeneh [17], Borges [18], Peng et al [19]-[21].

Turbomachinery impeller blades can be established by using a given mean absolute velocity moment $V_u r$ in Borges [18], Peng et al [19]-[21], Tan et al [22], Luu et al [23], Jenkins and Moore [24], Dang and Isgro [25] and [26] or $\partial V_u r / \partial s$ in Ghaly [16] and Zangeneh [17], has long been recognized and realized. On a blade camber line, the density of bound vortex intensity λ is related to the velocity moment $V_u r$ with the following expression

$$\lambda = W_s - W_p = \frac{2\pi}{Z} \frac{\partial V_u r}{\partial s} \quad (22)$$

Since the prescribed $V_u r$ can be converted into λ , λ seems be equivalent to $\partial V_u r / \partial s$. In this contribution, λ 's effect on the fluid flow in the impeller was taken into

account by using analytical induced velocity equations. The considerable complicated mathematical contents have been removed. It is very hopeful such a simple method is acceptable for engineers.

4. Conclusions

An inverse singularity method was proposed for establishing the impeller blades of centrifugal pump in this article. A density distribution of bound vortex intensity on blade camber line was defined by using a cubic Bezier curve. The angle of attack has been involved in such a distribution. The results of the direct and inverse problems were validated by means of an experimental centrifugal pump impeller. The defined density of bound vortex intensity can ensure the designed blade to have a carefully controlled loading coefficient and smooth camber line to guarantee an improved hydraulic performance. The method may be applicable to the redesign of existing centrifugal pump impellers. Although a satisfactory outcome has been achieved yet for 2D blades, a further application to 3D twisted blades is highly desired. The prospective studies include 3D quasi-three-dimensional blade design and optimization of density profile of bound vortex intensity along blade camber line and span.

References

- [1] K. Ayyubi, Y. V. N. Rao, "Theoretical analysis of flow through two-dimensional centrifugal pump impeller by method of singularities". ASME Journal of Basic Engineering, Vol. 93, 1971, 35-41.
- [2] Y. R. Reddy, S. Kar, "Study of flow phenomena in the impeller passage by using a singularity method", ASME Journal of Basic Engineering, Vol. 94, 1972, 513-521.
- [3] T. Ogawa, S. Murata, "On the flow in the centrifugal impeller with arbitrary aerofoil blades (1st report, impeller with constant width)". Bulletin of the JSME, Vol. 17, No.108, 1974, 713-722.
- [4] T. Ogawa, S. Murata, "On the flow in the centrifugal impeller with arbitrary aerofoil blades (2nd report, the effect of change in impeller width)", Bulletin of the JSME, Vol. 17, No. 108, 1974, 723-730.
- [5] T. C. M. Kumar, Y. V. N. Rao, "Theoretical investigation of pressure distribution along the surfaces of a thin arbitrary geometry of a two-dimensional centrifugal pump impeller". ASME Journal of Fluids Engineering, Vol. 99, 1977, 531-542.
- [6] T. C. M. Kumar, Y. V. N. Rao, "Quasi two-dimensional analysis of flow through a centrifugal pump impeller". ASME Journal of Fluids Engineering, Vol. 99, 1977, 687-692.
- [7] Betz, I. Flugge-Lotz, "Design of centrifugal impeller blades". NACA TM-902, 1939, 1-27.
- [8] Y. Kashiwabaray, "Theory on blades of axial, mixed and radial turbomachines by inverse method". Bulletin of JSME, Vol. 16, No. 92, 1973, 272-281.
- [9] S. Murata, Y. Miyake, K. Bandoh, "A solution to inverse problem of quasi-three-dimensional flow in centrifugal impeller". Bulletin of JSME, Vol. 26, No. 211, 1983, 35-42.
- [10] Y. Senoo, Y. Nakase, "A blade theory of an impeller with an arbitrary surface of revolution", ASME Journal of Engineering for Power, Vol. 93, No. 4, 1971, 454-460.

- [11] W. G. Li, "Analysis of flow in extreme low specific speed centrifugal pump impellers with multi-split-blade". *International Journal of Turbo & Jet Engines*, Vol. 23, No. 2, 2006, 73-86.
- [12] Rogers D. F. *An introduction to NURBS*. San Francisco: Morgan Kaufmann Publisher, 2001.
- [13] O. E. Balje, "Loss and flow path studies on centrifugal compressors-Part I", *ASME Journal of Engineering for Power*, Vol. 92, No. 2, 1970, 275-286.
- [14] G. Kamimoto, K. Hirai, "On the flow in the impeller of centrifugal type hydraulic machinery (1st report)". *Transaction of JSME*, Vol. 19, No. 85, 1953, 37-43.
- [15] Anonymous, *FLUENT 5 User's Guide, Volume 4*. Lebanon: Fluent Incorporated, 1998.
- [16] W. S. Ghaly, "A design method for turbomachinery blading in three-dimensional flow". *International Journal for Numerical Methods in Fluids*, Vol. 10, No. 2, 1990, 179-197.
- [17] M. Zangeneh, "A compressible three-dimensional design method for radial and mixed flow turbomachinery blades". *International Journal for Numerical Methods in Fluids*, Vol. 13, No. 5, 1991, 599-624.
- [18] J. E. Borges, "A proposed through-flow inverse method for the design of mixed-flow pumps". *International Journal for Numerical Methods in Fluids*, Vol. 17, No. 12, 1993, 1097-1114.
- [19] G. Y. Peng, S. L. Cao, M. Ishizuka, S. Hayama, "Design optimization of axial flow hydraulic turbine runner: Part I—an improved Q3D inverse method". *International Journal for Numerical Methods in Fluids*, Vol. 39, 2002, 517-531.
- [20] G. Y. Peng, S. L. Cao, M. Ishizuka, S. Hayama, "Design optimization of axial flow hydraulic turbine runner: Part II—multi-objective constrained optimization method". *International Journal for Numerical Methods in Fluids*, Vol. 39, 2002, 517-531.
- [21] G. Y. Peng, "A practical combined computation method of mean through-flow for 3d inverse design of hydraulic". *ASME Journal of Fluids Engineering*, Vol. 127, No. 6, 2005, 1183-1190.
- [22] S. Tan, W. R. Hawthorne, C. Wang, J. E. McCune, "Theory of blade design for large deflections: Part II—annular cascades". *ASME Journal of Engineering for Gas Turbine and Power*, Vol. 106, 1984, 354-365.
- [23] T. S. Luu, B. Viney, L. Bencherif, "Turbomachine blading with splitter blades designed by solving the inverse flow field problem". *Journal of Physics III France*, Vol. 2, 1992, 657-672.
- [24] R. M. Jenkins, D. A. Moore, "An inverse calculation technique for quasi-three-dimensional turbomachinery cascades". *Applied Mathematics and Computation*, 57, 1993, 197-204.
- [25] T. Dang, V. Isgro, "Euler-based inverse method for turbomachine blades part 1: two-dimensional cascades". *AIAA Journal*, Vol. 33, No. 12, 1995, 2309-2315.
- [26] T. Dang, V. Isgro, "Euler-based inverse method for turbomachine blades part 2: three-dimensional flows". *AIAA Journal*, Vol. 38, No. 11, 1995, 2007-2013.

CFD Simulations of Drag and Separation Flow Around Ellipsoids

Yazan Taamneh*

Department of Mechanical Engineering, Tafila Technical University P. O. Box 179, 66110 Tafila, Jordan

Abstract

Computational fluid dynamics (CFD) simulations are carried out for incompressible fluid flow around ellipsoid in laminar steady axisymmetric regime ($20 \leq Re \leq 200$). The ratio of the major to the minor axis of the ellipsoid are ranged over $a/b = 0.5$ to 2. A commercial finite volume package FLUENT was used to analyze and visualize the nature of the flow around ellipsoids of different axis ratio. The simulation results are presented in terms of skin friction coefficient, separation angles and drag coefficient. It was found that the total drag coefficient around the ellipsoid is strongly governed by the axis ratio as well as the Reynolds number. It was observed that the Reynolds number at which the separation first occur increase with axis ratio. Separation angles and drag coefficient for special case of a sphere ($AR = 1$) was found to be in good agreement with previous experimental results and with the standard drag curve. The present study has established that commercially-available software like FLUENT can provide a reasonable good solution of complicated flow structures including flow with separation.

© 2011 Jordan Journal of Mechanical and Industrial Engineering. All rights reserved

Keywords: CFD Simulation; Laminar Flow; Drag Coefficient ; Separation Angle.

Nomenclature

a [m] ellipsoid major diameter in the flow direction
 b [m] ellipsoid minor diameter in the direction normal to the flow
 AR [-] axis ratio a/b
 C_d [-] total drag coefficient
 C_f [-] friction drag coefficient
 C_p [-] pressure drag coefficient
 P [N/m²] pressure
 Re [-] Reynolds number
 U_∞ [m/s] free stream velocity
 V_x [m/s] x-component velocity
 V_r [m/s] r-component velocity

Greek Symbols

μ [Pa.s] fluid dynamic viscosity
 ρ [kg/m³] fluid density
 θ_s [degree] separation angle

1. Introduction

The flow separation around simple and complex bluff body is one of the most important and challenging problems in fluid mechanics. The separated flow around a body is difficult to predict and results in many undesirable

phenomena such as drag increase, lift loss and fluctuations in the pressure field, etc. The accuracy of the predicted flow field depends on model equations, numerical methods and grid spacing among other factors. Experimental investigations of the steady wake behind a sphere at low Reynolds numbers have been performed by [1,2]. They found that for Reynolds numbers less than 24 the flow around the sphere is perfectly laminar, no flow separation occurs, and the flow on the downstream side of the sphere is identical to that on the upstream side. The flow past a sphere over a larger range of Reynolds numbers have been investigated experimentally by [3,4]. They found that the flow was axisymmetric and stable up to $Re = 200$, while in [5] found the same behavior occurring up to $Re = 210$. These observations are in good agreement with the calculations of [6], who investigated the linear stability of the steady axisymmetric flow past a sphere and found that the flow undergoes a regular bifurcation at a Reynolds number of about 210 and results in the development of a non-axisymmetric wake.

The use of computational fluid dynamics codes to simulate the flow around geometrically complicated shapes such as airplanes, cars and ships has become standard engineering practice in the last few years. Therefore, several authors have developed numerical techniques for calculating viscous flow, applied them to a spheroid, and compared their predictions to the experimental results previously mentioned. The numerical work has developed from solutions of the boundary layer equations with a predetermined pressure distribution [7-

* Corresponding author: ytaamneh@yahoo.com.

12]. Numerical studies of the fluid flow past different shape of spheroid particles over the Reynolds number range, $1 \leq Re \leq 500$ at different aspect ratio are presented by [12]. They found that the effect of shape of particles on individual and total drag coefficient was small at low Reynolds number and magnifies with increasing Reynolds number. Separation points where the boundary layer leaves the surface were not clearly considered in their study. Direct numerical simulation based on spectral-type methods to simulate the flow between $Re = 25$ and $Re = 1000$ were carried out by [11]. Their simulations showed that the flow past a sphere is axisymmetric up to a Reynolds number of approximately 212, and that beyond this Reynolds number the flow undergoes a transition to three-dimensionality through a regular bifurcation.

There seems to be lack of computational works on flow separation around ellipsoid in axisymmetric flow regime. Therefore, this paper aims to provide a CFD simulation study of axisymmetric viscous laminar flow around ellipsoids by using commercial finite volume package FLUENT. Another sub goal of the present study is to test whether FLUENT, a commercial Computational Fluid Dynamics (CFD) software package, is capable of providing the solutions for the problem under consideration.

2. Theoretical Formulation

2.1. Governing equations

The governing equation for laminar 2D steady-state incompressible in axisymmetric geometry are the continuity equation and the two equations of motion:

$$\rho \left[\frac{\partial v_x}{\partial x} + \frac{\partial v_r}{\partial r} + \frac{v_r}{r} \right] = 0 \quad (1)$$

$$\rho \left[\frac{1}{r} \frac{\partial (rv_x^2)}{\partial x} + \frac{1}{r} \frac{\partial}{\partial r} (rv_x v_r) \right] = -\frac{\partial p}{\partial x} + \frac{1}{r} \frac{\partial}{\partial x} \left[r\mu \left(2 \frac{\partial v_x}{\partial x} - \frac{2}{3} (\nabla \cdot \vec{u}) \right) \right] + \frac{1}{r} \frac{\partial}{\partial r} \left[r\mu \left(\frac{\partial v_x}{\partial r} + \frac{\partial v_r}{\partial x} \right) \right] \quad (2)$$

$$\rho \left[\frac{1}{r} \frac{\partial (rv_r^2)}{\partial r} + \frac{1}{r} \frac{\partial}{\partial x} (rv_x v_r) \right] = -\frac{\partial p}{\partial r} + \frac{1}{r} \frac{\partial}{\partial r} \left[r\mu \left(2 \frac{\partial v_r}{\partial r} - \frac{2}{3} (\nabla \cdot \vec{u}) \right) \right] + \frac{1}{r} \frac{\partial}{\partial x} \left[r\mu \left(\frac{\partial v_r}{\partial x} + \frac{\partial v_x}{\partial r} \right) \right] - 2\mu \frac{v_r}{r^2} + \frac{2\mu}{3r} (\nabla \cdot \vec{u}) \quad (3)$$

where x is the axial coordinate, r is the radial coordinate, v_x is the axial velocity and v_r is the radial velocity, p is the static pressure, μ is the molecular viscosity, ρ is the density and

$\nabla \cdot \vec{u} = \frac{\partial v_x}{\partial x} + \frac{\partial v_r}{\partial r} + \frac{v_r}{r}$ no external body force is considered in this study.

2.2. Boundary conditions

The x -coordinate denote the direction of the bulk flow and along the major axis of ellipsoid. The r -coordinate is along the minor axis of the ellipsoid. Figure 1 shows the coordinate system for the 2-D ellipsoid model.

Since a half body section rotated about an axis parallel to the free stream velocity (axisymmetric body) is considered. The bottom boundary of the domain is modeled as an axis boundary.

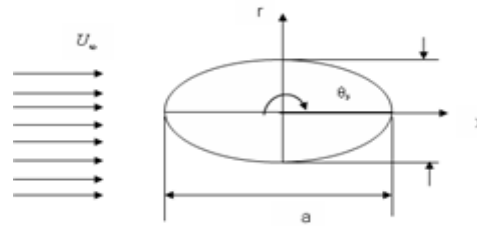


Figure 1. Schematic of the physical problem

The top and left boundaries of the domain are modeled as velocity inlet, the right boundary is modeled as a pressure out flow and the surface of the ellipsoid is modeled as a wall. Additionally, the no-slip boundary condition is assumed to hold at all fluid-solid interface, i.e. at the top surface of the ellipsoid. The boundary conditions which describing the current simulated computational domain as well as the surface boundary layer is depicted in Figure 2.

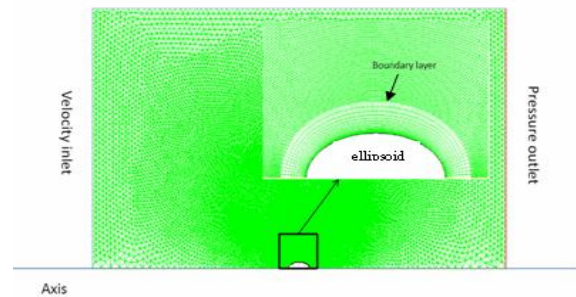


Figure 2. Solution domain and computational grid with boundary conditions and close up view of the boundary layer at $AR = 2$

3. Numerical Methods

A finite volume method is employed using a commercial software FLUENT 6.2 to solve the governing equations subject to specified boundary conditions. Since the boundary layer separation is intimately connected with the pressure and velocity distribution in the boundary layer, accurate separation point predication are dependent on accurate resolution of the boundary layer near the surface of the body. Therefore, for the purpose of grid construction, the computational domain for ellipsoid model is divided into two regions: the boundary layer region and the free stream region (see Figure 2). The boundary layers are attached to the ellipsoid and the direction of the boundary layer grid is defined such that the grids extended into the interior of the domains. More cells are constructed near the surface of the ellipsoid to compensate the high velocity gradient in the boundary layer region of the viscous flow. A commercial software GAMBIT is used for grid generation. The coupling between the pressure and velocity fields is achieved using PISO. A second order upwind schemes is used for the convection. Here in this study, following [13], we define the total drag coefficient, C_d the pressure drag

coefficient, C_p the skin friction coefficient, C_f and a Reynolds number, Re as follows:

$$C_d = \frac{2D}{\rho U_\infty^2 A}, C_p = \frac{2(p - p_\infty)}{\rho U_\infty^2 A} \tag{5}$$

$$C_f = \frac{2\tau_w}{\rho U_\infty^2 A} \text{ and } Re = \frac{a \cdot U_\infty \cdot \rho}{\mu}$$

where D , is the sum of the local skin friction and pressure drag, p_∞ is the pressure of the stream, A is appropriate reference area and U_∞ is free stream velocity. The grid independence is achieved by comparing the results of the different grid cell size. It was found that 75000 cells is satisfactory, and any increase beyond this size would lead to an insignificant change in the resulting solution.

4. Results and Discussion

Simulation results for axisymmetric laminar flow around sphere ($AR = 1$) are compared to experimental data to verify the validity of the CFD simulation solution. Figure 3 shows the total drag coefficient as a function of Reynolds number for special case of a sphere ($AR = 1$). As can be seen from Figure 3, there is an excellent agreement in the Reynolds number dependence of C_d between CFD simulations in this study and the experimental measured dependence by [7].

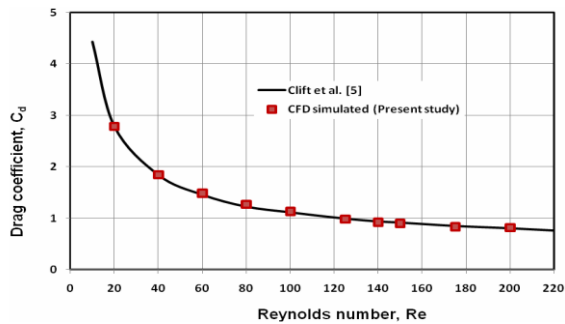


Figure 3. Comparison of computed drag coefficient with the experimental correlation of Clift et al. [5] for sphere ($AR = 1$).

The effects of Reynolds number on the total drag coefficient for ellipsoids of different axis ratio are shown in Figure 4.

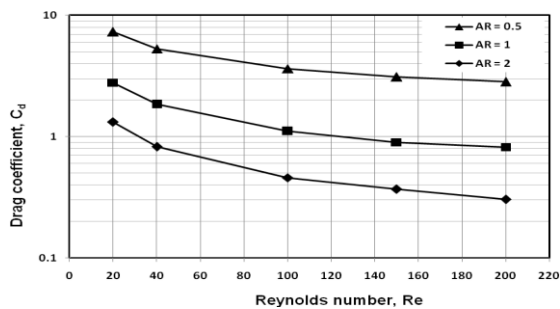


Figure 4. Variation of the total drag as a function of Reynolds number for various axis ratio.

It is clear that C_d values gradually decrease with increase in Reynolds number for all axis ratio. It can be seen that the ellipsoid of axis ratio $AR = 2$ exhibit the lowest drag coefficient due to the ellipsoid geometry. The simulated values of skin friction coefficient over the ellipsoid of different axis ratio at various Reynolds number is shown in Figure 5 (a-c).

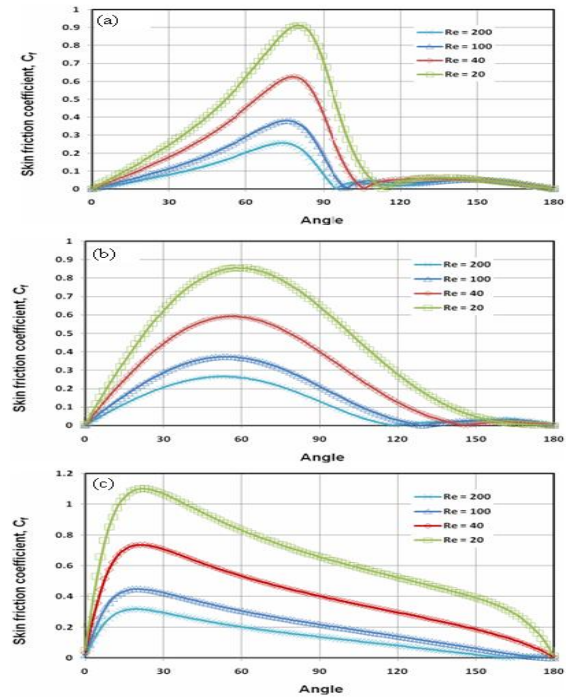


Figure 5. Skin friction coefficient on the surface of ellipsoid at different Reynolds numbers for (a) $AR = 0.5$, (b) $AR = 1$, (c) $AR = 2$.

It can be observed that the skin friction coefficient around the ellipsoid decreases by increasing the Reynolds number regardless of the value of axis ratio. This is due to the increase of the convection stream flow. The distribution of the skin friction coefficient identify the points where the flow leaves the surface i.e. $C_f \approx 0$. Since the point of separation itself is determined by the condition that the velocity gradient normal to the wall vanish ($\partial v_x / \partial r = 0$). It can be noted from Figure 5 (a) that the ellipsoid of axis ratio $AR = 0.5$ has always imposed to flow separation over the range of Reynolds number $20 \leq Re \leq 200$. It shows that the separation angle increases with the Reynolds number from 113.5° at $Re = 20$ to 95.29° at $Re = 200$ (separation angle measured from the front stagnation point). For special case of sphere $AR = 1$, as Reynolds number increase beyond $Re = 20$ the separation begin to occur Figure 5(b). For the ellipsoid of axis ratio $AR = 2$ there was no separation flow except at high Reynolds number $Re = 200$, Figure 5(c). As a result, the Reynolds number at which the separation first occur increase with axis ratio. Table 1 lists the values of the angular position of separation points for all axis ratio at various Reynolds number.

The numerical prediction of separation angle values for special case of sphere $AR = 1$ matched very close Rimon and Cheng [8]. Figure 6 (a-c) shows the velocity vectors around rear half of ellipsoid for different axis ratio at $Re = 200$. The separation region and vortex shedding are clearly visible near the rear half of ellipsoid. It can be seen that as the axis ratio increase the separation region tends to disappear. Figure 7 (a-c) shows the velocity vectors around the rear half of ellipsoid of axis ratio $AR = 0.5$ at various Reynolds number. It can be observed that as the Reynolds number increase the separation ring moves forward so that the attached recirculating wake widens and lengths.

Table 1. Angle of separation for viscous axisymmetric laminar flow around ellipsoids.

Reynolds number, Re	Separation points (in degrees, θ_s)			
	AR = 0.5	AR = 1	AR = 2	AR = 1, [8]
20	113.4454	No separation	No separation	No separation
40	105.8824	146.7227	No separation	145.02
100	98.31932	130.084	No separation	129.37
200	95.29411	117.9832	161.8487	116.2

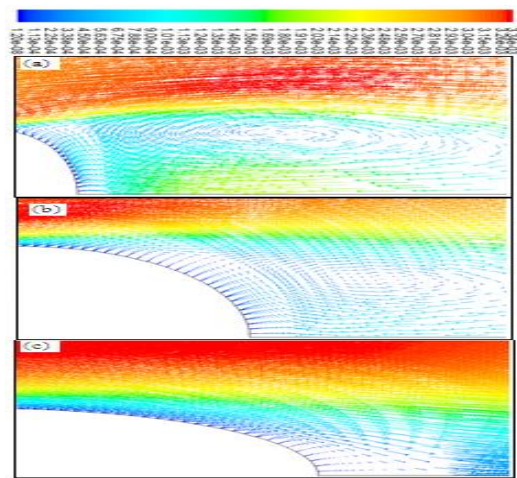


Figure 6: Velocity vectors around the rear part of the ellipsoids at Re = 200 for (a) AR = 0.5, (b) AR = 1, (c) AR = 2.

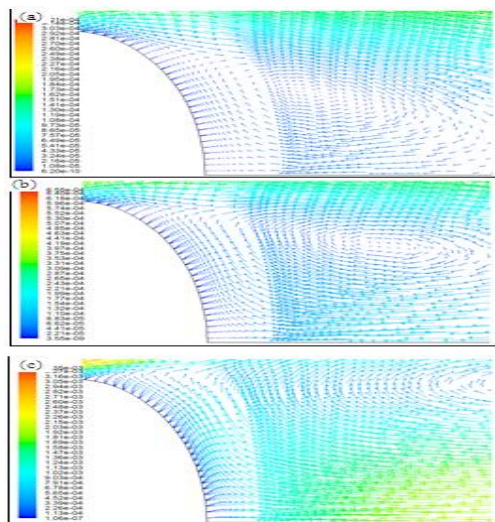


Figure 7: Velocity vectors around the rear part of the ellipsoid with AR = 0.5 for (a) Re = 20, (b) Re = 40, (c) Re = 200.

5. Conclusions

Drag and separation flow around ellipsoid in laminar steady axisymmetric region using Computational fluid dynamics (CFD) simulations are carried out. The nature of

the flow around ellipsoids of different axis ratio was visualized. The dependency of the total drag coefficient on the Reynolds number and axis ratio of ellipsoids was shown. It was found that the Reynolds number at which the separation first occur increase with axis ratio i.e. for $AR \geq 2$ there may be no separation region regardless of the Reynolds number. Comparison the simulation results with the experimental data validate the commercially-available software FLUENT in providing a reasonable good solution of complicated flow structures, including flow with separation.

References

- [1] S. Taneda, "Experimental Investigation of the Wake behind a Sphere at Low Reynolds Numbers". *J. Phys. Soc. Japan*, Vol. 11, No. 10, 1956, 1104-1108.
- [2] Nakamura, "Steady wake behind a sphere", *Phys. Fluids*, Vol. 19, No. 1, 1976, 5-8.
- [3] J. S. Wu, G. M. Faeth, "Sphere wakes in still surroundings at intermediate Reynolds numbers". *AIAA J.*, Vol. 31, No. 1, 1993, 1448-1455.
- [4] R. H. Margavey, R. L. Bishop,, "Transition ranges for three-dimensional wakes". *Can. J. Phys.*, Vol. 39, No. 1, 1961, 1418-1422.
- [5] Clift R, Grace J. R, Weber M. E. Bubbles, Drops and Particles. New York: Academic Press. 1978.
- [6] R. Natarajan, A. Acrivos, "The instability of the steady flow past spheres and disks". *J. Fluid Mech.*, Vol. 254, No. 3, 1993, 323-344.
- [7] E. Achenbach, "Experiments on the flow past spheres at very high Reynolds numbers". *J. Fluid Mech.*, Vol. 54, No. 3, 1972, 565-569.
- [8] Y. Rimon, S. I. Cheng, "Numerical solution of a uniform flow over a sphere at intermediate Reynolds number". *Phys. Fluid*, Vol. 12, No. 1, 1969, 949.
- [9] K. C. Wang, "Boundary layer over a blunt body at low incidence with circumferential flow". *J. Fluid Mech.*, Vol. 72, 1975, 39-65.
- [10] G. S. Constantinescu, H. Pasinato, Y. Wang, J. R. Forsythe, K. D. Squires, "Numerical Investigation of Flow Past a Prolate Spheroid". *ASME J. Fluids Eng.*, Vol. 124, 2002, 904-910.
- [11] H. W. Emmons, "The Laminar-Turbulent Transition in a Boundary Layer Part 1". *Journal of the Aeronautical Sciences*, Vol. 18, No. 7, 1951, 490-498.
- [12] N. N. Kumar, N. Kishore, "2-D Newtonian Flow past Ellipsoidal Particles at Moderate Reynolds Numbers". *Seventh International Conference on CFD in the Minerals and process Industries*, Australia, 2009.
- [13] Schlichting H. *Boundary layer Theory*, New York: McGraw-Hill; 1969.
- [14] M. M. Karim, M. M. Rahman, M. A. Alim, "Computation of Axisymmetric Turbulent Viscous Flow Around Sphere". *Journal of Scientific Research*, Vol. 1, No. 2, 2009, 209-219.
- [15] C. Chang, B. Liou, R. Chern, "An analytical and Numerical study of axisymmetric flow around spheroids". *J. Fluid Mech.*, Vol. 234, No. 5, 1992, 219-246.

Mhd Heat and Mass Transfer Free Convection Flow Near the Lower Stagnation Point of an Isothermal Cylinder Imbedded in Porous Domain with the Presence of Radiation

Ziya Uddin^{*,a}, Manoj Kumar^b

^a Department of Applied Sciences and Humanities ITM University, Gurgaon, India

^b Department of Mathematics, Statistics and Computer Science G. B. Pant University of Agriculture and Technology,
Pantnagar – 263 145, Uttarkhand, India

Abstract

Heat and mass transfer characteristics and the flow behavior on MHD flow near the lower stagnation point of a porous isothermal horizontal circular cylinder have been studied. The equations of conservation of mass, momentum, energy and concentration which govern the case study of heat and mass transfer flow have been obtained. These equations have been transformed into a system of non-dimensional coupled non-linear ordinary differential equations by using similarity transformations and finally solved by Runge-Kutta and shooting method. It has been assumed that the fluid is incompressible, absorbing-emitting radiation and viscous, with temperature dependent viscosity and temperature dependent thermal conductivity in the presence of radiation. Velocity profiles, temperature distributions and concentration distributions for the flow have been presented for various values of radiation parameter, viscosity variation parameter, thermal conductivity variation parameter, Prandtl number and Schmidt number. The skin friction factor, local Nusselt number and Sherwood number are also calculated for all the parameters involved in the problem. It has been observed that with the increase in Schmidt number skin friction and Nusselt number decrease, while Sherwood number increases.

© 2011 Jordan Journal of Mechanical and Industrial Engineering. All rights reserved

Keywords: MHD heat mass transfer; free convection; isothermal circular cylinder; radiation effect; variable thermal conductivity and viscosity; Runge-Kutta shooting technique.

Nomenclature

a	Curvature
b	Inertial drag coefficient
B_o	Magnetic intensity
C	Concentration
C_f	Skin friction
C_p	Specific heat at constant pressure
D	Mass diffusivity
f	Non-dimensional reduced stream function
Gm	Modified Grashoff number
Gr	Grashoff number
K	Porosity parameter
k	Thermal conductivity
k'	Permeability of porous media
M	Magnetic parameter
N	radiation parameter
Nf	Forchhiemer inertial porous parameter
Nu	Nusselt number
O	Stagnation point
Pr	Prandtl number
q_r	Radiative heat flux
q_w	Rate of heat transfer
Sc	Schmidt number

Sh	Sherwood number
So	Soret number
s_w	Rate of mass transfer
T	Temperature
u, v	Velocity components along X, Y directions
X, Y	distances along and perpendicular to the surface

Greek symbols

μ	Viscosity of the fluid
k_1	Mean absorption coefficient
β	Coefficient of thermal expansion
ε	Variable viscosity parameter
η	Dimensionless distance
θ	Non-dimensional temperature
ν	kinematic viscosity of the fluid
ρ	Density of the fluid
σ	Electrical conductivity
σ_1	Stefan Boltzmann constant
Φ	Non-dimensional concentration
ψ	Stream function
ω	Variable thermal conductivity parameter

* Corresponding author: ziya_dd@rediffmail.com.

Subscripts

w	wall of cylinder
∞	Distance far away from the surface

Superscript

'	Differentiation with respect to η
---	--

1. Introduction

The study of flow problems which involve the interaction of several phenomena, has a wide range of applications in the field of Science and Technology. One such study is related to the effect of free convection MHD flow, which plays an important role in Agriculture, Engineering and Petroleum industries. The problem of free convection under the influence of magnetic field has attracted many researchers in view of its application in Geophysics, Astrophysics, geological formations, thermal recovery of oil, and in assessment of aquifers, geothermal reservoirs and underground nuclear waste storage site, etc. The heat transfer in porous media has great practical importance in geophysics and energy related engineering problems. These include the utilization of geothermal energy, the control of pollutants in ground water, solar power collectors, high performance insulations of buildings, food processing, casting and welding of a manufacturing process, etc.

The effect of temperature dependent viscosity on natural convection of fluid from heated vertical wavy surface was studied by [1]. In case of vertical cone, this effect was studied by [2]. Nazar et al. [3] studied the free convection boundary layer on an isothermal horizontal circular cylinder in a micropolar fluid. In case of horizontal cylinder the radiation-conduction interaction on mixed convection was investigated by [4]. Kafoussius et al. [5] studied the combined free and forced convection laminar boundary layer past a vertical isothermal flat plate with temperature dependent viscosity. In porous media the effect of viscosity variation was considered by [6] and [7]. Free convection boundary layer on cylinders of elliptic cross section was studied by [8]. Harris et al. [9] studied the transient free convection near the lower stagnation point of a cylindrical surface subjected to a sudden change in surface temperature. Effect of aligned magnetic field on steady viscous flow past a circular cylinder was studied by [10]. Free convection and mixed convection about a circular cylinder was studied by the authors [11] and [12] respectively. The effect of variable viscosity on the fluid flow past a horizontal cylinder was also investigated by [13]. The combined heat and mass transfer along a vertical moving cylinder was studied by [14]. In this analysis both uniform wall temperature and uniform heat flux cases have been included. Bhargava et al. [15] found the finite element solution for non-newtonian pulsatile flow in a non-darcian porous medium conduit, they used the Darcy-Forchheimer model to formulate the problem. Transient analysis of heat and mass transfer by natural convection in power law fluid past a vertical plate immersed in a porous medium is studied by [16]. Rashad [17] studied the effect of thermal radiation on the steady laminar flow past a vertical plate immersed in a porous medium. He used the Rosseland approximation to incorporate the effect of radiation, in the mathematical model of the problem.

It is observed that MHD heat and mass transfer free convection flow near the lower stagnation point of an isothermal horizontal circular cylinder in presence of radiation and temperature dependent fluid properties has given a very scant attention in the literature. Hence in the present study the effect of radiation with temperature dependent thermal conductivity and temperature dependent viscosity on MHD heat and mass transfer free convection flow near the lower stagnation point of a porous, isothermal horizontal circular cylinder has been considered.

2. Formulation

Consider a two dimensional MHD free convection flow of a viscous, incompressible, electrically conducting fluid absorbing-emitting radiation, over a uniformly heated circular cylinder of radius " r ". It is assumed that the surface temperature of the porous cylinder is T_w and T_∞ is the ambient temperature of the fluid. A uniform radial magnetic field of strength B_0 is applied perpendicular to the surface of the cylinder. A locally orthogonal coordinate system is chosen with origin O , at lower stagnation point and X and Y denoting the distances measured along and perpendicular to the surface respectively. If " a " is the curvature of the body surface, then by the choice of axes, " a " is the principal curvature at O . The physical model and coordinate system is shown in the figure 1.

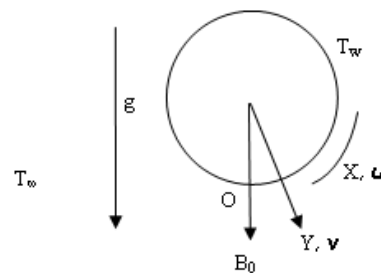


Figure 1. Physical model and coordinate system

We assume that (i) the fluid has constant kinematic viscosity and the Boussinesq approximation may be adopted for the steady laminar boundary layer flow, (ii) the magnetic Reynolds number is assumed to be small so that the induced magnetic field is negligible in comparison to the applied magnetic field, (iii) the cylinder is considered to be non-electrically conducting and the hall effect has been neglected, (iv) the joule heating effect has been neglected, and (v) the fluid is considered to be gray absorbing-emitting radiations but non scattering medium and the Rosseland approximation is used to describe the radiative heat flux in the x-direction is considered negligible in comparison to y-direction. This approximation is valid at points far from the boundary surface, and is good for intensive absorption, that is, for an optically thick boundary layer. The Darcy-Forchheimer model is used to describe the flow in porous media. Under the usual Boussinesq approximation, the equations that govern the flow are:

Equation of Continuity:

$$\frac{\partial u}{\partial x} + \frac{\partial v}{\partial y} = 0 \tag{1}$$

Equation of Momentum

$$u \frac{\partial u}{\partial x} + v \frac{\partial u}{\partial y} = g\beta(T - T_\infty)ax + g\beta_c(C - C_\infty)ax + \frac{1}{\rho} \frac{\partial}{\partial y} \left(\mu(T) \frac{\partial u}{\partial y} \right) - \frac{\sigma B_0^2 u}{\rho} - \frac{\mu u}{\rho k'} - bu^2 \tag{2}$$

Equation of Energy:

$$\rho C_p \left(u \frac{\partial T}{\partial x} + v \frac{\partial T}{\partial y} \right) = \frac{\partial}{\partial y} \left(k(T) \frac{\partial T}{\partial y} \right) - \left(\frac{\partial q_r}{\partial y} \right) \tag{3}$$

Equation of Diffusion:

$$\left(u \frac{\partial C}{\partial x} + v \frac{\partial C}{\partial y} \right) = D \frac{\partial^2 C}{\partial y^2} \tag{4}$$

where u and v denote the fluid velocity components in the x and y directions respectively, T is the fluid temperature, C is fluid concentration, g is the magnitude of acceleration due to gravity, β is the coefficient of thermal expansion, ρ is the density of the fluid, σ is the fluid electrical conductivity, B_0 is the strength of applied magnetic field, k' is the permeability of porous medium, b is the Forchheimer geometrical (inertial drag) coefficient, C_p is specific heat at constant pressure, $\mu(T)$ is the temperature dependent viscosity of the fluid, $k(T)$ is the temperature dependent thermal conductivity and D is mass diffusivity. The term $g\beta(T - T_\infty)ax$ in the momentum equation arises from the component of buoyancy force in the x direction in the vicinity of O and the last term qr in the energy equation represent the radiative heat flux in y direction.

The radiative heat flux q_r under Rosseland approximation by Brewster [18] has the form:

$$q_r = -\frac{4\sigma_1}{3k_1} \frac{\partial T^4}{\partial y} \tag{5}$$

where σ_1 is Stefan-Boltzmann constant and k_1 is the mean absorption coefficient.

We assume that the temperature differences within the flow are so small that T^4 can be expressed as a linear function of T_∞ . This is obtained by expanding T^4 in a Taylor series about T_∞ and neglecting the higher order terms. Thus we get:

$$T^4 \cong 4T_\infty^3 T - 3T_\infty^4 \tag{6}$$

The initial and boundary conditions are:

$$u=0, v=0, T=T_w, C=C_w \text{ at } y=0 \tag{7a}$$

$$u \rightarrow 0, T \rightarrow T_\infty, C \rightarrow C_\infty \text{ as } y \rightarrow \infty \tag{7b}$$

It is assumed that the viscosity $\mu(T)$ and thermal conductivity $k(T)$ varies with temperature as follows:

$$\mu(T) = \frac{\mu_\infty}{1 + \gamma(T - T_\infty)} \tag{8}$$

$$k(T) = k_\infty (1 + b(T - T_\infty)) \tag{9}$$

The system of partial differential equations (1-4) and initial and boundary conditions (7) after introducing equations (5-6) and (8-9) can be reduced to a system of

semi-similar equations by employing the following transformations:

$$\psi = Gr^{\frac{1}{4}} axvf(\eta), \quad \eta = Gr^{\frac{1}{4}} ay, \quad \theta(\eta) = \frac{T - T_\infty}{T_w - T_\infty}, \tag{10a}$$

$$\phi(\eta) = \frac{C - C_\infty}{C_w - C_\infty}, \quad Gr = \frac{g\beta(T_w - T_\infty)}{a^3 \nu^2}, \quad Gm = \frac{g\beta_c(C_w - C_\infty)}{a^3 \nu^2} \tag{10b}$$

where ψ is the stream function, f is non-dimensional reduced stream function, θ is non-dimensional reduced temperature, C is non-dimensional reduced concentration, Gr is Grashoff number and Gm is modified Grashoff number.

Thus, the reduced equations in non-dimensional are:

$$f''' = (1 + \epsilon\theta) \left[(1 - Nf)f'' - ff'' + \frac{\epsilon}{(1 + \epsilon\theta)^2} \theta' f' + \frac{1}{\sqrt{Gr}} \left(M + \frac{1}{(1 + \epsilon\theta)K} \right) f' - \theta - \frac{Gm}{Gr} \phi \right] \tag{11}$$

$$\theta'' = -\frac{3N}{4 + 3N(1 + \omega\theta)} [\text{Pr. f. } \theta' + \omega\theta'^2] \tag{12}$$

$$\phi'' = -Sc. f. \phi' \tag{13}$$

Here, $\epsilon = \gamma(T_w - T_\infty)$ is variable viscosity parameter, $\omega = b(T_w - T_\infty)$ is variable thermal conductivity parameter, $N = \frac{k_1 k_\infty}{4\sigma_1 T_\infty^3}$ is radiation parameter, $M = \frac{\sigma B_0^2 a^2}{\mu_\infty}$ is magnetic parameter, $K = k'a^2$ is porosity parameter, $Nf = bx$ is Forchheimer inertial porous parameter, $Pr = \frac{k_\infty}{\mu_\infty C_p}$ is

Prandtl number, $Sc = \frac{\nu}{D}$ is Schmidt number and prime (') denote the differentiation with respect to η .

The corresponding initial and boundary conditions are:

$$f(0) = 0, \quad f'(0) = 0, \quad \theta(0) = 1, \quad \phi(0) = 1 \tag{14a}$$

$$f(\infty) \rightarrow 0, \quad \theta(\infty) \rightarrow 0, \quad \phi(\infty) \rightarrow 0 \tag{14b}$$

In the absence of magnetic field, radiation and porosity and at $Gm=0$, eq. (11) and eq.(12) reduce to the equations given by Md. Mamun Molla et al. [13] as follows:

$$f''' = (1 + \epsilon\theta) \left[f'^2 - ff'' + \frac{\epsilon}{(1 + \epsilon\theta)^2} \theta' f' - \theta \right] \tag{15a}$$

$$\theta'' = -Pr. f. \theta' \tag{15b}$$

Keeping in view of engineering aspects, the most important characteristics of the flow are local surface heat flux (Nusselt number), local surface mass flux (Sherwood number) and skin-friction, which can be written as

$$Nu = \frac{Gr^{-1/4}}{ak_\infty(T_w - T_\infty)} q_w, \quad Mu = \frac{Gr^{-1/4}}{aD(C_w - C_\infty)} S_w, \tag{15}$$

$$C_f = \frac{Gr^{-3/4}}{a^3 \nu x} \tau_w$$

where $q_w = -\left(k \frac{\partial T}{\partial y}\right)_{y=0}$ is rate of heat transfer,

$S_w = -\left(D \frac{\partial C}{\partial y}\right)_{y=0}$ is rate of mass transfer and,

$\tau_w = \left(\mu \frac{\partial u}{\partial y}\right)_{y=0}$ is local wall shear stress.

Using the variables equations (8)-(10) and initial and boundary conditions (14a, 14b), we get the following expressions for the Nusselt number, Sherwood number and skin-friction:

$$\begin{aligned} Nu &= -(1 + \omega)\theta'(0), Sh = -\phi'(0) \\ C_f &= \frac{1}{(1+\epsilon)} f''(0) \end{aligned} \quad (16)$$

3. Results And Discussion

The equations (11-13) with initial and boundary conditions (14) have been solved using Runge-Kutta and Shooting method. Taking $\Delta\eta=0.05$ shooting technique has been applied for getting missing boundary conditions. The value of dependent variable is calculated at the terminal point by adopting fourth-order Runge-Kutta method within an admissible tolerance viz., of order 10^{-6} .

In the absence of magnetic field, porosity and radiation and at $Gm=0$, $\epsilon=0$ and $Nf=0$ the value of $-\theta'(0)$ is 0.4212, the value of $-\theta'(0)$ found by Merkin [10] was 0.4214, by Nazar [14] it was found to be 0.4214 and by Md. Mamun Molla [10] it has been calculated to 0.4241. This shows that our results are in good agreement with these three solutions.

For several values of the dimensionless parameters, values of dimensionless velocity $f(\eta)$ and dimensionless temperature $\theta(\eta)$ have been computed and are presented in figures (2-7). figures (2,3) show the effects of variable viscosity parameter and radiation parameter on velocity and temperature respectively.

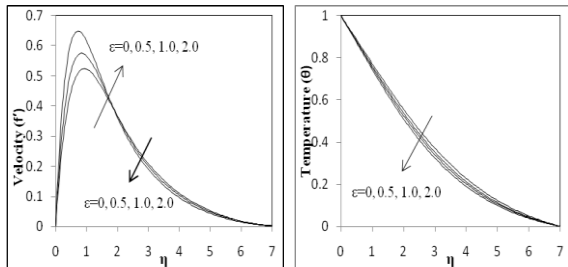


Figure 2. Velocity and Temperature for different values of ϵ at $Gr=1$, $Gm=K=N=Sc=1$, $M=\omega=0.5$ and $Pr=0.7$

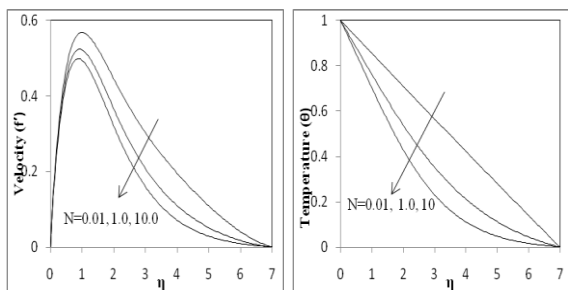


Figure 3. Velocity and Temperature for different values of ϵ at $Gr=1$, $Gm=K=N=Sc=1$, $M=\omega=0.5$ and $Pr=0.71$

It is seen from the figure (2) that the velocity increases with the increase in viscosity parameter, but after a certain distance from the surface of cylinder it decreases. It is also noticed that temperature decreases uniformly with an increase in viscosity parameter. figure (3) depicts the effect of radiation parameter and results that velocity and

temperature both decrease with the increase in radiation parameter. The effects of thermal conductivity parameter and Schmidt number on velocity as well as temperature are shown in figures (4,5).

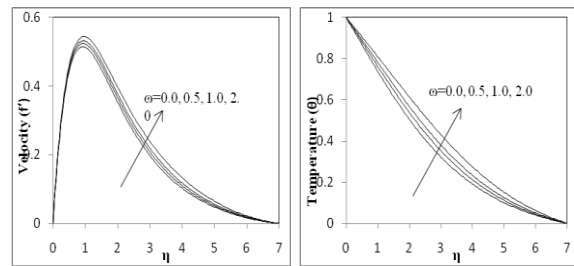


Figure 4 Velocity and Temperature for different values of ϵ at $Gr=1$, $Gm=K=N=Sc=1$, $M=\omega=0.5$ and $Pr=0.71$

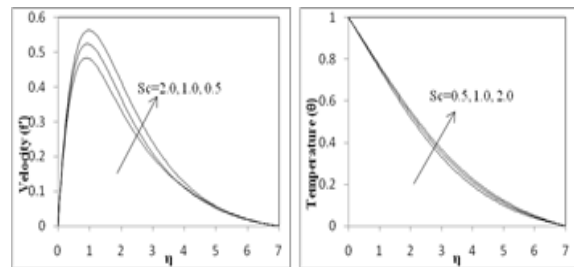


Figure 5. Velocity and Temperature for various values of Sc at $Gr=Gm=K=N=1$, $\epsilon=\omega=M=0.5$ and $Pr=0.71$

It is noticed that velocity and temperature both increase with the increase in thermal conductivity parameter. This is because as thermal conductivity parameter ω increases, the thermal conductivity of the fluid increases. This increase in the fluid thermal conductivity increases the fluid temperature and accordingly its velocity. Moreover, it is obvious that neglecting the variation of fluid thermal conductivity for high temperature differences introduces a substantial error. This error has been shown by plotting the dimensionless velocity and temperature for $\omega=0$. On increasing the Schmidt number the velocity decreases but temperature increases. The effects of Prandtl number on dimensionless velocity and temperature have been shown in figure (6).

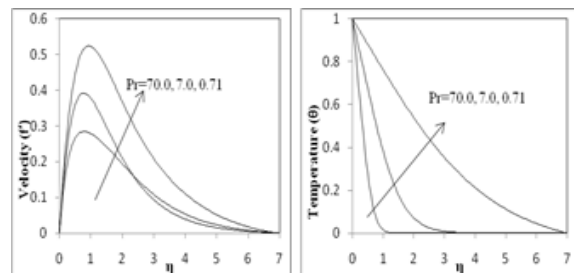


Figure 6. Velocity and Temperature for various values of Pr at $Gr=Gm=Sc=K=N=1$, $\omega=\epsilon=M=0.5$

It is clear that thermal boundary layer thickness decreases sharply with the increase in Prandtl number. Also the momentum boundary layer thickness decreases with the increase in Prandtl number from $Pr=0.71$ to $Pr=7.0$, but for $Pr=70.0$ the velocity is smaller than in the case of $Pr=7.0$ in the neighborhood of the cylinder and afterwards it increases. Figure (7) shows the velocity distribution for various values of Nf i.e. Forchhiemer parameter. A rise in Nf increases the velocity near the surface of the cylinder, but if we move longitudinally far away from the cylinder a

rise in N_f depresses the velocity slightly and there is a slight depression in temperature for an increase in the N_f value for all the distances.

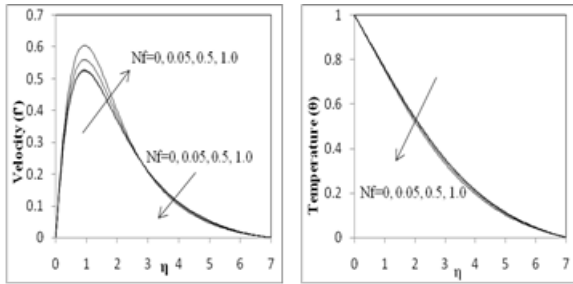


Figure 7. Velocity and Temperature for various values of N_f at $Gr=Gm=K=1$, $\omega=\epsilon=M=0.5$ and $Pr=0.71$

The effects of various dimensionless parameters on dimensionless concentration $\Phi(\eta)$ are shown in figures (8-10). From all these figures it is clear that the concentration decreases sharply as we move away from the surface. The effects of Prandtl number and thermal conductivity parameter are shown in figure (8), which depicts that the concentration boundary layer thickness increases with the increase in Prandtl number and there is a slight decrease in the concentration with the increase in thermal conductivity parameter. The variation of concentration with the change in the values of Schmidt number and viscosity parameter has been shown in figure (9).

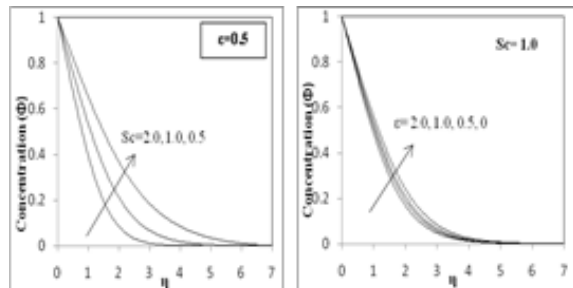


Figure 8. Concentration for various values of Sc and ϵ at $Gr=Gm=K=N=1$, $\omega=M=0.5$ and $Pr=0.71$

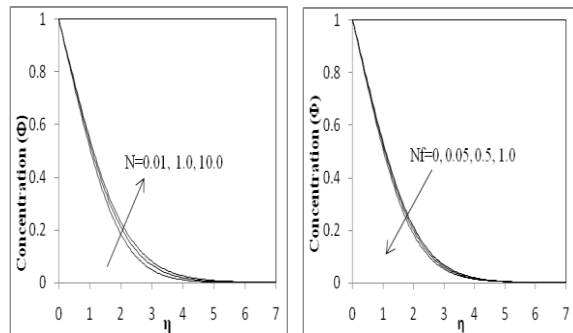


Figure 9. Concentration for various values of N and N_f at $Gr=Gm=K=1$, $\omega=\epsilon=M=0.5$ and $Pr=0.71$

It is seen that with the increase in Schmidt number concentration boundary layer thickness decreases. Also it depicts that the dimensionless concentration decreases with an increase in viscosity parameter. Figure (10) shows the effect of radiation parameter and Forchheimer parameter on concentration distribution and results that concentration increases with the increase in radiation parameter, and there is a slight depression with with the increase in N_f , but this depression is negligible.

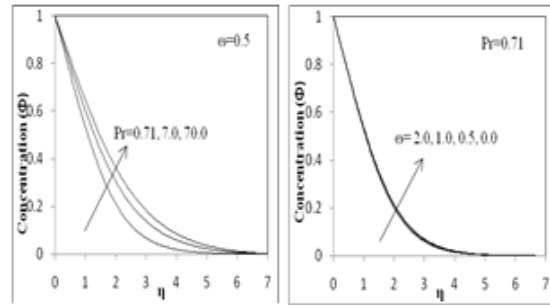


Figure 10. Concentration for various values of Pr and ω at $Gr=Gm=K=N=1$, $\omega=\epsilon=M=0.5$

The numerical values of $f''(0)$, $-\theta'(0)$ and $-\Phi'(0)$ have been presented in tabular form in table 1 for different values of various dimensionless parameters ϵ , M , K , ω , N , Sc , N_f and Pr at $Gr=Gm=1.0$. It is observed that dimensionless wall velocity gradient $f''(0)$ increases as ϵ , K , N_f and ω increase, while it decreases with the increase in M , N , Sc and Pr . Moreover, the value of $-\theta'(0)$ decreases with the increase in M , Sc and ω , while it increases with the increase in K , ϵ , N , N_f and Pr . Also it is seen that the value of $-\Phi'(0)$ increases with the increase in ϵ , ω , K , N_f and Sc and it decreases with the increase in N , M and Pr .

Table 1 Numerical values of $f''(0)$, $-\theta'(0)$ and $-\Phi'(0)$ for different values of non-dimensional parameters at $Gr=Gm=1.0$

ϵ	ω	N	M	K	Sc	Pr	N_f	$f''(0)$	$-\theta'(0)$	$-\Phi'(0)$
0	0.5	1.0	0.5	1.0	1.0	0.71	0.05	1.134486	0.2241	0.4530
0.5	0.5	1.0	0.5	1.0	1.0	0.71	0.05	1.520394	0.2353	0.4876
2.0	0.5	1.0	0.5	1.0	1.0	0.71	0.05	2.433411	0.2536	0.5454
0.5	2.0	1.0	0.5	1.0	1.0	0.71	0.05	1.541600	0.1839	0.4975
0.5	0.5	0.01	0.5	1.0	1.0	0.71	0.05	1.563953	0.1449	0.5100
0.5	0.5	10.0	0.5	1.0	1.0	0.71	0.05	1.493160	0.2889	0.4725
0.5	0.5	1.0	1.5	1.0	1.0	0.71	0.05	1.3064126	0.2147	0.4374
0.5	0.5	1.0	0.5	3.0	1.0	0.71	0.05	1.690260	0.2528	0.5253
0.5	0.5	1.0	0.5	1.0	0.5	0.71	0.05	1.572565	0.2444	0.3563
0.5	0.5	1.0	0.5	1.0	2.0	0.71	0.05	1.460637	0.2276	0.6550
0.5	0.5	1.0	0.5	1.0	1.0	7.0	0.05	1.356362	0.6376	0.4119
0.5	0.5	1.0	0.5	1.0	1.0	70.0	0.05	1.154725	1.5134	0.3633
0.5	0.5	1.0	0.5	1.0	1.0	0.71	0	1.515020	0.2348	0.4865
0.5	0.5	1.0	0.5	1.0	1.0	0.71	1.0	1.649130	0.2465	0.5162

4. Conclusion

In this work we used darcy Forchheimer model to formulate the problem. The effect of Radiation, Porosity, Variable thermal conductivity, Variable Viscosity, Magnetic field and Prandtl number has been included in this analysis. The governing nonlinear equations have been solved by using Runge-Kutta and Shooting method. It was found that:

1. Skin friction factor increases with the increasing porosity and thermal conductivity, while this is reduced with the increase in applied magnetic field, viscosity and radiation.
2. Rate of heat transfer (Nusselt number) increases with the increase in the porosity, radiation and Prandtl number, while it decreases with the increase in Magnetic field, viscosity and thermal conductivity.
3. Rate of mass transfer (Sherwood number) increases with the increase in thermal conductivity and porosity, while it decreases with the increase in viscosity, applied magnetic field and radiation.

Acknowledgements

We would like to thank to the reviewers for their encouraging comments and constructive suggestions to improve the manuscript.

References

- [1] M. A. Hossain, S. Kabir and D. A. S. Rees, "Natural convection of fluid with temperature dependent viscosity from heated vertical wavy surface". ZAMP, Vol. 53, 2002, 48-52.
- [2] M. A. Hossain, M. S. Munir and I. Pop, "Natural convection flow of viscous fluid with viscosity inversely proportional to linear function of temperature from a vertical cone". Int J Thermal Sci, Vol. 40, 2001, 366-371.
- [3] R. Nazar, N. Amin and I. Pop, "Free convection boundary layer on an isothermal horizontal circular cylinder in a micro-polar fluid". 12th international conference Heat Transfer. In., 2002.
- [4] M. A. Hossain, M. Kutubuddin and I. Pop, "Radiation-conduction interaction on mixed convection past a horizontal circular cylinder". Int J Heat Mass transfer, Vol. 35, 1999, 307-314.
- [5] N. G. Kafoussius and D. A. S. Rees, "Numerical study of the combined free and forced convective laminar boundary layer flow past a vertical isothermal flat plate with temperature dependent viscosity". Acta Mech, Vol. 127, 1998, 39-50.
- [6] J. Gray, D. R. Kassory and H. Tadjeran, "The effect of significant viscosity variation on convective heat transport in water saturated porous media". J Fluid Mech, Vol. 117, 1982, 233-248.
- [7] N. K. Mehta and S. Sood, "Transient free convection flow with temperature dependent viscosity in a fluid saturated porous media". Int J Eng Sci, Vol. 30, 1992, 1083-1087.
- [8] J. H. Merkin, "Free convection boundary layer on cylinders of elliptic cross section". ASME J Heat Transfer, Vol. 99, 1977, 453-457.
- [9] S. D. Harris and D. B. Ingham, "Transient free convection near the lower stagnation point of a cylindrical surface subjected to a sudden change in surface temperature". Int Comm. Heat Transfer, Vol. 27, 2000, 1091-1100.
- [10] T. V. S. Sekhar, R. Sivakumar, H. Kumar and T. V. R. Ravikumar, "Effect of aligned magnetic field on the steady viscous flow past a circular cylinder". App Math Model, Vol. 31, 2007, 130-139.
- [11] J. H. Merkin, "Free convection boundary layer on an isothermal horizontal circular cylinder". ASME/AIChE, heat transfer conference, St. Louis, MO, 9-11 August, 1976.
- [12] J. H. Merkin, "Mixed convection a horizontal circular cylinder". Int J Heat Mass Transfer, Vol. 20, 1977, 73-77.
- [13] Md. M. Molla, Md. Anwar Hossain and Gorla Rama Subba Reddy, "Natural convection flow from an isothermal horizontal circular cylinder with temperature dependent viscosity". Heat Mass Transfer, Vol. 41, 2005, 594-598.
- [14] H. S. Takhar, A. J. Chamka and G. Nath, "Combined heat and mass transfer along a vertical moving cylinder with a free stream". Heat Mass Transfer, Vol. 36, 2000, 237-246.
- [15] R. Bhargava, H. S. Takhar, S. Rawat, Tasveer A. Beg and O. anwar beg, "Finite element solutions for non-Newtonian pulsatile flow in a non-darcian porous medium conduit". Nonlinear Analysis: Modelling and Control, Vol. 12, No. 3, 2007, 317-327.
- [16] Naseer S. Elgazery, "Transient analysis of heat and mass transfer by natural convection in power law fluid past a vertical plate immersed in a porous medium (numerical study)". Applications and Applied Mathematics, Vol. 3, No. 2, 2008, 267-285.
- [17] Rashad, A. M., "Perturbation analysis of radiative effect on free convection flow in the presence of pressure work and viscous dissipation". Communication in nonlinear sciences and numerical simulation, Vol. 14, 2009, 140-153.
- [18] Brewster, M. Q. Thermal Radiative Transfer and Properties. 2nd ed. New York: John Wiley and Sons; 1992.

A Correlation for the Prediction of Nucleate Pool Boiling Performance of Pure Liquids from Enhanced Tubes

Ali H. Tarrad*

Department of Mechanical Engineering, College of Engineering,

Al-Mustansiriya University, Baghdad, P.O. Box: 14150, Iraq

Abstract

This investigation is devoted to study the enhancement factor of single enhanced tubes boiling pure liquids. Two surfaces of the integral machined structure; Gewa-T and low finned, tubes were considered. A new correlation for the estimation of the heat transfer coefficient in the nucleate region was developed based on the Buckingham (π) theorem for these tubes. The enhancement factor is a strong function of the fin shape of the enhanced surface structure and boiling liquids physical properties. Five liquids boiling at atmospheric pressure were considered, R-113, n-pentane, ethanol, water and R-11, for a heat flux in the range between (10) and (50) kW/m². The total mean absolute errors of the enhancement factors were (6%) and (9%) for the low finned and Gewa-T surfaces respectively. The present correlation showed a good agreement with the available experimental data in the literatures for the nucleate pool boiling heat transfer coefficient. It correlated the available data with a corresponding total mean absolute errors were (9.5%) and (13.5 %) for the low finned and Gewa-T surfaces respectively.

© 2011 Jordan Journal of Mechanical and Industrial Engineering. All rights reserved

Keywords: Nucleate Boiling; Performance; Enhancement Factor; Correlation; Machined Tube.

Nomenclature:

$C_{S,F}$: Liquid-Surface Contribution Factor ineq.(13.c)
(Dimensionless)
 C_I : Empirical Constant in Equations
 cp : Specific Heat of Fluid, (kJ/kg K)
 d : Tube Diameter, (m)
 h_{fg} : Heat of Vaporization, (kJ/kg)
 k : Thermal Conductivity of Fluid, (W/m.K)
 m : Constant in eq. (13.c), (Dimensionless)
 n : Constant in eq.(13.c), (dimensionless)
 N : Number of Data Points, (Dimensionless)
 p : Process Operating Pressure, (kPa)
 q : Heat Flux Density, (kW/m²)
 q_{ref} : Reference Heat Flux in eq.(5), (kW/m²)
 T : Temperature, (C°)
 ΔT : Wall Superheat, (deg C)

Greeks

α : Nucleate Boiling Heat transfer Coefficient,
(kW/m² K)
 η : Enhancement Factor of Boiling Heat Transfer
Coefficient,(Dimensionless)
 μ : Viscosity of Fluid, (Pa.s)
 ρ : Density of Fluid, (kg/m³)
 σ : Surface Tension, (N/m)

Subscripts

c : Critical Value
 $enh.$: Enhanced surface Value
 $exp.$: Experimental Value
 l : Liquid
 $L-F$: Low Finned Surface
 o : Outside
 $pla.$: Plain Tube Value
 $pred.$: Predicted Value
 r : Reduced or Measured at Fin Root

1. Introduction

It is well known that the surface structure affects the pool boiling heat transfer from a heater surface. The number and size distribution of cavities present on a heater surface affect the nucleation characteristics. The early work of Jakob and Fritz [1] showed that the rough surfaces exhibited a temporary improvement in the boiling heat transfer performance. Courty and Froust [2] found that the roughness has a strong influence on the performance of the heating element boiling liquid. The above argument has been proved either experimentally or theoretically by Berenson [3], Kurihara and Myers [4], Griffith and Wallis [5] and many other investigators.

At the present time there are quite a number of enhanced surfaces available commercially, some of them

* Corresponding author: dr.alitarrad@yahoo.com

are shown in figure (1). They are either integrally machined or a porous coating surfaces. Gottzmann et al. [6] reported that a tenfold enhancement in the boiling heat transfer coefficient was obtained when the High Flux surface was compared with those of the smooth plain tube. Later Gottzmann [7] proved that the High Flux surface has a remarkable resistance to fouling in a long term operation.

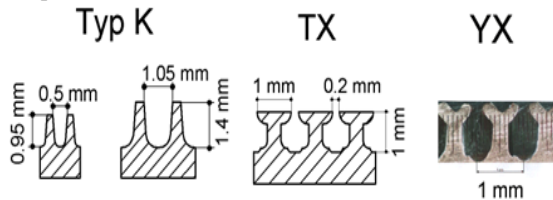


Figure 1.a): Typical Enhanced Gewa-T tube Structure

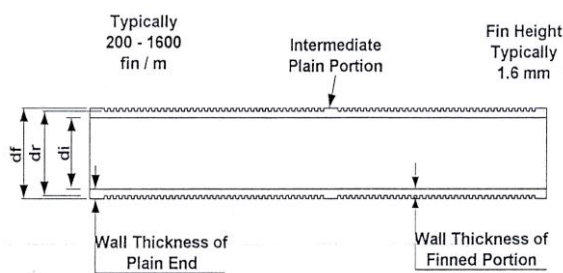


Figure 1.b): Typical Enhanced Low Finned Tube Structure

Marto and Lepere [8] showed that the pool boiling heat transfer coefficient when boiling R-113 and FC-72 was strongly related to the liquid-surface combination factor, the past history of the surface and the operating liquid properties.

Yilmaz et al. [9] found that the enhanced surfaces improved the boiling heat transfer coefficients of p-xylene and isopropyl alcohol by an order of magnitude approaching (10) times when compared with those of the smooth surface depending on the operating conditions and boiling liquid type. Yilmaz and Westwater [10] concluded that the enhancement in heat transfer performance depends on the enhanced surface structure and liquid properties.

Marto and Hernandez [11] reported an enhancement factor of about three times when boiling R-113 on the Gewa-T surface at atmospheric pressure. Hahne and Muller [12] have found an improvement in the boiling heat transfer coefficient of R-11 when compared the finned tubes with that of the smooth one. Tarrad [13] has concluded that the enhancement factor of the enhanced tubes is a function of the liquid thermal properties, binary mixtures or pure liquids, and the enhanced tube structure.

Kandikar and Howell [14] reported an increase in bubble activity on a micro fin surface when compared to a plain surface for flow boiling investigation. Yuming et al. [15] made a comparison between the smooth tube and enhanced tubes for bubble growth rate, departure diameter, frequency, active site density and rise velocity. The effects of physical properties on the bubble dynamics were clear especially the departure diameter and the nucleation site density.

The present work establishes a correlation for the prediction of the enhancement factor and the nucleate pool boiling heat transfer coefficient of pure liquids from two

types of commercially available enhanced tubes, known as *low finned* and *Gewa-T* surfaces.

2. Available Correlations:

The formulation of the nucleate pool boiling in terms of simple geometry parameters and operating liquid conditions is quite difficult art to be handled. Therefore, the available correlations in the open literature are either semi-empirical or they require a large quantity of parameters to be determined prior to the application of such correlations. This of course will exhibit an additional difficulty of handling the enhanced surface effect on the boiling heat transfer performance prediction.

Myers and Katz [16] tried to correlate the experimental data measured boiling different pure liquids on copper and finned tubes. They were successful in producing a correlation for the plain tubes in the form.

$$\frac{\alpha}{k_l} \sqrt{\frac{\sigma}{\rho_l}} = m \left(\frac{k_l \Delta T}{\mu_l h_{fg}} \right)^n \quad (1)$$

Where the constants of the above equation were given according to the boiling liquid considered. In an attempt to apply eq.(1) to the boiling data of the finned tube, the authors [16] found that there were individual curves for each liquid. They were unable to obtain a general correlation for the prediction of the boiling data.

Many investigators correlated their experimental data in the form of:

$$\alpha = C_1 \quad (2)$$

The constants (C_1) and (n) were given for each liquid surface combination. Hahne and Muller [12] presented the following experimental forms for R-11 nucleate boiling on a single low finned tube as:

$$\alpha = 0.697q^{0.79} \quad \text{for } 3 < q < 20 \text{ kW/m}^2 \quad (3.a)$$

$$\alpha = 8.53q^{0.54} \quad \text{for } q > 20 \text{ kW/m}^2 \quad (3.b)$$

Palen and Yang [17] proposed a correlation for the prediction of the boiling heat transfer coefficient on low finned tube in the form:

$$\alpha_{L-F} = F_c F_e \eta \alpha_{pla.} + \alpha_{nc} \quad (4)$$

Where ($\alpha_{pla.}$) is the boiling heat transfer coefficient achieved by a plain tube and (α_{nc}) is the natural convection part of the heating surface which is usually small; of the order of (250) W/m².K for hydrocarbons. The mixture correction factor (F_c), equal to (1.0) for pure fluids and azeotropes and less than (1.0) for mixtures. The fin efficiency (F_e), equal to (1.0) for plain tube and close to unity for finned tube. Palen and Yang represented a formula for the surface factor (η) in the form:

$$\eta = C_1 \left(\frac{q}{q_{ref}} \right)^{m_1} \left(\frac{P}{P_c} \right)^{m_2} F_c^{m_3} \quad (5)$$

The authors [17] postulated that this expression has been found by the (HTRI) organization and did not give numerical values for the exponents and the empirical constant.

Chen et al. [18] proposed a model to predict the boiling heat transfer coefficients of R-11 from copper single and twin finned tube arrangements for the heat flux

range (20) to (50) kW/m². Their correlation involved three empirical constants to be determined for each surface.

Tarrad [13] correlated his own results for boiling on the plain and enhanced surfaces in an expression having the form:

$$q = C_1 \Delta T^n \quad \text{for } 5 \leq q \leq 60 \text{ kW/m}^2 \quad (6)$$

Where the empirical constant (C_1) and the wall superheat index (n) were given for each liquid - surface combination. These values showed a great dependence on the liquid properties and surface structure considered.

3. The Present Correlation:

3.1. Theoretical Background:

The present correlation is based on the Buckingham (π) theorem technique to formulate the independent variables chosen to represent the dependent parameter. It has been proved previously that the enhancement factor produced by an enhanced surface is directly proportional to:

1. The boiling liquid physical properties include the, latent heat of Vaporization, liquid density and thermal conductivity, liquid specific heat and surface tension.
2. The operating conditions of the boiling process including the heat flux and pressure, and
3. The liquid-surface combination factor which includes the effect of the enhancement structure and its interaction with the boiling liquid at the vicinity of the heating surface.

The dependency of the enhancement factor on the working pressure of the boiling process will be introduced through the plain tube prediction of the boiling heat transfer coefficient.

The above highlight points can be expressed by the following mathematical presentation:

$$\eta = \eta(h_{fg}, \rho_l, k_l, cp_l, \sigma, q) \quad (7)$$

Where (η) refers to the enhancement factor defined by:

$$\eta = \frac{\alpha_{enh.}}{\alpha_{pla.}} = \frac{\Delta T_{pla.}}{\Delta T_{enh.}} \quad (8)$$

The enhanced surface nucleate boiling heat transfer coefficient is therefore has the form:

$$\alpha_{enh.} = \eta \alpha_{pla.} \quad (9.a)$$

Or in terms of the wall superheats in the form:

$$\Delta T_{enh.} = \frac{\Delta T_{pla.}}{\eta} \quad (9.b)$$

The plain nucleate pool boiling heat transfer coefficient, $\alpha_{pla.}$, is predicted by the available correlations such as Mostinski [19] equation in the following expression:

$$\alpha_{pla.} = 0.1 p_c^{0.69} q^{0.7} F(p_r) \quad (10.a)$$

Where

$$F(p_r) = 1.8 p_r^{0.17} + 4 p_r^{1.2} + 10 p_r^{10} \quad (10.b)$$

Where (p_c) in bar, (q) in W/m² and ($\alpha_{pla.}$) in W/m² K.

The equation which was proposed by McNelly [20] could also be used for the estimation of the plain nucleate pool boiling heat transfer coefficient in the form:

$$\frac{\alpha_{pla.} d}{k_l} = 0.225 \left(\frac{q d}{h_{fg} \mu_l} \right)^{0.69} \left(\frac{\mu_l c p_l}{k_l} \right)^{0.69} \left(\frac{p d}{\sigma} \right)^{0.31} \left(\frac{\rho_l}{\rho_v} - 1 \right)^{0.33} \quad (11)$$

4. Correlation Formulation:

In performing a dimensionless groups from the independent variables, the four dimensions will be considered for these variables (M, L, T, θ) together with four selected repeating variables (h_{fg}, ρ_l, k_l and cp_l). There are seven variables, $h_{fg}, \rho_l, k_l, cp_l, q, \sigma$ and η , expressed in terms of four fundamental dimensions. Therefore, the equation relating the variables will contain three independent dimensionless groups including the enhancement factor in the forms:

$$\pi_1 = \eta \quad (12.a)$$

$$\pi_2 = \frac{\rho_l h_{fg}^{3/2}}{q} \quad (12.b)$$

and

$$\pi_3 = \left(\frac{\sigma}{k_l} \right) \frac{cp_l}{h_{fg}^{0.5}} \quad (12.c)$$

Therefore, the suggested correlation has the following expression:

$$\pi_1 = \phi(\pi_2, \pi_3) \quad (13.a)$$

$$\eta = \phi \left\{ \left(\frac{\rho_l h_{fg}^{3/2}}{q} \right), \left(\frac{cp_l \sigma}{k_l h_{fg}^{0.5}} \right) \right\} \quad (13.b)$$

This function may be represented in an equation with the form:

$$\eta = C_{S,F} \left(\frac{\rho_l h_{fg}^{3/2}}{q} \right)^m \left(\frac{cp_l \sigma}{k_l h_{fg}^{0.5}} \right)^n \quad (13.c)$$

The liquid-surface combination factor, ($C_{S,F}$), and the exponents of the groups, (m) and (n), should be determined from experimental data to establish the correlation suggested in the present work at its final form.

The independent groups (π_2) and (π_3) are reflecting the effect of the enhancement structure on the ability of bubble nucleation activity and departure parameters, the bubble size and frequency. The first group, (π_2), represents the rate of vaporization of the boiling liquid at the vicinity of the heating element. In fact it represents the intensity of bubble generation in the liquid layer penetrating through the tunnels of the surface structure. The second group, (π_3), corresponds to the effect of the surface tension force during the bubble detachment for the heating surface and the force implemented by the vapor generation and its movement in the structure tunnels at the heating surface.

The experimental data bank presented by Tarrad [13], the data of Marto and Hernandez [11] and the experimental results of Hahne and Muller [12] will be used for verification of the present correlation. A total number of about (520) data points were used in the present correlation for the heat flux range between (10) and (50) kW/m² at atmospheric pressure. Table (1) shows the

structure characteristics of the plain and enhanced surfaces used in the developing of the present correlation.

Table 1. The Structure Characteristics of the Surfaces Used in the Present Correlation.

Surface Type	Reference	Fins/ inch	Enhancement Thick. (mm)	d_o/d_i (mm)
Plain	Tarrad [13]	-----	-----	19/19
Low Finned	Tarrad [13]	19	1.5	18.8/15.8
	Hahne & Muller [12]	19	1.5	18.9/15.9
Gewa-T	Tarrad [13]	19	1.12	18.9/16.7
	Marto & Hernandez [11]	19	1.12	21.2/19

The thermal physical properties of the pure liquids tested by the present correlation are shown in table (2).

Table 2. The Physical Properties of the Liquids Used in the Present Correlation.

Liquid	ρ_l (kg/m ³)	CP_l (kJ/kgK)	k (W/mK)	h_{fg} (kJ/kg)	$\mu_l \cdot 10^3$ (Pa.s)	σ (N/m)	P (bar)
R-113	1507.42	0.98	0.07	147	0.5015	0.0159	34.15
n-Pentane	610.598	2.376	0.1096	356.3	0.1944	0.012	40.5
Ethanol	736.45	3.0202	0.15147	823.83	0.4376	0.0177	63.8
Water	958.4	4.219	0.681	2257	0.2817	0.0589	221.2
R-11	1479.4	0.8703	0.08898	180.33	0.405	0.018	44.1

These values are deduced from Tarrad [13], Incropera and Dewitt [21] and Sinnott [22]. Equation (13.c) showed a total mean absolute error of (7.5 %) when the exponents (m) and (n) were (0.1806) and (1.7) respectively. The liquid-surface combination factors, ($C_{S,F}$), were (0.389) and (0.48) for the *low finned* and *Gewa-T* surfaces respectively.

The numerical values of (m) and (n) conclude that the enhancement factor shows a decrease as the operating heat flux and liquid surface tension increase. This behavior is perfectly corresponds to the experimental data tested in the present work from the point of view of the effect of the heat flux on the predicted enhancement factor.

5. General Formula:

The final form of the suggested correlation of the present work is obtained by applying the above formula of the enhancement factor correlation, eq. (13.c), to the plain tube prediction equation either eq.(10) or eq.(11). The choice of the plain tube nucleate boiling heat transfer coefficient correlation depends on the accuracy and the limitation of use of the considered equation.

Mostinski [19] correlation has been used for all of the test liquids except that of the ethanol prediction. The selection of McNelly [20] equation was based on the excellent agreement between the experimental data and the predicted values of the plain tube. Therefore, the general

form of the present correlation when incorporated with the Mostinski equation was obtained by combining eq.(10) and eq.(13.c) in the form:

$$\alpha_{enh.} = 0.1 C_{S,F} P_c^{0.69} q^{0.7} F(p_r) \left(\frac{\rho_l h_{fg}^{3/2}}{q} \right)^m \left(\frac{cp_l \sigma}{k_l h_{fg}^{0.5}} \right)^n \quad (14)$$

When McNelly correlation for the plain tube heat transfer coefficient is used, the boiling heat transfer coefficient obtained from the plain surface, eq.(11), replaces that of eq.(10) to obtain:

$$\alpha_{enh.} = C_{S,F} \left(\frac{\rho_l h_{fg}^{3/2}}{q} \right)^m \left(\frac{cp_l \sigma}{k_l h_{fg}^{0.5}} \right)^n \times \alpha_{pla.} \quad (15)$$

6. Results and Discussion:

The present formula was tested against different liquids boiling on the plain, *low finned*, and the *Gewa-T* surfaces at atmospheric pressure. The errors percentage of the predicted enhancement factor, eq.(13.c), and the nucleate boiling heat transfer coefficient, eq.(14) or eq.(15), are defined by the following expressions:

$$(Err\%)_{\eta} = \frac{\eta_{pred.} - \eta_{meas.}}{\eta_{meas.}} \times 100 \quad (16.a)$$

and

$$(Err\%)_{\alpha} = \frac{\alpha_{pred.} - \alpha_{meas.}}{\alpha_{meas.}} \times 100 \quad (16.b)$$

The mean absolute errors of the above expressions are also calculated by the following forms:

$$(Err\%)_{abs.} = \Sigma |Err\%| / N \quad (17)$$

The above parameters were calculated for all of the tested liquids and presented in table (3).

Table 3. The Predicted Enhancement Factor and Boiling Heat Transfer Coefficient Error Percentages.

Surface Type	Liquid	Err% η	Err% $\alpha_{enh.}$	Err% α_m	Err% $\alpha_{m.}$
Low Fin	R-113	2 – 13	-3 – 11	7	5.4
	n-Pentane	-12 – -4	-21 – -11	8	14
	Ethanol	-7 – 0	10 – 20	4	11
	Water	-4 – 21	-1 – 13	7	5
	R-11	-3 – 22	9 – 30	5	12.5
Gewa-T	R-113	-17 – 5	-18 – -5	12	12
	n-Pentane	0 – 32	-4 – 9	7	3.4
	Ethanol	-3 – 38	14 – 33	12	18.6
	Water	-9 – 31	-10 – 21	8	6.7

The correlation showed a quite high accuracy for the enhancement factor of both surfaces. The mean absolute error of the enhancement factor for the *low finned* tube is ranged between (4%) and (8%), whereas, the corresponding values for the *Gewa-T* surface were (8%) and (12%). The total mean absolute errors of the enhancement factor for both tubes were (6%) and (9.8%) for the *low finned* and *Gewa-T* surfaces respectively. The corresponding values of the mean absolute error of the predicted boiling heat transfer coefficients were within (9.6%) and (10.2%) for the *low finned* and *Gewa-T* tubes respectively. It is obvious that with these values of absolute errors, the correlation prediction fall within acceptable limits of the mathematical expectation.

It is worthy to mention here that the high absolute error percentage range of the predicted enhancement factor for ethanol, n-pentane and water boiling on the Gewa-T tube occurred at the low heat fluxes ranged between (10 and 15) kW/m² only. The corresponding values for the rest range of heat flux (20 to 50) kW/m² were (-3 to 21)%, (0 to 9)% and (-9 to 3)% for these liquids respectively. Of course neglecting the effect at low heat fluxes of the above correlation will improve the mean accuracy and reduces the mean absolute error of the present formula.

Figure (2) shows the predicted and measured enhancement factors of the boiling liquids on the *low finned* and *Gewa-T* tube structures at the atmospheric pressure. It is obvious that the predicted values of (η) by the form of eq.(13.c) showed a good agreement with those of the measured values and bounded within the limit of ($\pm 20\%$) for whole number of the data points considered in this work. Noting that the predicted values of (η) for the *low finned* and *Gewa-T* tubes fell in the range ($\pm 15\%$) and ($\pm 20\%$) respectively.

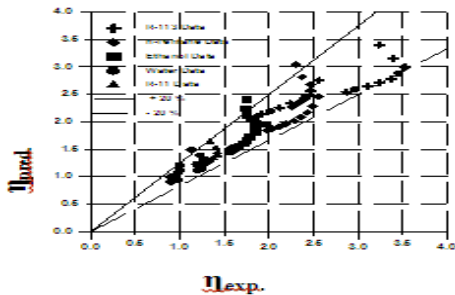


Figure 2. Comparison of the predicted enhancement factor with experimental data of the *low finned* and *Gewa-T* surfaces.

A comparison between the experimental data and the predicted values of (α_{enh}) either by eq.(14) or eq.(15) for the *low finned* and *Gewa-T* surfaces are shown in figures (3) and (4) respectively. The correlation of the present work predicted the boiling heat transfer coefficient for the *low finned* tube within ($\pm 25\%$) for the whole range of the data points considered for this surface. In fact, the predicted values of the boiling heat transfer coefficient fell within an error percentage ranged between (-10%) and as high as (+15%) for more than (98%) of the data points. The corresponding prediction accuracy for the *Gewa-T* surface was within ($\pm 25\%$) for more than (98%) of the boiling data of the heat transfer coefficient. The range of the error percentage of the predicted results with the present correlation revealed a qualitative agreement with the experimental data.

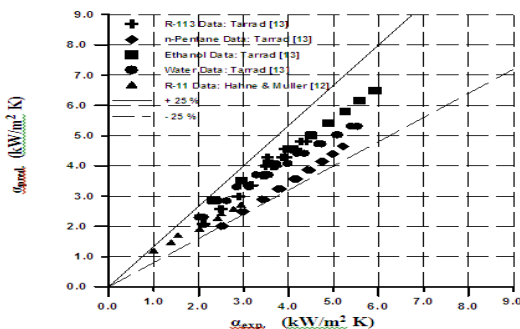


Figure 3. Comparison of the predicted nucleate pool boiling heat transfer coefficient with the experimental data of the *low finned* tube

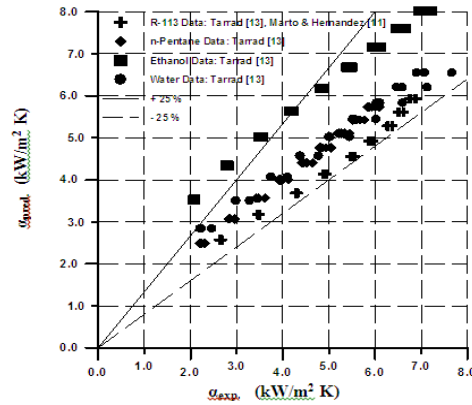


Figure 4. Comparison of the predicted nucleate pool boiling heat transfer coefficient with the experimental data of the *Gewa-T* tube

It is worthwhile to point out that the accuracy and limitation error margin of the present correlation of the nucleate boiling heat transfer coefficient is directly related to the plain tube prediction values. Therefore, it is recommended to select the most appropriate correlation for this object. However, the present work showed that the use of Mostinski equation is acceptable for the majority of the liquids considered in this investigation.

The present correlation for the prediction of the nucleate boiling heat transfer coefficient of the integral machined heating elements showed a good response to the surface and liquid combination type. This concludes that the shape of enhancement has a great interaction effect on the behavior of the bubble nucleation in the machined tunnels where the flow of the boiling liquid is very high there. Further, the boiling liquid properties account for the higher part of the influence on the enhancement expected from a specified surface. For example, the enhancement factor produced by boiling n-pentane on the *low finned* tube was ranged between (2) and (2.6) for the whole range of heat fluxes. The corresponding values of ethanol were (1.6) and (2). Whereas, boiling of water on this surface didn't show any augmentation for the boiling heat transfer coefficient. When boiling R-113 on the *Gewa-T* produces better enhancement than that obtained during boiling on the *low finned* tube. It was ranged between (1.8 to 2.6) and (2.9 to 3.5) for the entire range of the heat flux for the *low finned* and *Gewa-T* respectively. This behavior of the variation was also exhibited by the present formula for the prediction of the enhancement factor and the nucleate boiling heat transfer coefficient of the enhanced surfaces.

7. Conclusions:

General forms of correlations for the enhancement factor and boiling heat transfer coefficient exhibited by the enhanced surfaces were developed in the present investigation.

The formula showed a good response to the variation of both of parameters, (η) and (α_{enh}) when compared with the experimental data during boiling on the integral machined heating surfaces. The suggested equation of the enhanced boiling heat transfer coefficient prediction exhibited an acceptable range of accuracy to be within ($\pm 25\%$) for the *low finned* and *Gewa-T* surface for the heat flux range (10 - 50) kW/m². The total mean absolute error of the

correlation of the enhancement factor is within (7.5%) for the (520) data points used in the present work for both of the enhanced surfaces.

The present form of the correlation for the enhanced boiling heat transfer coefficient prediction can be incorporated with models used for the design of the kettle reboilers and pool boiling evaporators used in a variety of industrial applications. Further correlations are required for other liquid surface combination and enhanced surfaces.

References:

- [1] Jakob, M., Heat Transfer, Wiley, New York, 636-638, 1949.
- [2] C. Courty, A. S. Foust, "Surface Variables in Nucleate Boiling", Chem. Eng. Prog. Symp. Ser., Vol. 51, Pt. 17, 1-12, 1955.
- [3] P. J. Berenson, "Experiments on Pool Boiling Heat Transfer", Int. J. Heat Mass Transfer, Vol. 5, 985-999, 1962.
- [4] H. M. Kurihara, J. E. Myers, "The Effect of Superheat and Surface Roughness on Boiling Coefficients", AIChE. J., Vol. 6, No. 1, 83-91, 1960.
- [5] P. Griffith, J. D. Wallis, "The Role of the Surface Condition in Nucleate Boiling", Chem. Eng. Prog. Symp. Ser., Vol. 56, No. 49, 49-63, 1960.
- [6] C. F. Gottzmann, J. B. Wulf, P. S. O'Neil, "Theory and Application of High Performance Boiling Surface to Components of Absorption Cycle Air Conditioners", Presented at Nat. Gas Res. Tech. Conf., Session V, No. 3, 1-35, Chicago, 1971.
- [7] C. F. Gottzmann, P. S. O'Neil, P. E. Minton, "High Efficiency Heat Exchangers", Chem. Eng. Prog. Vol. 69, No. 7, 69-75, July, 1973.
- [8] Marto P. J., Lepere V. J., Pool Boiling Heat Transfer from Enhanced Surfaces to Dielectric Fluids. In: Webb, R. L., editor. Advances in Enhanced Heat Transfer, ASME. Publ., HTD-Vol. 18, 93-102, 1981.
- [9] Yilmaz, S., Palen, J. W., Taborek, J. Enhanced Boiling Surface as Single Tubes and Bundles. In: Webb, R. L., editor. Advances in Enhanced Heat Transfer, ASME. Publ., HTD-Vol. 18, 123-129, 1981.
- [10] Yilmaz, S., Westwater, J. W., Effect of Commercial Enhanced Surfaces on the Boiling Heat Transfer. In: Webb, R. L., editor. Advances in Enhanced Heat Transfer, ASME. Publ., HTD-Vol. 18, 73-91, 1981.
- [11] P. J. Marto, B. Hernandez, "Nucleate Pool Boiling Characteristics of Gewa-T Surface in Freon-113". AIChE. Symp. Ser., Vol. 79, No. 225, 1-10, 1983.
- [12] E. Hahne, J. Muller, "Boiling on a Finned Tube and Finned Tube Bundle". Int. J. Heat Mass Transfer, Vol. 26, No. 6, 849-859, 1983.
- [13] A., H. Tarrad, "Pool Boiling of Pure Fluids and Mixtures on Plain and Enhanced Surfaces". Ph.D. Thesis, Mech. Eng. Dept., Heriot-Watt University, Edinburgh, U.K., 1991
- [14] S. G. Kandlikar, M. J. Howell, "Investigation of Nucleation and Heat Transfer for Subcooled Flow Boiling on Microfin Surfaces". 2nd European Thermal-Sciences and 14th UIT National Heat Transfer Conference, Vol. 1, 241-247, 1996.
- [15] C. Yuming, G. Manfred, M. Rainer, K. Rudi, "Bubble Dynamics of Boiling of Propane and Iso-butane on Smooth and Enhanced Tubes". Institute of Nuclear Technology and Energy Systems (IKE), University of Stuttgart, Germany, 2003.
- [16] J. E. Myers, D. L. Katz, "Boiling Coefficients Outside Horizontal Tubes". Chem. Eng. Prog. Symp. Ser., Vol. 49, No. 5, 107-114, 1953.
- [17] J. W. Palen, C. C. Yang, "Circulation Boiling Model for Analysis of Kettle and Internal Reboiler Performance". Heat Exchangers for Two Phase Applications, 21st Nat. Heat Transfer Conf. ASME., HTD-Vol. 27, 55-61, Seattle, Wa., 1983.
- [18] Q. Chen, R. Windisch, E. Hahne, "Pool Boiling Heat Transfer on Finned Tubes". Eurotherm Seminar n. 8, Advances in Pool Boiling Heat Transfer, 126-141, Paderborn, Federal Republic of Germany, 1989.
- [19] I. L. Mostinski, "Application of the Rule of Corresponding States for Calculation of Heat Transfer and Critical Heat Flux to Boiling Liquids". British Chemical Engineering Abstracts: FOLIO no. 150, 580, 1963.
- [20] M. J. McNelly, "A Correlation of the Rates of Heat Transfer to Nucleate Boiling Liquids". J. Imperial Coll. Chem. Eng. Soc., Vol. 7, 18-34, 1953.
- [21] Incropera, F. P. and Dewitt, D. P. Introduction to Heat Transfer. 2nd edition, John Wiley Publications, New York, 1990.
- [22] Sinnott, R. K., "Chemical Engineering", Vol. 6, Pergamon Press, New York, 1986.

Fabrication and Analysis of Valve-less Micro-pumps

Shireen Al-Hourani^a, Mohammad N. Hamdan^a, Ahmad A. Al-Qaisia^a, “Moh’d Sami” Ashhab^{*b}

^a Mechanical Engineering Department, University of Jordan, Amman, 11942, Jordan

^b Department of Mechanical Engineering, The Hashemite University, Zarqa, 13115, Jordan

Abstract

Micro-fluidic devices and their applications have received a lot of attention in recent years due to the fast growing progress in the field of Micro-fluid systems. Micropumps are one of the most important micro-fluidic components. In this work, a 2D simulation, using Computerized Fluid Dynamic CFD software, is performed to study the fluid coupling effect driven by piezoelectric actuation of a valveless micropump. The results show the relationship between inlet velocity, actuation value, the flow velocity and pressure inside the valveless micropump using laminar and turbulent models solutions.

© 2011 Jordan Journal of Mechanical and Industrial Engineering. All rights reserved

Keywords: Micro-pumps; Fabrication; Piezoelectric actuation; Simulation.

1. Introduction

The measurements of Microelectromechanical systems (MEMS), such as piezoresistivity coefficients in germanium and silicon were published as early as 1954 which pointed the way for future pressure, displacement, and strain sensors design. The famous talk and respective publishing by Feynman (1960) revealed the possibilities of nanotechnology and micromechanical systems. The fabrication of resonant gate transistors, accelerometers [1], pressure sensors and silicon based strain sensors took place from 1960 to 1970, and these prototypes are generally considered as the beginning of MEMS device fabrication. Petersen (1982) was the first to publish the term micromachining, and also a survey of the respective current major techniques, with potential to be applied to mechanical systems. Intensive laboratory explorations took place during the next decades, followed by industrial success cases which became well known, like inkjet printer head [2], strain-based pressure sensors, mechanical resonators, accelerometers, gyroscope automotive sensors and others [1].

MEMS devices may include in the same structure the electronic and mechanical modules, encompassing sensors and actuators, with dimensions from the order of micrometers to millimeters. Today, they constitute one of the more promising and fast-growing new technologies. In a broad sense, miniaturization results in several new applications, beyond the reach of regular macro scale equipment. A good example is the development of solid state accelerometer used in the new automobile brake systems and air-bags [1,3], an application only made

possible by the large scale production associated to microfabrication techniques [4-6].

MEMS, beginning as an application of microelectronic techniques to build mechanical systems, were first made in silicon. Nowadays, new materials and methods have been tested, looking for good electrical and mechanical properties and low costs. The common methods for MEMS manufacturing are based on micromachining and different kinds of lithography, including the very successful LIGA [7]. Micromachining has been largely used in industrial sensor production since the early 1980's. It is based on different etching techniques used to shape forms on a crystal substrate [8]. LIGA involves the use of X-ray radiation to transfer a pattern to a polymeric thick layer and build metallic molds using some deposition technique. Using the metal structure built, plastic copies may be generated using several techniques [9]. Despite being very efficient, and a great improvement at the time it was developed, the main disadvantage of LIGA is yet a high cost due to mold manufacturing.

Recent progress in MEMS technology provides micro-fluid systems manufacturing and application pluralism further. The micro-fluid systems have the advantages of tiny size and easy to carry, also have high accuracy and short response time. They have quite great values, in fields like semiconductor, electronics, machinery, chemical analysis or biomedicine and laboratory chip development.

Among the micro-fluid control system components, they include micro-channels, micro valves, micro-pumps, micro-sensors and micro-actuators [9,10]. The micropump is one of the important components in micro fluidic systems since the micro-fluid control system requires a power to transport fluids which can provide considerably

* Corresponding author: sami@hu.edu.jo

precise flow rate. Therefore it becomes more popular in medical applications, such as micrototal analysis systems, Lab-on-a-chips (LOC), and micro dosage systems. Valveless micropumps are widely used due to their simple structure, durability and low maintenance. In recent years, wide varieties of valveless micropumps have been developed [1].

Micropump systems usually include an actuating chamber and a valve. There is always a reciprocating cycle vibration in the actuating chamber and the flow channel; it is due to the volume variation of the chamber via moving membrane. A pressure drop is naturally formed when fluids are flowing. In accordance with its different actuating models, it can be divided into piezoelectric, electrostatic, thermo-mechanical, electromagnetic and shape memory alloy types. In addition, the valve can be divided into check-valve and valve-less types. The main function of the valve is to control the flow in a unique direction. The check-valve type acts as a blocking slice using a cantilever beam in the port. When the micropump is actuated there will be difference between the internal and external pressure of the micropump. The valve blocking slice in the channel turns on or off, making the fluid to flow in one direction without a reversing flow. Since the valve is operated frequently, it is easy to cause the valve material fatigue or disability to return to its original state which affects micropump efficiency and life-span. The valveless micropump is comparatively simple and stale [1].

In this work, Computerized Fluid Dynamic CFD software, is used to study the fluid coupling effect driven by piezoelectric actuation of a valveless micropump. The relationship between inlet velocity, actuation value, the flow velocity and pressure inside the valveless micropump using laminar and turbulent models is to be analyzed.

2. Valveless Micropumps

A particular type of micropumps which has received a lot of attention in recent years is the diaphragm based-valveless one shown schematically in Figure 1 [2]. The vibrating diaphragm constitutes the pumping mechanism, and among the different methods which may be used to actuate this vibration the piezoelectric is the well established one. Also this type of micropump design utilizes the dependence of pressure loss of the flow through the pair of fixed, and geometrically similar diffuser/nozzle elements at chamber inlet and outlet ports, on the direction of the flow through these elements to obtain a one way net flow over a cycle of diaphragm vibration cycle which constitutes the pump mechanism. During the pumping phase, namely, when the diaphragm is deflected in downward direction, the flow from the pumping chamber is the nozzle direction at the inlet port and is in the diffuser direction at the output port. On the other hand during the intake phase of a pumping cycle, namely, when the diaphragm is deflected upward, the flow through the inlet port is in the diffuser direction and the flow through the output port is in the nozzle direction. Because, with diffuser/nozzle elements having same size and shape, the resistance (e.g. pressure loss coefficient) to flow in the nozzle direction is higher than that in the

diffuser direction a net flow from inlet to outlet is obtained over a pumping cycle.

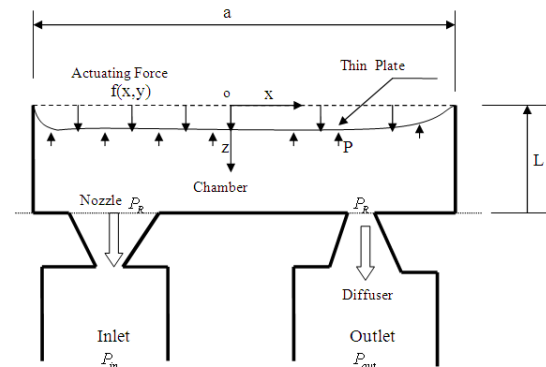


Figure 1. Schematic of the valveless micropump vertical cross section in supply mode.

3. Fabrication

Pump chambers and valves can be etched on silicon wafers using a Reactive Ion Etching (RIE) process to achieve precise control over the final etched shape in the valve regions. The micropumps have anodically bonded Pyrex membranes sealing the pump chamber and valves. All silicon/Pyrex assemblies were mounted on steel or aluminum backing plates, (using Crystalbond 509, Aremco Products, Inc.) [10].

The Reactive Ion Etching consisted of a number of independent components built up around a silicon pump chip. Membranes of stainless steel or brass shim stock could be used. A piezoelectric disk (PZT) can be bonded to the membrane with conductive silver epoxy. Pump bodies should be machined from x mm thick Plexiglas with a y mm diameter hole for the pump chamber, where x and y could be as per the design. Inlet and outlet holes, as needed (depending on the property being tested), should be drilled in the plexiglas. The membrane, pump body, and etched pump chip should be pressed together by an outer assembly. The Plexiglas acted as its own gasket.

4. The Flow Field

In developing fluid flow models for the micropump it is assumed that the density ρ and viscosity η of the modeled fluid are constant, in addition to not being affected by temperature and concentration. The governing equations of continuity and three-dimensional momentum can be expressed as follows:

$$\nabla \cdot \vec{V} = 0 \quad (1)$$

$$\rho \frac{\partial u}{\partial t} + \rho \vec{V} \cdot \nabla u - \eta \nabla^2 u + \frac{\partial p}{\partial x} = F_{E,x} \quad (2)$$

$$\rho \frac{\partial v}{\partial t} + \rho \vec{V} \cdot \nabla v - \eta \nabla^2 v + \frac{\partial p}{\partial y} = F_{E,y} \quad (3)$$

$$\rho \frac{\partial w}{\partial t} + \rho \vec{V} \cdot \nabla w - \eta \nabla^2 w + \frac{\partial p}{\partial z} = F_{E,z} \quad (4)$$

where u , v , w are the velocity components of \vec{V} , η is the dynamic viscosity of the fluid, ρ is the density of the fluid,

and p is pressure. These equations describe the performance of fluids inside the micropump.

5. The Software Simulation

FLUENT, Version: 2d, dp, pbns, lam (2d, double precision, pressure-based, laminar); Release: 6.3.26; was used to analyze the valve less micropump with different actuation conditions and different inlet flow rate. The water was used as the main fluid to simulate the performance of the pump.

By making the inlet initial value to zero, the pressure and velocity contours as solved by FLUENT using equations [1-4] are shown in Figures [2-5].

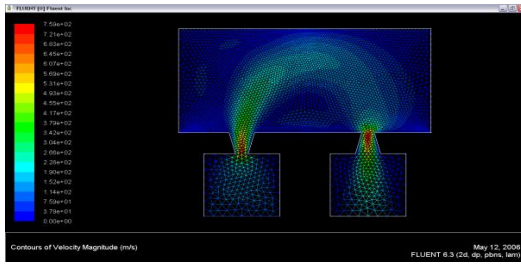


Figure 2. the velocity contour for v_{in} and actuation of 1000m/s, laminar.

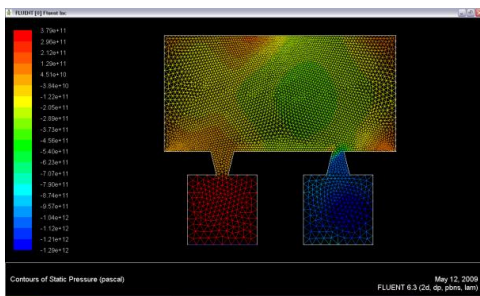


Figure 3. the Pressure contour for v_{in} and actuation of 1000m/s, laminar.

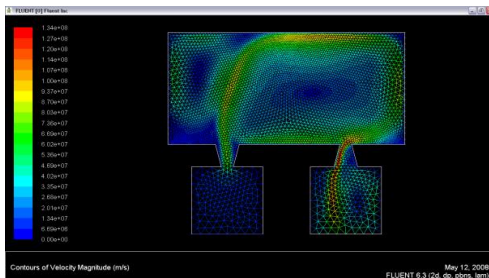


Figure 4. the velocity contour for v_{in} and actuation of 100 Km/s, laminar.

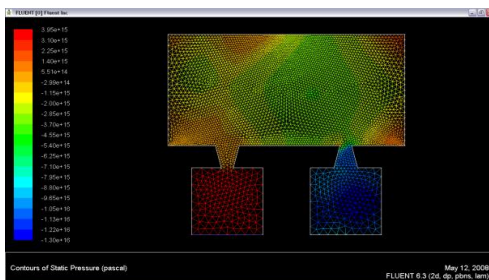


Figure 5. the pressure contour for v_{in} and actuation of 100 Km/s, laminar.

Solving for turbulent flow (K- ϵ model in FLUENT) gives the results shown in figures[6–11].

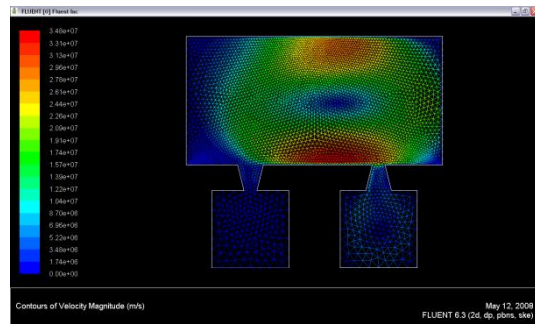


Figure 6. the velocity contour for v_{in} and actuation of 1000m/s, K- ϵ turbulent model.

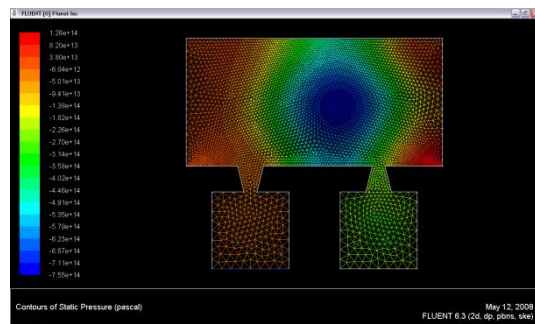


Figure 7. the pressure contour for v_{in} and actuation of 1000m/s, K- ϵ turbulent model.

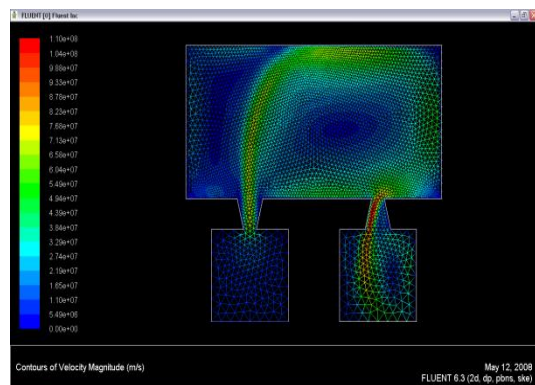


Figure 8. the velocity contour for v_{in} and actuation of 100Km/s, K- ϵ turbulent model.

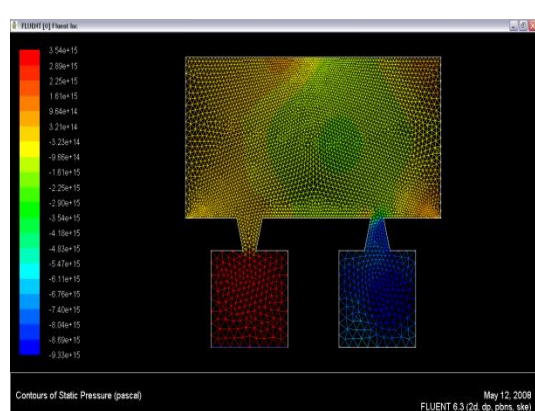


Figure 9. the pressure contour for v_{in} and actuation of 100Km/s, K- ϵ turbulent model.

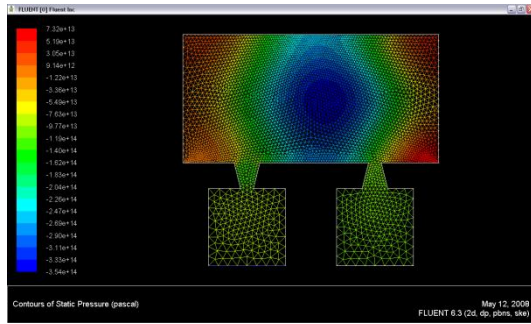


Figure 10. the pressure contour for $v_{in} = 0$ and actuation= 100Km/s, K- ϵ turbulent model.

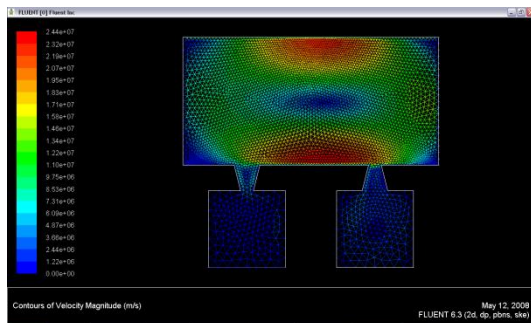


Figure 11. the velocity contour for $v_{in} = 0$ and actuation= 100Km/s, K- ϵ turbulent model.

Figures(2-11) show the velocity and pressure contour with different boundary condition and we can easily notice the net flow from the nozzle to the diffuser, and how the membrane and inlet flow

affected the value of the flow velocity and pressure inside the pump chamber.

6. Conclusion

A 2D simulation was performed to study the fluid coupling of the micropump actuated by piezoelectric plate with variant working conditions. The results show the relationship between inlet velocity, actuation value, the flow velocity and pressure inside the valveless micropump using laminar and turbulent models solutions.

The study shows that the results are highly dependent on the boundary conditions.

References

- [1] E. Nóbrega, C. Campos, "Deep UV lithography valveless micropump design and test". ABCM Symposium Series in Mechatronics, Vol. 3, 2008, 586 - 594.
- [2] P. Glynn-Jones, M. Coletti, N. M. White, C. Bramanti, S. Gabriel, "A Feasibility study on using inkjet technology, micropumps, and MEMS as fuel injectors for bipropellant rocket engines". Acta Astronautica, Vol. 67, 2010, 194 – 203.
- [3] K. Junwu, Y. Zhigang, P. Taijiang, C. Guangming, W. Boda, "Design and test of a high-performance piezoelectric micropump for drug delivery" Sensors and Actuators A, Vol. 121, 2005, 156–161.
- [4] A. Fadl, Z. Zhang, M. Faghri, D. Meyer, E. Simmon, "Experimental Investigation of Geometric Effect on Micro Fluidic Diodicity". Proceedings of the Fifth International Conference on Nanochannels, Microchannels and Minichannels, 2005.
- [5] N. C. Tsai, W. Huang, C. Chiang, R. Lee, "Fabrication and Analysis of Valve-less Micro Pumps". PIERS Proceedings, 2008.
- [6] A. Keißner, C. Brücker, "Micro-Flow in a bundle of micropillars". 14th Int Symp. on Applications of Laser Techniques to Fluid Mechanics, 2008.
- [7] C. Wang, P. Chang, C. Huang; "Optimization of diffuser valves". Journal of Marine Science and Technology, Vol. 16, 2008, 134-138.
- [8] H. Yang, T. H. Tsai, C. C. Hu, "Portable Valve-less Peristaltic Micropump Design and Fabrication". DTIP of MEMS and MOEMS, 2008.
- [9] W. P. Lan, J. S. Chang, K. C. Wu, Y. C. Shih, "Simulation of valveless micropump and mode analysis". DTIP of MEMS and MOEMS, 2007.
- [10] R. L. Bardell, N. R. Sharma, F. K. Forster, M. A. Afromowitz, R. J. Penney, "Designing High-Performance Micro-Pumps Based On No-Moving-Parts Valves". Microelectromechanical Systems (MEMS), DSC-Vol. 62/HTD-Vol. 354, ASME 1997, 47-53.

Economic Design of Joint \bar{X} and R Control Charts Using Differential Evolution

Rukmini V. Kasarapu*, Vijaya B. Vommi

Department of Mechanical Engineering, Andhra University, Visakhapatnam - 530003, India.

Abstract

Benefits of economic designs can be realized to the full extent only by employing appropriate optimization techniques for minimizing the so called loss-cost functions or the total cost functions. Approximate methods employed to find the best control chart parameters may not be effective in obtaining the intended cost benefits. In the present work, differential evolution (DE), a population based evolutionary optimization technique has been employed to design joint \bar{X} and R control charts. The optimum costs obtained are compared with the earlier designs which are based on conventional optimization techniques. It has been observed that the designs obtained using DE are very effective and in majority of the cases remarkable improvements are obtained in cost reductions.

© 2011 Jordan Journal of Mechanical and Industrial Engineering. All rights reserved

Keywords: Economic Control Chart Design; \bar{X} , R Control Charts; Statistical Process Control; Differential Evolution.

1. Introduction

The simultaneous use of \bar{X} chart to control the process mean and R chart to control the process variability gives good control of the process. The power of joint \bar{X} and R charts is much greater than that of \bar{X} or R chart alone. Therefore, in practice, \bar{X} and R control charts are usually employed together to monitor the processes. The economic design of joint \bar{X} and R control charts involves the determination of economically optimal sample size, sampling interval, and control limit coefficient for each chart, so as to minimize the total expected cost of controlling the process.

The economic design of joint \bar{X} and R charts has been studied by various authors. Saniga [1] developed an expected cost model and performed a sensitivity analysis of the model for a process whose mean and variance are controlled by \bar{X} and R charts. Saniga [2] investigated the effects of the types of process models on the joint economic design of \bar{X} and R charts and suggested that accurate process model selection is an important determinant of the quality of joint \bar{X} and R control chart design. Jones and Case [3] developed an economic model which determines the design of joint \bar{X} and R charts to minimize costs and reported that the joint economic design can result in considerable savings over the traditional design of \bar{X} and R charts. Rahim [4] developed a computer program for the optimal economic design of joint \bar{X} and R charts based on the cost model of Saniga and Montgomery [5]. Chung and Chen [6] presented a simplified algorithm

for the determination of optimal design parameters of joint \bar{X} and R control charts. Costa [7] developed a model for joint economic design of \bar{X} and R control charts, where two assignable causes are allowed to occur independently according to exponential distributions and found that the cost surface is convex to the model considered. Gelinas and Lefrancois [8] proposed a heuristic approach for the economic design of \bar{X} and R control charts. Costa and Rahim [9] developed a cost model to determine the design parameters of joint \bar{X} and R charts by adopting a non-uniform sampling interval scheme. A sensitivity analysis of the model is conducted and the cost savings associated with the use of non-uniform sampling intervals instead of constant sampling intervals are evaluated. Gelinas [10] presented a power approximation model for the joint determination of \bar{X} and R control chart parameters based on three regression equations which are used to estimate the sample size and the control limits for the \bar{X} chart and the R chart and the method's performance is tested using a set of previously studied problems. Use of evolutionary computational algorithms has become the need of the day to solve complicated objective functions in search of global solutions. Chou *et al.* [11] proposed joint economic design of \bar{X} and R charts with variable sampling intervals using genetic algorithm. Minimizing the risk of using the uncertain cost and process parameters in the economic designs of \bar{X} control chart has been dealt by Vommi and Seetala [12,13] employing genetic algorithm as a search tool. The present paper proposes the application of Neoteric Differential Evolution algorithm for the economic

* Corresponding author: : rukminivk@yahoo.in

design of joint \bar{X} and R charts based on the cost model of Saniga and Montgomery [5].

2. Cost Model

The process is assumed to start in a state of statistical control. The measurable quality characteristic of the process is assumed to be normally distributed with mean μ_0 and variance σ_0^2 . The process is subject to a single assignable cause of variation. The time lapse between successive occurrences of the assignable cause is assumed to follow a negative exponential distribution with parameter λ . The occurrence of the assignable cause shifts the process mean from μ_0 to $\mu_1 = \mu_0 + \delta\sigma_0$, where δ is a positive constant. Furthermore, it is assumed that with the change in the process mean, the process variance σ_0^2 changes to σ_1^2 , ($\sigma_1^2 \geq \sigma_0^2$) and also the process is shut down during the search for the assignable cause. The production cycle for the process model then consists of four possible periods: (a) the in-control period, (b) the out-of-control period due to the occurrence of the assignable cause, (c) the search period due to a false alarm, and (d) the search and repair period due to a true alarm. The cost model incorporates the fixed and variable costs of sampling, the cost of searching for the assignable cause when it exists, any adjustment or repair costs and the cost of searching for an assignable cause that does not exist.

Notation used in the formulation of loss-cost function:

- n = sample size
- h = sampling interval
- τ_s = expected search time for false alarm
- K_s = expected search cost for false alarm
- τ_r = expected search and adjustment time for true alarm
- K_r = expected search and adjustment cost for true alarm
- V_0 = profit per hour when the process is in control
- V_1 = profit per hour when the process is out of control
- L = average loss-cost per hour of the process
- b = fixed cost of sampling
- c = variable cost of sampling
- α = probability that the control charts for \bar{X} or R or both indicate a false alarm (Type I error)
- $\alpha_{\bar{X}}$ = probability of Type I error of \bar{X} chart
- $P_{\bar{X}}$ = power of \bar{X} chart
- α_R = probability of Type I error of R chart
- P_R = power of R chart
- $\Phi(x)$ = standard normal cumulative distribution function
- P = probability that the control charts for \bar{X} or R or both indicate a true alarm
- τ = average time within an interval before the assignable cause occurs
- K_1 = control limit coefficient for \bar{X} chart
- K_2 = control limit coefficient for R chart

Saniga and Montgomery [5] presented the expected loss-cost per hour of operation as:

$$L = \frac{\lambda U B_1 + V B_0 + \lambda W + (b + cn)(1 + \lambda B_2)/h}{1 + \lambda B_1 + \tau_s B_0 + \lambda \tau_r} \quad (1)$$

Where

$$U = V_0 - V_1 \quad (2)$$

$$V = K_s + V_0 \tau_s \quad (3)$$

$$W = K_r + V_0 \tau_r \quad (4)$$

$$B_0 = \alpha(1 - \lambda\tau)/h \quad (5)$$

$$\tau = \frac{1 - (1 + \lambda h)e^{-\lambda h}}{\lambda(1 - e^{-\lambda h})}$$

$$\tau = \frac{1}{\lambda} - \frac{h}{e^{\lambda h} - 1} \quad (6)$$

$$B_1 = \frac{h}{P} - \tau \quad (7)$$

Chung and Chen [6] approximated the expression $1/(e^{\lambda h} - 1)$ to $(1/\lambda h) - (1/2)$ and the loss-cost function had been modified to \bar{L} given as under. In order to compare the optimum solutions obtained by Chung and Chen [6] with the solutions obtained in the present work by applying DE technique, the same modified loss cost function \bar{L} has been used.

$$\bar{L} = \frac{\lambda U \left(\frac{1}{P} - \frac{1}{2} \right) h + \lambda [W + (b + cn) \left(\frac{1}{P} - \frac{1}{2} \right) - \frac{V\alpha}{2}] + [V\alpha + (b + cn)]/h}{1 + \lambda \left(\frac{1}{P} - \frac{1}{2} \right) h + \tau_s \left(\frac{\alpha}{h} - \frac{\alpha\lambda}{2} \right) + \lambda \tau_r} \quad (8)$$

Hence, the present objective is to minimize the loss-cost function, \bar{L} with respect to the design parameters n , h , K_1 , and K_2 . However, \bar{L} also depends on α and P , which, in turn, involve the normal probability distribution function and the probability integral of the distribution of the range. The expressions for α and P is presented as follows:

Denoting by $X_{(1)}, X_{(2)}, \dots, X_{(n)}$ a random sample of n observations, arranged in an ascending order of magnitude, drawn from a normal population having mean μ_0 and variance σ_0^2 , the sample range R can be written as $X_{(n)} - X_{(1)}$.

The cumulative distribution function for the standardized range, $W_0 = R/\sigma_0$ can be expressed as

$$F_n(W_0) = \left(\int_{-W_0/2}^{W_0/2} \phi(x) dx \right)^n + 2n \int_{W_0/2}^{\infty} \Phi(w) \left(\int_{w-W_0}^w \phi(x) dx \right)^{n-1} dw \quad (9)$$

where

$$\phi(x) = (2\pi)^{-1/2} e^{-x^2/2} \quad (10)$$

The upper and lower control limits respectively for the \bar{X} chart are

$$UCL_{\bar{X}} = \mu_0 + K_1 \sigma_0 / \sqrt{n} \quad (11)$$

and

$$LCL_{\bar{X}} = \mu_0 - K_1 \sigma_0 / \sqrt{n} \quad (12)$$

where $K_1 \geq 0, \sigma_0 \geq 0$.

Also, the upper and lower control limits respectively for the R chart are

$$UCL_R = K_2 \sigma_0 \quad (13)$$

And

$$LCL_R = 0 \quad (14)$$

where $K_2 \geq 0$.

The expressions for the joint probability of false alarm (Type I error) and the joint probability of true alarm (power) for \bar{X} and R charts are as follows:

$$\alpha_{\bar{X}} = 2[1 - \Phi(K_1)] \tag{15}$$

and

$$P_{\bar{X}} = \Phi\left(\frac{\delta\sqrt{n}\sigma_0}{\sigma_1} - K_1\sigma_0/\sigma_1\right) + \Phi\left(-\frac{\delta\sqrt{n}\sigma_0}{\sigma_1} - K_1\sigma_0/\sigma_1\right) \tag{16}$$

where $\sigma_1 \geq \sigma_0$.

$$\alpha_R = P(W_0 \geq K_2) = 1 - F_n(K_2) \tag{17}$$

and

$$P_R = 1 - F_n(K_2\sigma_0/\sigma_1). \tag{18}$$

Thus, the joint probability of false alarm for the \bar{X} and R charts is

$$\alpha = \alpha_{\bar{X}} + \alpha_R - \alpha_{\bar{X}} \cdot \alpha_R. \tag{19}$$

Similarly, the joint probability of true alarm for the \bar{X} and R charts is

$$P = P_{\bar{X}} + P_R - P_{\bar{X}} \cdot P_R. \tag{20}$$

3. . Application of Differential Evolution to Joint Economic Design of \bar{X} and R Charts

Differential Evolution is a population-based, direct-search algorithm for globally optimizing the complicated objective functions. For the present joint economic design, Neoteric Differential Evolution algorithm suggested by Feoktistov [14] has been used. Storn and Price [15] first proposed classical Differential Evolution algorithm which forms the base for the present Neoteric Differential Evolution.

In Differential Evolution, the individuals of population contain design parameters and represent potential optimal solutions. The population is initialized by randomly generating individuals within the lower and higher boundary limits of the design parameters. Each individual of the initial population is evaluated by the cost function. In order to obtain next generation from the initial population, any one individual is chosen as the current best individual. Then, the initial population is subjected to repeated generations of differentiation, crossover and selection. Differentiation and crossover operations are used to create one trial or child individual for each target or parent individual. In order to perform the differentiation, a set of individuals, mutually different and also different from the current target individual, are randomly chosen from the current population. The search strategies of differentiation are designed on the basis of these individuals. In the crossover, by recombining the trial and target individuals, the trial individual inherits parameters of the target individual with certain probability. Next, boundary limits of the trial individual parameters are verified. If any parameter exceeds the limits, the parameter is reset by re-initialization. This trial individual is evaluated by the cost function. Afterwards, selection is fulfilled by comparing the cost function values of target and trial individuals. If the trial individual has an equal or lower cost to the target individual, it replaces its target individual in the population. If the trial individual has higher cost than the target one then the target individual is retained. Then, if the new trial individual of the population is better than the current best individual, the current best individual's index is updated. Figure 1 shows how the

differential evolution is applied for joint economic design of \bar{X} and R control charts.

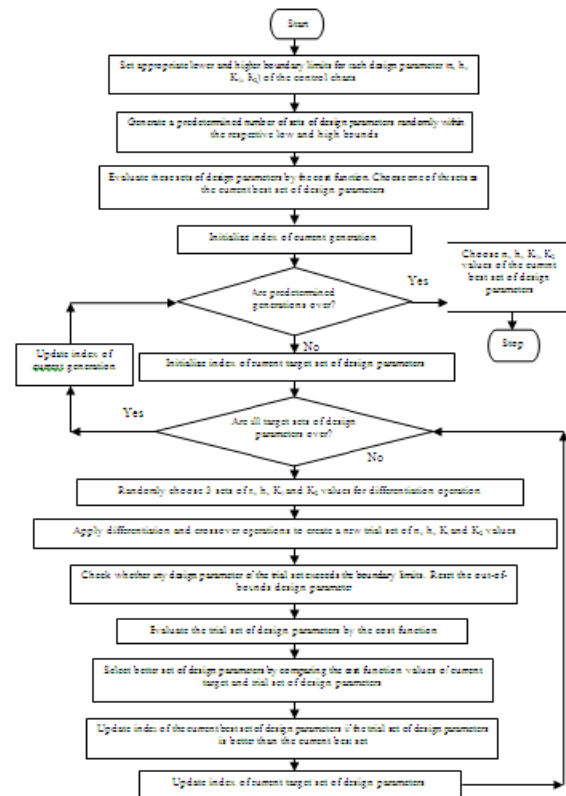


Figure 1. Procedure for Economic Design of Joint \bar{X} and R Control Charts Using Differential Evolution

In the present work, an individual of the population represents a set of design parameters of joint \bar{X} and R control charts, namely n, h, K_1 , and K_2 . To define the limits of search space, feasible values are taken as lower and higher boundary limits of design parameters by considering the published economic designs on joint \bar{X} and R control charts. Table 1 contains the boundary constraints taken on the parameters of the control charts.

Table 1: Boundary constraints of \bar{X} and R charts parameters used in present Differential Evolution algorithm

\bar{X} and R Charts Parameters	Low – High Boundary Limits
n	2 – 33
h	0.25 – 12.00
K_1	1.00 – 6.00
K_2	1.00 – 6.00

Once the search space has been defined, the next step is to find the best parameters of the evolutionary algorithm. Parametric tuning has been carried out to find the effective control parameters for the algorithm namely population size, constant of differentiation, and constant of crossover. A few loss-cost function evaluations have been made using different combinations of control parameters, generations and search strategies. Different population sizes in multiples of 10, number of generations in multiples of 50 and search strategies of differentiation as suggested in Feoktistov [14] have been tested. For refining the selection of constant of differentiation (F) and constant of crossover (Cr), different values in multiples of 0.05 have been

chosen in the intervals [0,1] for F and [0,1] for Cr. By using the feedback provided by these function evaluations and following the practical guidelines given in Feoktistov [14], the parameters for the differential evolution algorithm have been finalized. Table2 shows the parameters of DE employed in the present work to obtain the optimum control chart design parameters.

Table 2: Parameters used in present Differential Evolution algorithm.

Description of the Differential Evolution algorithm parameters	Magnitude/ method
No. of design parameters in a set	4
Population size	80
Search strategy	Rand3
Constant of Differentiation, F	0.85
Type of Crossover	Combinatorial
Constant of Crossover, Cr	0.50
Selection scheme	Elitist
Number of generations	300

As the performance of any evolutionary algorithm is best represented by the probability distribution of the best objective value (Kuo *et al.* [16]), it is required to run algorithm for a number of times, in order to check its consistency in providing the best solution. While obtaining robust \bar{X} chart designs using genetic algorithm, Vommi and Seetala [13] has run the algorithm for 300 times and obtained the statistics of the best objective values. In the present case, to check the consistency of the algorithm in providing the best solutions, the algorithm has been run for 300 times for 40 sets of randomly selected cost and process parameters. All the 300 runs yielded the same best design parameters as reported in the present paper for each of the selected cost and process parameters sets. Since there is no variation in the best values of the objective function, single solution corresponding to each input data set for \bar{X} and R control charts has been tabulated. The joint economic designs of Chung and Chen [6] are considered for comparison of optimum designs obtained by the present algorithm for the same cost and process parameters. A comparison of the results is presented in table 3.

Table 3.Comparison of Results

Cost and process parameters Chung and Chen's results Differential Evolution results % of Reduction in Loss-cost

Ex. No. ^c	δ	λ	V_0	V_1	K_c	K_p	τ_r	τ_s	b	c	σ_0	σ_1	n	h	K_1	K_2	\bar{L}	n	h	K_1	K_2	\bar{L}	
1.	0.50	0.01	50	25	2	1	0.3	0.1	0.5	0.1	0.02	0.03	10	3.46	2.07	4.14	1.4869	10	3.4682	2.0792	4.15	1.4781	0.5918
2.	0.50	0.05	50	25	2	1	0.4	0.1	0.5	0.1	0.02	0.03	10	1.66	2.04	4.09	3.8380	10	1.6720	2.0428	4.10	3.8134	0.6410
3.	0.50	0.01	50	25	15	5	0.3	0.1	0.5	0.2	0.02	0.03	8	4.04	2.05	3.96	1.9794	8	4.0837	2.0605	3.95	1.9691	0.5204
4.	0.50	0.01	50	25	15	5	0.3	0.1	0.5	0.1	0.02	0.03	13	3.71	2.24	4.58	1.7224	13	3.7201	2.2551	4.60	1.7105	0.6909
5.	0.50	0.05	50	25	15	5	0.6	0.1	0.5	0.8	0.02	0.03	2	4.10	0.56	1.00	6.5776	2	3.5593	1.0000	1.00	6.5416	0.5473
6.	0.50	0.05	50	25	15	5	0.5	0.1	0.5	0.4	0.02	0.03	4	2.15	1.70	2.96	5.9003	5	2.4010	1.7160	3.15	5.8771	0.3932
7.	0.50	0.05	50	25	15	5	0.4	0.1	0.5	0.2	0.02	0.03	7	1.88	2.00	3.79	5.1683	8	2.0247	2.0132	3.90	5.1387	0.5727
8.	0.50	0.05	50	25	15	5	0.4	0.1	0.5	0.1	0.02	0.03	12	1.74	2.21	4.48	4.6643	13	1.8238	2.2248	4.55	4.6337	0.6560
9.	0.50	0.01	150	50	2	1	0.4	0.1	0.5	0.4	0.02	0.03	6	2.26	2.01	3.70	5.0149	6	2.2664	2.0140	3.70	5.0004	0.2891
10.	0.50	0.01	150	50	2	1	0.4	0.1	0.5	0.2	0.02	0.03	10	2.08	2.22	4.36	4.3160	10	2.0644	2.2274	4.40	4.2907	0.5862
11.	0.50	0.01	150	50	2	1	0.6	0.1	0.5	0.1	0.02	0.03	16	1.93	2.39	4.93	3.9883	16	1.9385	2.4002	4.95	3.9619	0.6619
12.	0.50	0.05	150	50	2	1	0.6	0.1	0.5	0.4	0.02	0.03	6	1.09	1.97	3.64	13.5670	6	1.0899	1.9688	3.65	13.5256	0.3052
13.	0.50	0.05	150	50	2	1	0.6	0.1	0.5	0.2	0.02	0.03	10	0.99	2.19	4.32	12.1752	10	0.9861	2.1973	4.35	12.1150	0.4944
14.	0.50	0.05	150	50	2	1	0.6	0.1	0.5	0.1	0.02	0.03	15	0.88	2.36	4.86	10.9316	15	0.8891	2.3798	4.85	10.8705	0.5589
15.	0.50	0.01	150	50	15	5	0.6	0.1	0.5	0.4	0.02	0.03	7	2.39	2.10	3.93	5.6217	7	2.3826	2.1022	3.95	5.6011	0.3664
16.	0.50	0.01	150	50	15	5	0.3	0.1	0.5	0.2	0.02	0.03	11	2.14	2.29	4.53	4.4449	11	2.1406	2.3013	4.55	4.4160	0.6502
17.	0.50	0.01	150	50	15	5	0.6	0.1	0.5	0.1	0.02	0.03	17	1.95	2.45	5.06	4.2163	17	1.9467	2.4577	5.10	4.1877	0.6783
18.	0.50	0.05	150	50	15	5	0.6	0.1	0.5	0.4	0.02	0.03	7	1.15	2.06	3.88	14.5951	7	1.1498	2.0636	3.90	14.5395	0.3809
19.	0.50	0.05	150	50	15	5	0.6	0.1	0.5	0.2	0.02	0.03	11	1.02	2.26	4.49	13.0856	11	1.0282	2.2744	4.50	13.0175	0.5204
20.	0.50	0.05	150	50	15	5	0.6	0.1	0.5	0.1	0.02	0.03	17	0.92	2.43	5.04	11.7576	17	0.9268	2.4410	5.05	11.6905	0.5707
21.	0.50	0.01	150	50	2	1	0.6	0.1	5	0.2	0.02	0.03	17	4.29	2.03	4.46	5.9667	17	4.2836	2.0393	4.50	5.9337	0.5531
22.	0.50	0.01	150	50	2	1	0.6	0.1	5	0.1	0.02	0.03	27	4.06	2.21	5.06	5.4536	27	4.0557	2.2132	5.10	5.4268	0.4914
23.	0.50	0.05	150	50	2	1	0.6	0.1	5	0.2	0.02	0.03	16	2.01	1.99	4.35	15.0411	17	2.0395	2.0057	4.45	14.9361	0.6981
24.	0.50	0.05	150	50	2	1	0.4	0.1	5	0.1	0.02	0.03	26	1.89	2.18	4.99	12.7627	26	1.8889	2.1786	5.025	12.6716	0.7138
25.	0.50	0.01	150	50	15	5	0.3	0.1	5	0.2	0.02	0.03	19	4.35	2.12	4.67	5.7943	19	4.3497	2.1236	4.70	5.7587	0.6144
26.	0.50	0.01	150	50	15	5	0.3	0.1	5	0.1	0.02	0.03	30	4.12	2.29	5.24	5.2376	29	4.0814	2.2797	5.25	5.2092	0.5422
27.	0.50	0.05	150	50	15	5	0.4	0.1	5	0.2	0.02	0.03	18	2.04	2.08	4.57	14.6625	18	2.0437	2.0815	4.60	14.5491	0.7734
28.	0.50	0.05	150	50	15	5	0.4	0.1	5	0.1	0.02	0.03	29	1.93	2.26	5.18	13.5381	28	1.9142	2.2500	5.175	13.4431	0.7017
29.	0.50	0.05	150	50	15	5	0.6	0.1	5	0.1	0.02	0.03	28	1.93	2.25	5.14	14.7888	28	1.9277	2.2472	5.175	14.6951	0.6336
30.	1.0	0.01	50	25	2	1	0.3	0.1	0.5	0.4	0.02	0.03	4	4.07	1.62	3.36	1.7241	4	4.0816	1.6157	3.35	1.7212	0.1682
31.	1.0	0.01	50	25	2	1	0.3	0.1	0.5	0.2	0.02	0.03	6	3.55	1.87	4.09	1.4732	6	3.5525	1.8706	4.10	1.4694	0.2579
32.	1.0	0.01	50	25	2	1	0.3	0.1	0.5	0.1	0.02	0.03	9	3.23	2.09	4.73	1.2563	9	3.2484	2.1011	4.70	1.2523	0.3184
33.	1.0	0.05	50	25	2	1	0.6	0.1	0.5	0.8	0.02	0.03	2	2.37	1.06	1.90	5.1965	2	2.5118	0.9910	1.75	5.1747	0.4195
34.	1.0	0.05	50	25	2	1	0.6	0.1	0.5	0.4	0.02	0.03	3	1.78	1.52	2.97	4.7272	4	2.0257	1.5556	3.25	4.7120	0.3215
35.	1.0	0.05	50	25	2	1	0.6	0.1	0.5	0.2	0.02	0.03	6	1.72	1.84	4.03	4.2393	6	1.7376	1.8332	4.00	4.2243	0.3538
36.	1.0	0.05	50	25	2	1	0.6	0.1	0.5	0.1	0.02	0.03	9	1.54	2.07	4.69	3.8083	9	1.5466	2.0643	4.70	3.7942	0.3702
37.	1.0	0.01	50	25	5	5	0.6	0.1	0.5	0.4	0.02	0.03	5	4.29	1.85	3.90	2.1147	5	4.2883	1.8429	3.90	2.0147	4.7288

^c The values of cost and process parameters are same as Chung and Chen[6].

Table 3 (cont.): Comparison of Results
 Cost and process parameters Chung and Chen's results Differential Evolution results % of Reduction in Loss-cost

e.g. No. ^c	δ	λ	V0	V1	Kr	Ks	α	β	b	c	σ_0	σ_1	n	h	K1	K2	L	n	h	K1	K2	L		
38.	1.0	0.01	50	25	5	5	0.3	0.1	0.5	0.2	0.02	0.03	8	3.93	2.08	4.62	1.6806	8	3.9160	2.0784	4.65	1.5787	6.0633	
39.	1.0	0.01	50	25	5	5	0.4	0.1	0.5	0.2	0.02	0.03	7	3.67	2.07	4.49	1.7273	8	3.9200	2.0782	4.65	1.6255	5.8936	
40.	1.0	0.01	50	25	5	5	0.3	0.1	0.5	0.1	0.02	0.03	11	3.44	2.29	5.15	1.4326	11	3.4388	2.2896	5.15	1.3309	7.0990	
41.	1.0	0.05	50	25	5	5	0.5	0.1	0.5	0.8	0.02	0.03	3	2.44	1.50	2.93	6.0073	3	2.4454	1.4787	2.90	5.5483	7.6407	
42.	1.0	0.05	50	25	5	5	0.3	0.1	0.5	0.4	0.02	0.03	5	2.10	1.81	3.84	4.9751	5	2.0810	1.7980	3.85	4.5033	9.4832	
43.	1.0	0.05	50	25	5	5	0.3	0.1	0.5	0.2	0.02	0.03	7	1.77	2.04	4.45	4.3811	7	1.7604	2.0339	4.45	3.9046	10.8763	
44.	1.0	0.05	50	25	5	5	0.3	0.1	0.5	0.1	0.02	0.03	11	1.64	2.27	5.12	3.8778	11	1.6192	2.2627	5.15	3.3960	12.4246	
45.	1.0	0.01	50	25	5	5	0.5	0.1	5	0.2	0.02	0.03	13	8.18	1.92	4.78	2.5157	13	8.1724	1.9169	4.80	2.4053	4.3884	
46.	1.0	0.01	50	25	5	5	0.6	0.1	5	0.1	0.02	0.03	18	7.71	2.15	5.32	2.3725	18	7.6950	2.1447	5.35	2.2639	4.5774	
47.	1.0	0.05	50	25	5	5	0.6	0.1	5	0.2	0.02	0.03	12	4.01	1.85	4.61	6.5125	12	3.9831	1.8372	4.60	6.0100	7.7159	
48.	1.0	0.05	50	25	5	5	0.6	0.1	5	0.1	0.02	0.03	17	3.76	2.08	5.20	6.1509	17	3.7267	2.0771	5.20	5.6514	8.1208	
49.	1.0	0.01	150	50	2	1	0.4	0.1	0.5	0.4	0.02	0.03	6	2.19	2.03	4.32	4.2405	6	2.2043	2.0336	4.30	4.2331	0.1745	
50.	1.0	0.01	150	50	2	1	0.4	0.1	0.5	0.2	0.02	0.03	9	1.98	2.25	4.94	3.5493	9	1.9831	2.2467	4.95	3.5415	0.2198	
51.	1.0	0.01	150	50	2	1	0.4	0.1	0.5	0.1	0.02	0.03	13	1.79	2.46	5.50	2.9911	13	1.7926	2.4605	5.50	2.9840	0.2374	
52.	1.0	0.05	150	50	2	1	0.5	0.1	0.5	0.8	0.02	0.03	4	1.20	1.76	3.57	13.0538	4	1.2062	1.7507	3.55	13.0318	0.1838	
53.	1.0	0.05	150	50	2	1	0.5	0.1	0.5	0.4	0.02	0.03	6	1.03	2.00	4.28	11.4064	6	1.0321	1.9982	4.30	11.3800	0.2314	
54.	1.0	0.05	150	50	2	1	0.5	0.1	0.5	0.2	0.02	0.03	9	0.92	2.22	4.91	9.9825	9	0.9290	2.2250	4.90	9.9567	0.2585	
55.	1.0	0.05	150	50	2	1	0.5	0.1	0.5	0.1	0.02	0.03	12	0.80	2.42	5.40	8.8167	12	0.8034	2.4303	5.35	8.7957	0.2382	
56.	1.0	0.01	150	50	5	5	0.5	0.1	0.5	0.4	0.02	0.03	7	2.36	2.11	4.56	4.6163	7	2.3638	2.1168	4.55	4.5096	2.3114	
57.	1.0	0.01	150	50	5	5	0.5	0.1	0.5	0.2	0.02	0.03	10	2.07	2.33	5.13	3.8869	10	2.0707	2.3257	5.15	3.7807	2.7323	
58.	1.0	0.01	150	50	5	5	0.6	0.1	0.5	0.1	0.02	0.03	13	1.77	2.52	5.38	3.4476	13	1.7720	2.5200	5.60	3.3426	3.0456	
59.	1.0	0.05	150	50	5	5	0.6	0.1	0.5	0.8	0.02	0.03	4	1.17	1.85	3.72	14.6262	4	1.1711	1.8444	3.70	14.1490	3.2626	
60.	1.0	0.05	150	50	5	5	0.5	0.1	0.5	0.4	0.02	0.03	6	1.01	2.08	4.39	12.2456	7	1.1167	2.0905	4.50	11.7527	4.0251	
61.	1.0	0.05	150	50	5	5	0.5	0.1	0.5	0.2	0.02	0.03	9	0.91	2.29	5.01	10.7404	10	0.9765	2.3124	5.05	10.2451	4.6116	
62.	1.0	0.05	150	50	5	5	0.5	0.1	0.5	0.1	0.02	0.03	13	0.82	2.50	5.56	9.5223	13	0.8196	2.5018	5.60	9.0275	5.1962	
63.	1.0	0.01	150	50	2	1	0.6	0.1	5	0.8	0.02	0.03	6	4.57	1.59	3.66	6.5753	6	4.5848	1.5935	3.65	6.5541	0.3224	
64.	1.0	0.01	150	50	2	1	0.6	0.1	5	0.4	0.02	0.03	10	4.31	1.87	4.50	5.8736	10	4.3180	1.8749	4.50	5.8512	0.3814	
65.	1.0	0.01	150	50	2	1	0.6	0.1	5	0.2	0.02	0.03	15	4.06	2.12	5.15	5.3024	15	4.0627	2.1247	5.15	5.2834	0.3583	
66.	1.0	0.01	150	50	2	1	0.3	0.1	5	0.1	0.02	0.03	20	3.79	2.33	5.63	4.4447	20	3.7959	2.3407	5.60	4.4291	0.3510	
67.	1.0	0.05	150	50	2	1	0.6	0.1	5	0.8	0.02	0.03	6	2.19	1.55	3.59	16.2683	6	2.1967	1.5357	3.60	16.1775	0.5581	
68.	1.0	0.05	150	50	2	1	0.3	0.1	5	0.4	0.02	0.03	10	2.02	1.84	4.46	13.0180	10	2.0266	1.8418	4.45	12.9289	0.6844	
69.	1.0	0.05	150	50	2	1	0.3	0.1	5	0.2	0.02	0.03	14	1.86	2.06	5.03	11.8297	14	1.8618	2.0598	5.05	11.7532	0.6467	
70.	1.0	0.05	150	50	2	1	0.3	0.1	5	0.1	0.02	0.03	20	1.76	2.31	5.61	10.9214	20	1.7605	2.3124	5.60	10.8560	0.5988	
71.	1.0	0.01	150	50	5	5	0.4	0.1	5	0.4	0.02	0.03	11	4.38	1.97	4.72	5.8022	11	4.3926	1.9796	4.70	5.8186	2.0751	
72.	1.0	0.01	150	50	5	5	0.4	0.1	5	0.2	0.02	0.03	15	4.03	2.18	5.23	5.1946	15	4.0337	2.1806	5.25	5.0778	2.2485	
73.	1.0	0.01	150	50	5	5	0.5	0.1	5	0.1	0.02	0.03	21	3.82	2.41	5.77	4.8813	21	3.8152	2.4120	5.80	4.7685	2.3109	
74.	1.0	0.05	150	50	5	5	0.6	0.1	5	0.8	0.02	0.03	7	2.25	1.68	3.93	17.1665	7	2.2671	1.6771	3.90	16.6163	3.2051	
75.	1.0	0.05	150	50	5	5	0.5	0.1	5	0.4	0.02	0.03	10	2.03	1.91	4.56	15.0487	11	2.0727	1.9375	4.70	14.5029	3.6269	
76.	1.0	0.05	150	50	5	5	0.5	0.1	5	0.2	0.02	0.03	15	1.90	2.15	5.20	13.8127	15	1.8990	2.1563	5.20	13.2736	3.9029	
77.	1.0	0.05	150	50	5	5	0.5	0.1	5	0.1	0.02	0.03	21	1.79	2.39	5.75	12.8792	21	1.7847	2.3933	5.75	12.3492	4.1152	
78.	1.5	0.01	50	25	2	1	0.6	0.1	0.5	0.4	0.02	0.04	3	3.40	2.06	3.53	1.5699	3	3.3936	2.0511	3.55	1.5691	0.0510	
79.	1.5	0.01	50	25	2	1	0.6	0.1	0.5	0.2	0.02	0.04	4	3.00	2.29	4.06	1.3562	4	3.0059	2.2867	4.05	1.3549	0.0959	
80.	1.5	0.01	50	25	2	1	0.3	0.1	0.5	0.1	0.02	0.04	6	2.84	2.52	4.67	1.0477	6	2.8517	2.5254	4.65	1.0451	0.2482	
81.	1.5	0.05	50	25	2	1	0.6	0.1	0.5	0.4	0.02	0.04	3	1.64	2.02	3.47	4.1584	3	1.6448	2.0124	3.45	4.1501	0.1996	
82.	1.5	0.05	50	25	2	1	0.3	0.1	0.5	0.2	0.02	0.04	4	1.40	2.27	4.03	3.0758	4	1.4116	2.2612	4.00	3.0679	0.2568	
83.	1.5	0.05	50	25	2	1	0.4	0.1	0.5	0.1	0.02	0.04	6	1.33	2.50	4.64	2.9502	6	1.3318	2.4992	4.65	2.9403	0.3356	
84.	1.5	0.01	50	25	5	5	0.4	0.1	0.5	0.4	0.02	0.04	3	3.26	2.25	3.80	1.6657	3	3.2515	2.2437	3.80	1.5686	5.8294	
85.	1.5	0.01	50	25	5	5	0.4	0.1	0.5	0.2	0.02	0.04	5	3.25	2.50	4.51	1.4283	5	3.2506	2.4997	4.50	1.3284	6.9943	
86.	1.5	0.01	50	25	5	5	0.3	0.1	0.5	0.1	0.02	0.04	6	2.79	2.66	4.86	1.2008	7	2.9859	2.7120	5.00	1.1003	8.3694	
87.	1.5	0.05	50	25	5	5	0.6	0.1	0.5	0.4	0.02	0.04	3	1.59	2.22	3.76	4.8826	3	1.5763	2.2095	3.75	4.4210	9.4540	
88.	1.5	0.05	50	25	5	5	0.3	0.1	0.5	0.2	0.02	0.04	5	1.54	2.48	4.48	3.7728	5	1.5236	2.4739	4.50	3.2942	12.6855	
89.	1.5	0.05	50	25	5	5	0.3	0.1	0.5	0.1	0.02	0.04	6	1.32	2.65	4.84	3.3970	6	1.3120	2.6524	4.80	2.9159	14.1625	
90.	1.5	0.05	50	25	2	1	0.6	0.1	5.0	0.1	0.02	0.04	10	3.47	2.34	4.76	5.2434	10	3.4761	2.3351	4.75	5.1922	0.9765	
91.	1.5	0.01	50	25	5	5	0.4	0.1	5.0	0.2	0.02	0.04	8	7.52	2.32	4.59	2.2593	8	7.5071	2.3229	4.60	2.1509	4.7979	
92.	1.5	0.01	50	25	5	5	0.4	0.1	5.0	0.1	0.02	0.04	11	2.55	5.11	7.25	2.1304	11	2.2428	2.5600	5.10	2.0228	5.0507	
93.	1.5	0.05	50	25	5	5	0.5	0.1	5.0	0.4	0.02	0.04	6	3.92	2.08	4.04	6.2683	6	3.9039	2.0686	4.00	5.7667	8.0022	

Table 3 (cont.): Comparison of Results
 Cost and process parameters Chung and Chen's results Differential Evolution results % of Reduction in Loss-cost

e.g. No. ^c	δ	λ	V_0	V_1	K_1	K_2	ξ_0	ξ_1	b	c	σ_0	σ_1	n	h	K_1	K_2	L	n	h	K_1	K_2	L	
101.	1.5	0.05	150	50	2	1	0.3	0.1	0.5	0.1	0.02	0.04	7	0.66	2.82	5.17	6.3645	7	0.6646	2.8250	5.15	6.3498	0.2310
102.	1.5	0.01	150	50	5	5	0.4	0.1	0.5	0.2	0.02	0.04	5	1.54	2.71	4.79	3.0331	6	1.6906	2.7338	5.00	2.9311	3.3629
103.	1.5	0.01	150	50	5	5	0.4	0.1	0.5	0.1	0.02	0.04	7	1.43	2.89	5.26	2.6275	7	1.4485	2.9001	5.20	2.5252	3.8934
104.	1.5	0.05	150	50	5	5	0.6	0.1	0.5	0.4	0.02	0.04	4	0.84	2.50	4.36	11.0358	4	0.8414	2.5011	4.35	10.5584	4.3259
105.	1.5	0.05	150	50	5	5	0.6	0.1	0.5	0.2	0.02	0.04	5	0.72	2.69	4.77	9.9209	5	0.7188	2.6893	4.75	9.4386	4.8615
106.	1.5	0.05	150	50	5	5	0.3	0.1	0.5	0.1	0.02	0.04	7	0.66	2.88	5.25	7.0397	7	0.6622	2.8874	5.20	6.5448	7.0301
107.	1.5	0.01	150	50	2	1	0.5	0.1	0.5	0.4	0.02	0.04	7	3.96	2.33	4.50	5.0818	7	3.9637	2.3312	4.50	5.0642	0.3463
108.	1.5	0.01	150	50	2	1	0.3	0.1	0.5	0.2	0.02	0.04	9	3.71	2.51	4.92	4.3916	9	3.7073	2.5124	4.95	4.3757	0.3621
109.	1.5	0.01	150	50	2	1	0.3	0.1	0.5	0.1	0.02	0.04	12	3.36	2.71	5.38	4.1063	12	3.5687	2.7342	5.35	4.0923	0.3409
110.	1.5	0.05	150	50	2	1	0.5	0.1	0.5	0.4	0.02	0.04	7	1.85	2.30	4.47	12.9502	7	1.8533	2.2923	4.50	12.8793	0.5475
111.	1.5	0.05	150	50	2	1	0.5	0.1	0.5	0.2	0.02	0.04	9	1.73	2.49	4.89	12.1054	9	1.7352	2.4911	4.90	12.0414	0.5287
112.	1.5	0.05	150	50	2	1	0.4	0.1	0.5	0.1	0.02	0.04	12	1.65	2.70	5.35	10.8632	12	1.6557	2.7068	5.35	10.8050	0.5358
113.	1.5	0.01	150	50	5	5	0.6	0.1	0.5	0.4	0.02	0.04	7	3.94	2.39	4.59	5.3874	7	3.9438	2.3889	4.60	5.2726	2.1309
114.	1.5	0.01	150	50	5	5	0.4	0.1	0.5	0.2	0.02	0.04	10	3.77	2.62	5.14	4.6853	10	3.7734	2.6291	5.15	4.5714	2.4310
115.	1.5	0.01	150	50	5	5	0.5	0.1	0.5	0.1	0.02	0.04	12	3.56	2.77	5.44	4.5323	12	3.5641	2.7749	5.45	4.4203	2.4712
116.	1.5	0.05	150	50	5	5	0.6	0.1	0.5	0.8	0.02	0.04	5	1.99	2.13	3.99	15.4402	5	1.9874	2.1226	4.00	14.9111	3.4268
117.	1.5	0.05	150	50	5	5	0.5	0.1	0.5	0.4	0.02	0.04	7	1.85	2.36	4.56	13.6345	7	1.8521	2.3648	4.55	13.1003	3.9180
118.	1.5	0.05	150	50	5	5	0.5	0.1	0.5	0.2	0.02	0.04	9	1.73	2.55	4.97	12.7639	9	1.7348	2.5553	4.95	12.2344	4.1484
119.	1.5	0.05	150	50	5	5	0.6	0.1	0.5	0.1	0.02	0.04	12	1.67	2.75	5.42	12.7929	12	1.6647	2.7485	5.45	12.2699	4.0882
120.	2.0	0.01	50	25	2	1	0.6	0.1	0.5	0.4	0.02	0.04	3	3.48	2.16	3.87	1.4611	3	3.4822	2.1594	3.85	1.4596	0.1027
121.	2.0	0.01	50	25	2	1	0.3	0.1	0.5	0.2	0.02	0.04	4	3.08	2.40	4.41	1.1217	4	3.0800	2.3930	4.40	1.1202	0.1337
122.	2.0	0.01	50	25	2	1	0.3	0.1	0.5	0.1	0.02	0.04	5	2.73	2.39	4.82	0.9735	5	2.7355	2.5876	4.80	0.9720	0.1541
123.	2.0	0.05	50	25	2	1	0.5	0.1	0.5	0.4	0.02	0.04	3	1.65	2.13	3.83	3.7313	3	1.6541	2.1253	3.80	3.7213	0.2680
124.	2.0	0.05	50	25	2	1	0.3	0.1	0.5	0.2	0.02	0.04	4	1.44	2.38	4.38	2.8859	4	1.4410	2.3707	4.35	2.8773	0.2980
125.	2.0	0.05	50	25	2	1	0.3	0.1	0.5	0.1	0.02	0.04	5	1.27	2.57	4.80	2.5722	5	1.2686	2.5659	4.80	2.5647	0.2916
126.	2.0	0.01	50	25	5	5	0.4	0.1	0.5	0.4	0.02	0.04	3	3.38	2.34	4.12	1.5341	3	3.3633	2.3314	4.15	1.4361	6.3881
127.	2.0	0.01	50	25	5	5	0.4	0.1	0.5	0.2	0.02	0.04	4	3.03	2.55	4.62	1.3224	4	3.0261	2.5483	4.60	1.2236	7.4713
128.	2.0	0.01	50	25	5	5	0.5	0.1	0.5	0.1	0.02	0.04	5	2.70	2.73	5.01	1.2140	5	2.6997	2.7276	5.00	1.1147	8.1796
129.	2.0	0.05	50	25	5	5	0.6	0.1	0.5	0.4	0.02	0.04	3	1.63	2.31	4.08	4.6250	3	1.6238	2.3054	4.05	4.1584	10.0886
130.	2.0	0.05	50	25	5	5	0.5	0.1	0.5	0.2	0.02	0.04	4	1.44	2.53	4.59	3.9854	4	1.4287	2.5241	4.60	3.5121	11.8758
131.	2.0	0.05	50	25	5	5	0.5	0.1	0.5	0.1	0.02	0.04	5	1.28	2.71	4.99	3.6644	5	1.2708	2.7127	4.95	3.1881	12.9980
132.	2.0	0.05	50	25	2	1	0.6	0.1	0.5	0.1	0.02	0.04	8	3.40	2.40	4.90	5.1444	8	3.4021	2.3901	4.90	5.0966	0.9292
133.	2.0	0.01	50	25	5	5	0.6	0.1	0.5	0.2	0.02	0.04	7	7.42	2.43	4.84	2.2725	7	7.4081	2.4278	4.85	2.1658	4.6953
134.	2.0	0.01	50	25	5	5	0.3	0.1	0.5	0.1	0.02	0.04	9	7.12	2.65	5.29	2.0284	9	7.1077	2.6478	5.30	1.9220	5.2455
135.	2.0	0.05	50	25	5	5	0.5	0.1	0.5	0.4	0.02	0.04	5	3.78	2.13	4.20	6.0691	5	3.7478	2.1139	4.20	5.5708	8.2104
136.	2.0	0.05	50	25	5	5	0.3	0.1	0.5	0.2	0.02	0.04	7	3.37	2.40	4.81	5.3637	7	3.3394	2.3942	4.80	4.8601	9.3890
137.	2.0	0.05	50	25	5	5	0.3	0.1	0.5	0.1	0.02	0.04	9	2.62	5.26	3.43	5.1463	9	3.3910	2.6201	5.25	4.6440	9.7604
138.	2.0	0.01	150	50	2	1	0.4	0.1	0.5	0.2	0.02	0.04	4	1.46	2.69	4.81	2.6341	4	1.4608	2.6891	4.80	2.6333	0.0304
139.	2.0	0.01	150	50	2	1	0.4	0.1	0.5	0.1	0.02	0.04	6	1.41	2.92	5.38	2.2963	6	1.4170	2.9204	5.35	2.2940	0.1002
140.	2.0	0.05	150	50	2	1	0.5	0.1	0.5	0.4	0.02	0.04	3	0.75	2.48	4.32	9.0347	3	0.7456	2.4684	4.35	9.0296	0.0564
141.	2.0	0.05	150	50	2	1	0.5	0.1	0.5	0.2	0.02	0.04	4	0.67	2.67	4.79	8.0672	4	0.6738	2.6704	4.80	8.0606	0.0818
142.	2.0	0.05	150	50	2	1	0.6	0.1	0.5	0.1	0.02	0.04	6	0.65	2.90	5.36	8.0331	6	0.6538	2.9040	5.35	8.0237	0.1170
143.	2.0	0.01	150	50	5	5	0.6	0.1	0.5	0.2	0.02	0.04	5	1.62	2.81	5.12	3.0774	5	1.6191	2.8042	5.15	2.9773	3.2527
144.	2.0	0.01	150	50	5	5	0.3	0.1	0.5	0.1	0.02	0.04	6	1.41	2.97	5.45	2.2925	6	1.4061	2.9752	5.45	2.1916	4.4013
145.	2.0	0.05	150	50	5	5	0.4	0.1	0.5	0.4	0.02	0.04	3	0.74	2.55	4.42	9.0710	3	0.7403	2.5489	4.35	8.5921	5.2795
145.	2.0	0.05	150	50	5	5	0.4	0.1	0.5	0.4	0.02	0.04	3	0.74	2.55	4.42	9.0710	3	0.7403	2.5489	4.35	8.5921	5.2795
146.	2.0	0.05	150	50	5	5	0.3	0.1	0.5	0.2	0.02	0.04	4	0.66	2.74	4.88	7.3852	5	0.7403	2.7908	5.15	6.8975	6.6037
147.	2.0	0.05	150	50	5	5	0.3	0.1	0.5	0.1	0.02	0.04	6	0.64	2.96	5.44	6.6344	6	0.6426	2.9638	5.45	6.1426	7.4129
148.	2.0	0.01	150	50	5	5	0.6	0.1	0.5	0.4	0.02	0.04	6	3.87	2.41	4.71	4.9841	6	3.8698	2.4122	4.70	4.9709	0.2648
149.	2.0	0.01	150	50	5	5	0.6	0.1	0.5	0.2	0.02	0.04	7	3.60	2.55	5.01	4.6404	7	3.6066	2.5572	5.00	4.6283	0.2608
150.	2.0	0.01	150	50	5	5	0.4	0.1	0.5	0.1	0.02	0.04	9	3.48	2.76	5.44	4.1236	9	3.4763	2.7622	5.45	4.1125	0.2692
151.	2.0	0.05	150	50	5	5	0.5	0.1	0.5	0.4	0.02	0.04	6	1.80	2.39	4.68	12.4604	6	1.8086	2.3864	4.65	12.3993	0.4904
152.	2.0	0.05	150	50	5	5	0.4	0.1	0.5	0.2	0.02	0.04	7	1.67	2.54	4.98	11.0894	7	1.6718	2.5291	5.00	11.0350	0.4906
153.	2.0	0.05	150	50	5	5	0.4	0.1	0.5	0.1	0.02	0.04	9	1.61	2.74	5.41	10.5993	9	1.6106	2.7373	5.45	10.5489	0.4755
154.	2.0	0.01	150	50	5	5	0.6	0.1	0.5	0.4	0.02	0.04	6	3.85	2.47	4.79	5.1348	6	3.8550	2.4703	4.80	5.0243	2.1520
155.	2.0	0.01	150	50	5	5	0.4	0.1	0.5	0.2	0.02	0.04	8	3.67	2.70	5.28	4.4982	8	3.6661	2.6981	5.30	4.3880	2.4499
156.	2.0	0.01	150	50	5	5	0.4	0.1	0.5	0.1	0.02	0.04	10	3.51	2.89								

4. Results and Discussion

Differential Evolution algorithm has been applied in the joint economic design of \bar{X} and R charts by utilizing the cost and process parameters of Saniga and Montgomery [5]. Given the cost and risk factors and other process parameters, the present work finds the sample size, the interval between samples and the control limit coefficient for each chart that minimize the expected loss-cost per hour. A large number of designs (160) have been considered and the solutions obtained are compared with the solutions reported by Chung and Chen [6]. In all the cases, the present algorithm has been found to yield lower loss-costs compared to Chung and Chen's algorithm. A maximum cost reduction of 14% has been obtained which shows the effectiveness of the DE. Also, it has been observed that the algorithm could provide the same best solutions even after a number of times the algorithm was run with different initial solutions.

The optimal sample sizes of the joint economic designs obtained by Chung and Chen [6] are found to range from 2 to 30. Hence, the probability integral for the standardized range values, $F_n(w_0)$, for n between 2 and 30 is required for the joint economic designs. Pearson and Hartley [17]

published the function $F_n(w_0)$ for the values of n between 2 and 20 which can be used for designs involving n values up to 20. Beyond the sample size of 20, $F_n(w_0)$ values are not published, hence are not readily available. Therefore, in the present work a program has been developed to evaluate $F_n(w_0)$. A database for the values of $F_n(w_0)$ has been developed for n between 2 and 33 since it takes lot of time to evaluate the probability integral for different values of n while the DE algorithm is running. The cost function evaluation program is made to use the same database for easy and instant retrieval of the $F_n(w_0)$ values. This saves a lot of time in the cost function evaluations using DE. The values of $F_n(w_0)$ for n between 21 and 33 are presented in table 4 for ready reference.

Finally, it is concluded that the economic designs obtained using Differential evolution, an evolutionary global optimization technique, are much superior in that they provided cost reductions of up to 14% compared to the earlier designs of Chung and Chen [6]. Hence, it is recommended to use evolutionary optimization techniques in the economic design of control charts as it is difficult to obtain closed form solutions by differentiating the loss-cost functions and also the designs are superior to the algorithms used earlier.

Table 4: Probability Integral of the Standardized Range W_0 for Normal Samples (of size n between 21 and 33)

n	21	22	23	24	25	26	27	28	29	30	31	32	33
1.55													
1.60	0.0001												
1.65	0.0001	0.0001											
1.70	0.0002	0.0001	0.0001										
1.75	0.0002	0.0002	0.0001	0.0001									
1.80	0.0004	0.0002	0.0002	0.0001	0.0001								
1.85	0.0005	0.0004	0.0002	0.0002	0.0001	0.0001							
1.90	0.0008	0.0005	0.0004	0.0002	0.0002	0.0001	0.0001						
1.95	0.0012	0.0008	0.0005	0.0004	0.0003	0.0002	0.0001	0.0001	0.0001				
2.00	0.0016	0.0011	0.0008	0.0006	0.0004	0.0003	0.0002	0.0001	0.0001	0.0001			
2.05	0.0023	0.0016	0.0011	0.0008	0.0006	0.0004	0.0003	0.0002	0.0001	0.0001	0.0001	0.0001	
2.10	0.0031	0.0023	0.0016	0.0012	0.0008	0.0006	0.0004	0.0003	0.0002	0.0002	0.0001	0.0001	0.0001
2.15	0.0042	0.0031	0.0023	0.0017	0.0012	0.0009	0.0007	0.0005	0.0003	0.0003	0.0002	0.0001	0.0001
2.20	0.0057	0.0042	0.0031	0.0023	0.0017	0.0013	0.0010	0.0007	0.0005	0.0004	0.0003	0.0002	0.0002
2.25	0.0075	0.0056	0.0043	0.0032	0.0024	0.0018	0.0014	0.0010	0.0008	0.0006	0.0004	0.0003	0.0002
2.30	0.0097	0.0074	0.0057	0.0044	0.0033	0.0025	0.0019	0.0015	0.0011	0.0009	0.0007	0.0005	0.0004
2.35	0.0125	0.0097	0.0075	0.0058	0.0045	0.0035	0.0027	0.0021	0.0016	0.0013	0.0010	0.0007	0.0006
2.40	0.0159	0.0125	0.0098	0.0077	0.0061	0.0048	0.0037	0.0029	0.0023	0.0018	0.0014	0.0011	0.0009
2.45	0.0200	0.0160	0.0127	0.0101	0.0080	0.0064	0.0050	0.0040	0.0032	0.0025	0.0020	0.0016	0.0012
2.50	0.0249	0.0201	0.0162	0.0130	0.0105	0.0084	0.0067	0.0054	0.0043	0.0035	0.0028	0.0022	0.0018
2.55	0.0307	0.0251	0.0204	0.0166	0.0135	0.0110	0.0089	0.0072	0.0059	0.0047	0.0038	0.0031	0.0025
2.60	0.0375	0.0309	0.0254	0.0209	0.0172	0.0141	0.0116	0.0095	0.0078	0.0064	0.0052	0.0043	0.0035
2.65	0.0454	0.0378	0.0314	0.0261	0.0217	0.0180	0.0149	0.0124	0.0102	0.0085	0.0070	0.0058	0.0048
2.70	0.0544	0.0457	0.0384	0.0322	0.0270	0.0226	0.0190	0.0159	0.0133	0.0111	0.0093	0.0077	0.0065
2.75	0.0647	0.0549	0.0465	0.0394	0.0333	0.0282	0.0238	0.0201	0.0170	0.0144	0.0121	0.0102	0.0086
2.80	0.0762	0.0652	0.0558	0.0477	0.0407	0.0348	0.0297	0.0253	0.0215	0.0183	0.0156	0.0133	0.0113
2.85	0.0891	0.0769	0.0664	0.0572	0.0493	0.0424	0.0365	0.0314	0.0270	0.0232	0.0199	0.0171	0.0147
2.90	0.1033	0.0900	0.0782	0.0680	0.0591	0.0513	0.0445	0.0386	0.0334	0.0290	0.0251	0.0217	0.0188
2.95	0.1190	0.1044	0.0915	0.0802	0.0702	0.0614	0.0537	0.0469	0.0410	0.0358	0.0312	0.0272	0.0238
3.00	0.1360	0.1203	0.1062	0.0938	0.0827	0.0729	0.0642	0.0566	0.0498	0.0438	0.0385	0.0338	0.0297
3.05	0.1545	0.1375	0.1223	0.1088	0.0966	0.0858	0.0761	0.0675	0.0599	0.0530	0.0470	0.0416	0.0368
3.10	0.1743	0.1562	0.1399	0.1252	0.1120	0.1001	0.0895	0.0799	0.0713	0.0636	0.0567	0.0506	0.0451
3.15	0.1953	0.1762	0.1589	0.1432	0.1289	0.1160	0.1043	0.0938	0.0842	0.0756	0.0679	0.0609	0.0546
3.20	0.2177	0.1976	0.1792	0.1625	0.1472	0.1333	0.1206	0.1091	0.0986	0.0891	0.0805	0.0727	0.0656
3.25	0.2411	0.2202	0.2009	0.1832	0.1670	0.1521	0.1385	0.1260	0.1146	0.1042	0.0946	0.0860	0.0781
3.30	0.2656	0.2439	0.2238	0.2053	0.1881	0.1723	0.1578	0.1444	0.1320	0.1207	0.1103	0.1008	0.0920
3.35	0.2910	0.2687	0.2479	0.2285	0.2106	0.1939	0.1785	0.1642	0.1510	0.1388	0.1276	0.1172	0.1076
3.40	0.3173	0.2944	0.2730	0.2530	0.2343	0.2169	0.2006	0.1855	0.1715	0.1585	0.1464	0.1351	0.1247
3.45	0.3441	0.3209	0.2990	0.2784	0.2591	0.2410	0.2241	0.2082	0.1934	0.1796	0.1667	0.1546	0.1434
3.50	0.3716	0.3480	0.3257	0.3047	0.2849	0.2662	0.2487	0.2322	0.2167	0.2021	0.1885	0.1757	0.1637
3.55	0.3994	0.3757	0.3532	0.3318	0.3116	0.2925	0.2744	0.2573	0.2412	0.2260	0.2116	0.1982	0.1855
3.60	0.4274	0.4037	0.3811	0.3595	0.3390	0.3195	0.3010	0.2834	0.2668	0.2510	0.2361	0.2220	0.2087
3.65	0.4555	0.4319	0.4093	0.3877	0.3670	0.3473	0.3285	0.3105	0.2934	0.2772	0.2618	0.2471	0.2332
3.70	0.4836	0.4602	0.4378	0.4162	0.3954	0.3756	0.3565	0.3383	0.3209	0.3043	0.2885	0.2734	0.2589

Table 4 (cont.): Probability Integral of the Standardized Range W_0 for Normal Samples (of size n between 21 and 33)

n W_0	21	22	23	24	25	26	27	28	29	30	31	32	33
3.75	0.5115	0.4885	0.4662	0.4448	0.4241	0.4042	0.3851	0.3668	0.3491	0.3323	0.3161	0.3006	0.2858
3.85	0.5662	0.5441	0.5227	0.5019	0.4817	0.4621	0.4431	0.4247	0.4070	0.3899	0.3733	0.3574	0.3420
3.90	0.5927	0.5713	0.5504	0.5300	0.5102	0.4909	0.4722	0.4540	0.4363	0.4192	0.4027	0.3866	0.3712
3.95	0.6186	0.5979	0.5776	0.5578	0.5384	0.5195	0.5011	0.4831	0.4657	0.4487	0.4322	0.4162	0.4007
4.00	0.6438	0.6238	0.6042	0.5850	0.5662	0.5477	0.5297	0.5121	0.4949	0.4782	0.4618	0.4459	0.4305
4.05	0.6681	0.6490	0.6301	0.6116	0.5933	0.5754	0.5579	0.5407	0.5239	0.5074	0.4914	0.4757	0.4604
4.10	0.6915	0.6733	0.6552	0.6374	0.6198	0.6025	0.5855	0.5688	0.5524	0.5364	0.5206	0.5052	0.4901
4.15	0.7140	0.6966	0.6794	0.6623	0.6455	0.6289	0.6125	0.5963	0.5804	0.5648	0.5494	0.5344	0.5196
4.20	0.7355	0.7190	0.7026	0.6864	0.6703	0.6544	0.6386	0.6231	0.6077	0.5926	0.5777	0.5631	0.5487
4.25	0.7559	0.7404	0.7249	0.7094	0.6941	0.6789	0.6639	0.6490	0.6343	0.6197	0.6054	0.5912	0.5772
4.30	0.7753	0.7607	0.7461	0.7315	0.7170	0.7026	0.6882	0.6740	0.6599	0.6460	0.6322	0.6185	0.6051
4.35	0.7937	0.7800	0.7662	0.7525	0.7388	0.7251	0.7115	0.6980	0.6846	0.6713	0.6581	0.6450	0.6321
4.40	0.8110	0.7981	0.7853	0.7724	0.7595	0.7466	0.7338	0.7210	0.7083	0.6956	0.6831	0.6706	0.6582
4.45	0.8272	0.8153	0.8032	0.7912	0.7791	0.7670	0.7550	0.7429	0.7309	0.7189	0.7070	0.6952	0.6834
4.50	0.8424	0.8313	0.8201	0.8089	0.7976	0.7863	0.7750	0.7637	0.7524	0.7411	0.7298	0.7186	0.7075
4.55	0.8566	0.8463	0.8360	0.8255	0.8150	0.8045	0.7939	0.7833	0.7727	0.7621	0.7516	0.7410	0.7304
4.60	0.8698	0.8603	0.8507	0.8411	0.8313	0.8215	0.8117	0.8018	0.7919	0.7820	0.7721	0.7622	0.7523
4.65	0.8820	0.8733	0.8645	0.8556	0.8466	0.8375	0.8284	0.8192	0.8100	0.8007	0.7915	0.7822	0.7729
4.70	0.8934	0.8854	0.8772	0.8690	0.8607	0.8524	0.8439	0.8354	0.8269	0.8183	0.8097	0.8011	0.7924
4.75	0.9038	0.8965	0.8890	0.8815	0.8739	0.8662	0.8584	0.8506	0.8427	0.8347	0.8267	0.8187	0.8107
4.80	0.9134	0.9067	0.8999	0.8930	0.8861	0.8790	0.8718	0.8646	0.8574	0.8500	0.8427	0.8352	0.8278
4.85	0.9222	0.9161	0.9099	0.9037	0.8973	0.8908	0.8843	0.8776	0.8710	0.8642	0.8574	0.8506	0.8437
4.90	0.9302	0.9247	0.9191	0.9134	0.9076	0.9017	0.8957	0.8897	0.8836	0.8774	0.8711	0.8649	0.8585
4.95	0.9376	0.9326	0.9275	0.9223	0.9170	0.9117	0.9062	0.9007	0.8951	0.8895	0.8838	0.8780	0.8722
5.00	0.9443	0.9398	0.9352	0.9305	0.9257	0.9208	0.9159	0.9109	0.9058	0.9007	0.8955	0.8902	0.8849
5.05	0.9503	0.9463	0.9421	0.9379	0.9336	0.9292	0.9247	0.9202	0.9156	0.9109	0.9062	0.9014	0.8965
5.10	0.9558	0.9522	0.9484	0.9446	0.9407	0.9368	0.9327	0.9286	0.9245	0.9202	0.9159	0.9116	0.9072
5.15	0.9608	0.9575	0.9542	0.9507	0.9472	0.9437	0.9400	0.9363	0.9326	0.9288	0.9249	0.9209	0.9170
5.20	0.9652	0.9623	0.9593	0.9563	0.9531	0.9499	0.9467	0.9433	0.9399	0.9365	0.9330	0.9295	0.9259
5.25	0.9693	0.9667	0.9640	0.9612	0.9584	0.9556	0.9526	0.9497	0.9466	0.9435	0.9404	0.9372	0.9339
5.30	0.9729	0.9705	0.9682	0.9657	0.9632	0.9607	0.9580	0.9554	0.9526	0.9499	0.9471	0.9442	0.9413
5.35	0.9761	0.9740	0.9719	0.9697	0.9675	0.9652	0.9629	0.9605	0.9581	0.9556	0.9531	0.9505	0.9479
5.40	0.9790	0.9771	0.9753	0.9733	0.9714	0.9693	0.9673	0.9651	0.9630	0.9608	0.9585	0.9562	0.9539
5.45	0.9815	0.9799	0.9783	0.9766	0.9748	0.9730	0.9712	0.9693	0.9673	0.9654	0.9634	0.9613	0.9593
5.50	0.9838	0.9824	0.9809	0.9794	0.9779	0.9763	0.9746	0.9730	0.9713	0.9695	0.9677	0.9659	0.9641
5.55	0.9858	0.9846	0.9833	0.9820	0.9806	0.9792	0.9777	0.9763	0.9748	0.9732	0.9716	0.9700	0.9684
5.60	0.9876	0.9865	0.9854	0.9842	0.9830	0.9818	0.9805	0.9792	0.9779	0.9765	0.9751	0.9737	0.9722
5.65	0.9892	0.9882	0.9873	0.9862	0.9852	0.9841	0.9830	0.9818	0.9806	0.9794	0.9782	0.9769	0.9757
5.70	0.9906	0.9898	0.9889	0.9880	0.9871	0.9861	0.9851	0.9841	0.9831	0.9820	0.9809	0.9798	0.9787
5.75	0.9918	0.9911	0.9903	0.9896	0.9887	0.9879	0.9870	0.9862	0.9852	0.9843	0.9834	0.9824	0.9814
5.80	0.9929	0.9923	0.9916	0.9909	0.9902	0.9895	0.9887	0.9880	0.9872	0.9863	0.9855	0.9847	0.9838
5.85	0.9939	0.9933	0.9927	0.9921	0.9915	0.9909	0.9902	0.9895	0.9888	0.9881	0.9874	0.9867	0.9859
5.90	0.9947	0.9942	0.9937	0.9932	0.9926	0.9921	0.9915	0.9909	0.9903	0.9897	0.9891	0.9884	0.9878
5.95	0.9954	0.9950	0.9946	0.9941	0.9936	0.9932	0.9927	0.9922	0.9916	0.9911	0.9905	0.9900	0.9894

Table 4 (cont.): Probability Integral of the Standardized Range W_0 for Normal Samples (of size n between 21 and 33)

n W_0	21	22	23	24	25	26	27	28	29	30	31	32	33
6.00	0.9961	0.9957	0.9953	0.9949	0.9945	0.9941	0.9937	0.9932	0.9928	0.9923	0.9918	0.9913	0.9908
6.05	0.9966	0.9963	0.9960	0.9956	0.9953	0.9949	0.9945	0.9942	0.9938	0.9933	0.9929	0.9925	0.9921
6.10	0.9971	0.9968	0.9965	0.9962	0.9959	0.9956	0.9953	0.9950	0.9946	0.9943	0.9939	0.9935	0.9932
6.15	0.9975	0.9973	0.9970	0.9968	0.9965	0.9962	0.9960	0.9957	0.9954	0.9951	0.9948	0.9944	0.9941
6.20	0.9979	0.9977	0.9974	0.9972	0.9970	0.9968	0.9965	0.9963	0.9960	0.9958	0.9955	0.9952	0.9949
6.25	0.9982	0.9980	0.9978	0.9976	0.9974	0.9972	0.9970	0.9968	0.9966	0.9964	0.9961	0.9959	0.9957
6.30	0.9984	0.9983	0.9981	0.9980	0.9978	0.9976	0.9975	0.9973	0.9971	0.9969	0.9967	0.9965	0.9963
6.35	0.9987	0.9985	0.9984	0.9983	0.9981	0.9980	0.9978	0.9977	0.9975	0.9973	0.9972	0.9970	0.9968
6.40	0.9989	0.9988	0.9986	0.9985	0.9984	0.9983	0.9982	0.9980	0.9979	0.9977	0.9976	0.9974	0.9973
6.45	0.9990	0.9989	0.9988	0.9987	0.9986	0.9985	0.9984	0.9983	0.9982	0.9981	0.9979	0.9978	0.9977
6.50	0.9992	0.9991	0.9990	0.9989	0.9988	0.9988	0.9987	0.9986	0.9985	0.9984	0.9983	0.9981	0.9980
6.55	0.9993	0.9992	0.9992	0.9991	0.9990	0.9989	0.9989	0.9988	0.9987	0.9986	0.9985	0.9984	0.9983
6.60	0.9994	0.9994	0.9993	0.9992	0.9992	0.9991	0.9990	0.9990	0.9989	0.9988	0.9987	0.9987	0.9986
6.65	0.9995	0.9995	0.9994	0.9994	0.9993	0.9992	0.9992	0.9991	0.9991	0.9990	0.9989	0.9989	0.9988
6.70	0.9996	0.9995	0.9995	0.9995	0.9994	0.9994	0.9993	0.9993	0.9992	0.9992	0.9991	0.9990	0.9990
6.75	0.9996	0.9996	0.9996	0.9995	0.9995	0.9995	0.9994	0.9994	0.9993	0.9993	0.9992	0.9992	0.9991
6.80	0.9997	0.9997	0.9996	0.9996	0.9996	0.9995	0.9995	0.9995	0.9994	0.9994	0.9994	0.9993	0.9993
6.85	0.9998	0.9997	0.9997	0.9997	0.9996	0.9996	0.9996	0.9996	0.9995	0.9995	0.9995	0.9994	0.9994
6.90	0.9998	0.9998	0.9997	0.9997	0.9997	0.9997	0.9997	0.9996	0.9996	0.9996	0.9995	0.9995	0.9995
6.95	0.9998	0.9998	0.9998	0.9998	0.9998	0.9997	0.9997	0.9997	0.9997	0.9996	0.9996	0.9996	0.9996
7.00	0.9999	0.9998	0.9998	0.9998	0.9998	0.9998	0.9998	0.9997	0.9997	0.9997	0.9997	0.9997	0.9996
7.05	0.9999	0.9999	0.9999	0.9998	0.9998	0.9998	0.9998	0.9998	0.9998	0.9998	0.9997	0.9997	0.9997
7.10	0.9999	0.9999	0.9999	0.9999	0.9999	0.9998	0.9998	0.9998	0.9998	0.9998	0.9998	0.9998	0.9997
7.15	0.9999	0.9999	0.9999	0.9999	0.9999	0.9999	0.9999	0.9998	0.9998	0.9998	0.9998	0.9998	0.9998
7.20	0.9999	0.9999	0.9999	0.9999	0.9999	0.9999	0.9999	0.9999	0.9999	0.9999	0.9998	0.9998	0.9998
7.25	0.9999	0.9999	0.9999	0.9999	0.9999	0.9999	0.9999	0.9999	0.9999	0.9999	0.9999	0.9999	0.9999

References

- [1] E. M. Saniga, "Joint economically optimal design of \bar{X} and R control charts". Management Science, Vol. 24, 1977, 420-431.
- [2] E. M. Saniga, "Joint economic design of \bar{X} and R control charts with alternate process models". AIIE Transactions, Vol. 11, 1979, 254-260.
- [3] L. J. Jones, K. E. Case, "Economic design of a joint \bar{X} and R control chart". AIIE Transactions, Vol. 13, 1981, 182-195.
- [4] M. A. Rahim, "Determination of optimal design parameters of joint \bar{X} and R charts". Journal of Quality Technology, Vol. 21, 1989, 65-70.
- [5] E. M. Saniga, D. C. Montgomery, "Economical quality control policies for a single cause system". AIIE Transactions, Vol. 13, 1981, 258-264.
- [6] K. J. Chung, S. L. Chen, "An algorithm for the determination of optimal design parameters of joint \bar{X} and R control charts". Computers & Industrial Engineering, Vol. 24, 1993, 291-301.
- [7] F. B. Costa, "Joint economic design of \bar{X} and R control charts for processes subject to two independent assignable causes". IIE Transactions, Vol. 25, 1993, 27-33.
- [8] R. Gelinas, P. Lefrancois, "A heuristic approach for the economic design of \bar{X} and R control charts". International Journal of Quality & Reliability Management, Vol. 15, 1998, 443-455.
- [9] A. F. B. Costa, M. A. Rahim, "Economic design of \bar{X} and R charts under weibull shock models". Quality and Reliability Engineering International, Vol. 16, 2000, 143-156.
- [10] R. Gelinas, "A power approximation model for the joint determination of X and R control chart parameters". International Journal of Quality & Reliability Management, Vol. 18, 2001, 625-643.
- [11] Y. Chou, C. C. Wu, C. H. Chen, "Joint economic design of variable sampling intervals \bar{X} and R charts using genetic algorithms". Communications in Statistics-Simulation and Computation, Vol. 35, 2006, 1027-1043.
- [12] V. B. Vommi, S. N. Murty Seetala, "A new approach to robust economic design of control charts". Applied Soft Computing, Vol. 7, 2007, 211-228.

- [13] V. B. Vomma, S. N. Murty Seetala, "A simple approach for robust economic design of control charts". Computers and Operations Research, Vol. 34, 2007, 2001-2009.
- [14] Vitaliy Feoktistov. Differential evolution in search of solutions. USA: Springer Publications; 2006.
- [15] R. Storn, K. Price, "Differential evolution – a simple and efficient adaptive scheme for global optimization over continuous spaces". Technical Report TR-95-012, International Computer Science Institute, Berkeley, CA, 1995.
- [16] W. Kuo, V. R. Prasad, F. A. Tillman, C. L. Hwang. Optimal reliability design. Cambridge: Cambridge University Press; 2001.
- [17] E. S. Pearson, H. O. Hartley, "The probability integral of the range in samples of n observations from a normal population". Biometrika, Vol. 32, 1942, 301-310.

Main Factors Causing Workers Turnover in Jordan Industrial Sector

Wisam M. Abu Jadayil *

Department of Industrial Engineering, The Hashemite University, Zarqa, Jordan 13135

Abstract

Workers turnover has been studied in Jordan to find out the main reasons causing this problem. A questionnaire was designed and distributed over twenty eight factories in Jordan, seven factories in each of the three main industrial cities there, and seven factories outside these industrial cities. Five main categories for workers turnover were studied and investigated. The salary, the working environment, the helpfulness and corporation of the management, the worker psychological state and relationships with surrounding environment, and the services provided by the employer to the employee. Analysis of the results showed that the main reason for turnover in industrial cities is the salary. which affects workers in industrial cities located closer to big cities more. One the other hand workers in factories located outside industrial cities suffer mainly from working conditions and environment, which force them to leave. These two reasons are the main issues of workers in industrial sector in Jordan as just an example of Middle Eastern countries.

© 2011 Jordan Journal of Mechanical and Industrial Engineering. All rights reserved

Keywords: Workers turnover, Jordanian industrial sector, Salary, Working conditions.

1. Introduction

Understanding workers flow is the fundamental aspect for understanding the market and how successful the economy of the country is. Although it is known that workers flow is very large in Jordan, the basic reasons which cause this workers turnover is not well realized yet. No comprehensive studies in the literature have been made until now, neither in Jordan nor in the Middle East region, to investigate those reasons. Instability in economy might lead to workers turnover as a result for looking for more satisfaction, higher wages and better working conditions.

The main reason for workers turnover might be different from country to another and from culture to another. So, Jordan, as a country in the Middle East, might have its reasons for large workers flow which does really deserve to be studied and investigated.

2. Literature Review

Many research studies have been made for investigating the main reasons for workers turnover all over the world. In 1998 Bartol and Martin [1] found that two forms of applicant market-referent information, number of applications filed and degree of target organization wage information possessed, were both significantly and positively related to turnover.

Lucifora [2] stated in 1998 that empirical evidence suggests that Italian trade unions have succeeded in reducing turnover.

Lehmann and Wadsworth [3] showed in 2000 that tenure-turnover rates are higher in Russia and lower in Poland than in Britain. Same year Strand [4] related the inefficiencies due to bargaining and externalities in the matching process lead firms to employing too few worker types.

Lambert et. al. [5] study in 2001 found that indicate that the work environment is more important in shaping worker job satisfaction than are demographic characteristics, and that job satisfaction is a highly salient antecedent of turnover intent.

In 2002 Gautier et. al. [6] investigated whether employers exploit cyclical downturns to improve the average skill level of their work force. Their findings are that at each job level mainly lower educated workers leave during downturns. They found no evidence that higher educated workers crowd out lower educated workers during recessions.

Haltiwanger and Vodopivec [7] studied in 2002 the labor market flows of one of the rapid reformers among the transition economies; Estonia, and found that the surge in labor market flows in Estonia contrasts sharply with the experience of other transition economies that pursued more gradual reforms.

In 2005, Tsou and Liu [8] found a negative relationship between wage dispersion and job reallocation, and (excess) worker turnover in Taiwan.

On the other hand Dale-Olsen (2006) [9] found a positive correlation between wages and fringe benefits in Norway. He concluded that higher wages and more fringe

*Corresponding author. wisam@hu.edu.jo

benefits reduce the worker turnover rate. Same year Liu [10] studied again the turnover in Taiwan and found that hiring determines worker entry and quits most strongly contribute to worker exit.

Munasinghe (2006) [11] found that workers with favorable job assessments have a lower and flatter tenure-turnover profile.

Morrison *et. al.* (2006) [12] found that in New Zealand the quitting behaviour of workers is a function of local labour market conditions, non-wage income and the costs and benefits of migration to other local labour markets.

Sousa-Poza and Sousa-Poza (2007) [13] studied the effect of job satisfaction on labor turnover by gender in Switzerland. Their results confirm that job satisfaction is a very good predictor of future quits and here is no apparent difference in firm attachment between men and women.

Senter and Martin (2007) [14] studied the factors affecting the turnover of different groups of part-time workers, and concluded that organizational commitment, job satisfaction, and perceived employment alternatives differentially predict turnover for these part-time groups.

Wheeler provided in 2008 [15] an explanation for the observed positive association between average producer size and the magnitude of an industry's presence within local labor markets. Turnover factors revisited and a longitudinal study of Taiwan-based staff nurses was made in 2008 by Chen *et. al.* [16]. Their study confirms earlier findings on the relationships among turnover determinants, job satisfaction, and intent to stay, and suggests a more comprehensive selection of turnover factors must be taken into account when attempting to explain variations in actual turnover.

McKnight *et. al.* studied in 2009 [17] the factor that reduces IT turnover intention the most, the job characteristics or the workplace characteristics. They found that workplace characteristics out-predicted job characteristics.

Based on literature discussed above, no comprehensive study has been made for all factors affecting the turnover. Moreover, no such a study has been made on workers in the Middle East region.

3. Problem Statement and Solution Technique

3.1. Problem Statement

Workers turnover is very expensive issue, especially for a third world developed country like Jordan. In the last few years, Jordan started to attract many industries from all over the world by offer the convenient environment to have successful business.

Factories in Jordan are distributed over the three largest cities, Amman, Zarqa and Irbid. Many of the factories are located in industrial cities in these largest cities, but other factories still there outside these industrial cities. The industrial cities are Sahab industrial city in Amman, AlDulail industrial city in Zarqa and AlHasan industrial city in Irbid. The establishment of these industrial cities intended to improve and support the industrial sector and introduce all possible services for as much industries as possible.

Since Amman, Zarqa and Irbid contain more than 90% of the Jordanian population; the study was limited to these three cities. The workers turnover from factories in these three largest cities caused instability both in the production capacity and the production quality. Shortage in number of workers led to decreasing production capacity, and leaving skilled and experienced works and hiring prospective works led to decreasing the products quality. On the other hand, the increase in the workers turnover affected not only the industrial sector and the country economy, but also the Jordanian community and social life of the Jordanian. As the number of factories and industries is increasing, as the workers turnover problem is getting larger.

For all these reasons this study is trying to investigate this workers turnover issue to find the main reasons which lead to this phenomenon, and so it is the first main step for reducing the effects of this problem.

3.2. Solution Technique

A questionnaire was designed such that it includes five main categories; Category A is the salary, Category B is the working environment, Category C is the helpfulness and corporation of the management, Category D is worker psychological state and relationships with surrounding environment, Category E is the services provided by the employer to the employee. Each category contained many questions, and the answers ranged from strongly agree with a load of 5 to strongly disagree with a load of 1. Strongly agree means that question was not really a reason for turnover. While strongly disagree means this question is a reason for turnover. So, as the average points a question achieve is lower as that question is qualified for being a reason for turnover. On the contrary if the average a question achieve is high, then that means this question is away from being a reason for turnover.

The question was distributed over twenty one factories, seven factories in each of the industrial cities. Seven more factories located in the largest cities but outside the industrial cities were also chosen to be included in this study. In each factory, the 50% of the sample was from workers who already turned over and left the factory in the last two years, and 50% of the sample was from people still working in their jobs. Equal number of questionnaires was collected from all factories to be around 80.

All questionnaires results were analyzed using Excel and by comparing the average achieved by each question in the questionnaire, the main reasons for workers turnover were determined.

3.2.1. AlDulail Industrial City

AlDulail industrial city represents a village community that is located far from the capital city Amman, where people are relatively poor with lower level of education than people live in big cities like Amman. And so AlDulail city represents the community of people who do not have a main career, like AlHasan industrial city where people live mainly on cultivation, or higher level of education and standards of living, like people live in the capital city, Amman.

Figure 1 compares the averages of the different categories. It can be clearly seen that criterion E, the services provided by the employer to the employee, has the

highest average value of 3.21, to be the least important issue for workers turnover in that industrial city. Mainly that is related to village community are not looking for superior services, and they accept to live very simple life with basic needs available. On the other hand criterion A, the salary, has the greatest effect on workers turnover with an average value of 2.41. The explanation for this is that AlDulail industrial city is located in relatively poor region, where the effect of world wide inflation is influencing more. But, since AlDulail is not a rich city, services by employer there are relatively sufficient and so workers are not expecting more in this direction from their employer, which makes salary the main reason for workers to turn over.

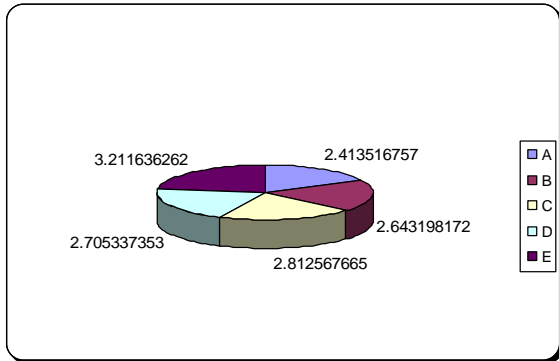


Figure 1. Comparison of A-E criteria of AlDulail industrial city

3.2.2. Sahab Industrial City

Sahab industrial city is located near the capital city Amman. People working in that industrial city usually live in Amman. Results of the questionnaire in that industrial city are summarized in Figure 2. It shows that the criterion C has the highest average of 3.0, to be the least effect reason for workers turnover in Sahab industrial city. So, the management is helpful in Sahab industrial city and that reduces workers turnover there.

Salary again is an issue to force the workers to leave their jobs in Sahab industrial city. The lowest average was for criterion A, with a value of 2.38. That average was even lower than that corresponding average of AlDulail industrial city. That was expected result as people work in Sahab industrial city mostly live in Amman as the questionnaire shows, and Amman is very expensive compared to AlDulail and AlHasan cities. So, workers there may suffer from low salaries more than workers of AlDulail industrial city.

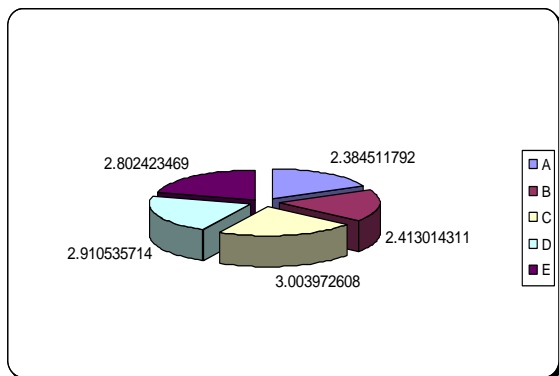


Figure 2. Comparison of A-E criteria of Sahab industrial city

3.2.3. AlHasan Industrial City

Although AlHasan industrial city is located in the north far from the capital city Amman, it shares same reasons for workers turnover with Sahab and AlDulail industrial cities. The lowest average was for the criterion A with a 2.43 value. It is a little higher than that corresponding value for Sahab and AlDulail industrial cities. That is mainly related to life nature around AlHasan industrial city that is located in the cultivation community and life there is much cheaper than that in the capital city Amman. The criterion with the highest average was D, worker psychological state and relationships with surrounding environment. Usually communities depending on cultivation in their lives have better psychological state and relationships with surrounding environment, than communities of big cities.

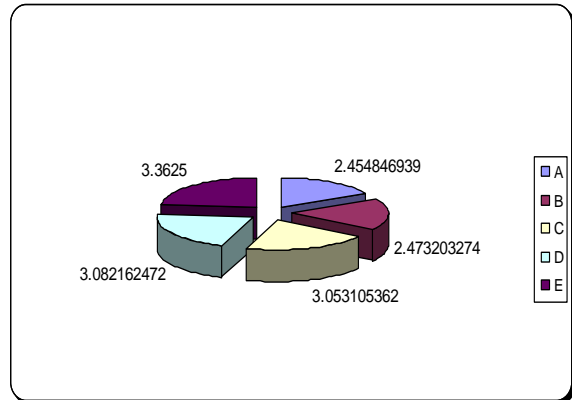


Figure 3. Comparison of A-E criteria of AlHasan industrial city

3.2.4. Industrial Cities in Jordan

Industrial cities are a healthy phenomenon that started to appear in Jordan in the last two decades. Instead of having factories distributed here and there all around the city, all or most factories located in that city are placed in one region that has special services and treatments, called the industrial city. Figure 4 summarizes the results of the three main industrial cities in Jordan. Workers in the three industrial cities agree that the salary is their main concern to leave their jobs there.

The next factor that might be a reason for workers turnover from industrial cities was the working condition and environment. On the other hand a reasonable satisfaction was achieved for the services provided by the employer.

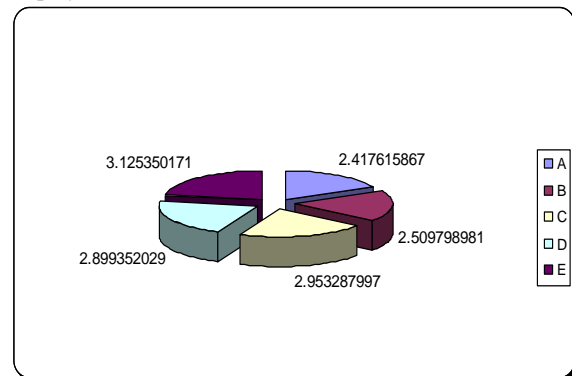


Figure 4. Comparison of A-E criteria of industrial cities in Jordan

3.2.5. Factories Outside Industrial Cities in Jordan

Seven factories located in the capital city Amman but outside any of the three industrial cities were included in survey of this study. The results of these factories are summarized in Figure 5.

Compared to results of factories located in industrial cities, it can be noticed here that the main reason for possible workers turnover is the worker psychological state and relationships with surrounding environment, in contrast to salary that was the main reason for workers turnover in factories located inside the industrial cities. That might be related to the fact that factories outside the industrial cities usually look for professional and experienced workers and so they pay them good salaries and of course expect from them more. That put the workers under stress all the time and makes the main reason for possible turnover is the psychological state of the workers.

Investigating all results in Figure 5 indicated that averages of all criteria are low compared to corresponding criteria for industrial cities. Which means the general satisfaction of workers in factories inside industrial cities is much more than the satisfaction of workers in factories outside industrial cities. That might be related to services and facilities provided by the government to those industrial cities. So, generally the workers turnover problem severity is more for factories located outside industrial cities, especially those factories looking for profession and experienced workers.

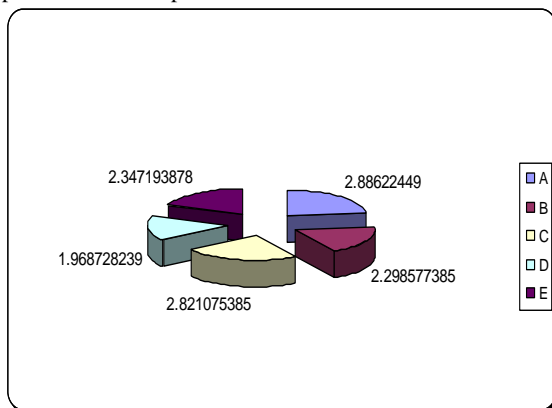


Figure 5. Comparison of A-E criteria of factories outside industrial cities in Jordan

3.2.6. Overall Turnover Results

Combining the results of the factories inside the industrial cities and the results of factories located outside the industrial cities to achieve an overall idea about the workers turnover problem in the industrial sector in Jordan, gave results summarized in Figure 6. As results show the main reason for possible turnover in industrial sector in Jordan is the working conditions and environment. Then the salary factor comes to be the second factor for turnover. Other factors have less effect on turnover issue.

The least factor affecting the turnover is criterion E, the services provided by the employer. It looks that employees are satisfied with services provided. Average values for all

criteria show that all of them are above 2.5 except criterion B. That means the only dissatisfaction is in the working conditions and environment. But other factors are not really issues for turnover.

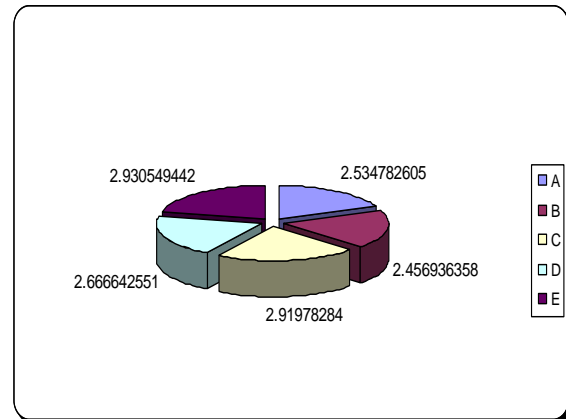


Figure 6. Comparison of A-E criteria of industrial sector in Jordan

4. Conclusions and Recommendations

Based on the study results, the main conclusions can be summarized in the following points:

- For factories located in big cities, the main reason for possible turnover is the salary then the working conditions and environment.
- For factories located outside big cities in farm regions, where people live mainly on cultivation, same two reasons for turnover as factories located in big cities, but with much less severity.
- For factories located in villages, where people live mainly on sheep, the only possible reason for turnover is the salary with less effect than that of big cities.
- People living in big cities suffer more from low salary than people living in farm regions and from poor people living in villages.
- Generally, turnover of workers from factories located in industrial cities is related to salary, but for factories located outside industrial cities, the reasons for possible turnover are the worker psychological state and relationships with surrounding environment, working conditions and environment and services provided for employee by the employer.
- In Jordan, as an example of Middle Eastern countries, the industrial sector has a problem of workers' turnover that is related mainly to working conditions and environment. So, those working conditions should be improved to reduce the turnover problem.

References

- [1] K. Bartol, K., D. Martin, "Applicant referent information at hiring interview and subsequent turnover among part-time workers". *Journal of Vocational Behavior*, Vol. 53, 1998, 334-352.
- [2] C. Lucifora, "The impact of unions on labour turnover in Italy: evidence from establishment level data". *International Journal of Industrial Organization* Vol. 16, 1998, 353-376.

- [3] H. Lehmann, J. Wadsworth, "Tenures that shook the world: worker turnover in Russia, Poland, and Britain". *Journal of Comparative Economics*, Vol. 28, 2000, 639-664.
- [4] J. Strand, "Wage bargaining and turnover costs with heterogeneous labor and asymmetric information". *Labour Economics*, Vol. 7, 2000, 95-116.
- [5] E. Lambert, N. Hogan, S. Barton, "The impact of job satisfaction on turnover intent: a test of a structural measurement model using a national sample of workers". *The Social Science Journal*, Vol. 38, 2001, 233-250.
- [6] P. Gautier, G. Berg; J. Ours, G. Ridder, "Worker turnover at the firm level and crowding out of lower educated workers". *European Economic Review*, Vol. 46, 2002, 523-538.
- [7] J. Haltiwanger, M. Vodopivec, "Gross worker and job flows in a transition economy: an analysis of Estonia". *Labour Economics*, Vol. 9, 2002, 601-630.
- [8] M. Tsou, J. Liu, "Wage dispersion and employment turnover in Taiwan". *Economics Letters*, Vol. 88, 2005, 408-414.
- [9] H. Dale-Olsen, "Wages, fringe benefits and worker turnover". *Labour Economics*, Vol. 13, 2006, 87-105.
- [10] D. Liu, "The entry and exit of workers in Taiwan". *Economics Letters*, Vol. 92, 2006, 330-332.
- [11] L. Munasinghe, "Expectations matter: Job prospects and turnover dynamics". *Labour Economics*, Vol. 13, 2006, 589-609.
- [12] P. Morrison, K. Papps, J. Poot, "Wages, employment, labour turnover and the accessibility of local labour markets". *Labour Economics*, Vol. 13, 2006, 639-663.
- [13] Sousa-Poza, A. Sousa-Poza, "The effect of job satisfaction on labor turnover by gender: An analysis for Switzerland". *The Journal of Socio-Economics*, Vol. 36, 2007, 895-913.
- [14] J. Senter, J. Martin, "Factors affecting the turnover of different groups of part-time workers". *Journal of Vocational Behavior*, Vol. 71, 2007, 45-68.
- [15] Wheeler, "Worker turnover, industry localization, and producer size". *Journal of Economic Behavior & Organization*, Vol. 66, 2008, 322-334.
- [16] H. Chen, C. Chu, Y. Wang, L. Lin, "Turnover factors revisited: A longitudinal study of Taiwan-based staff nurses". *International Journal of Nursing Studies*, Vol. 45, 2008, 277-285.
- [17] McKnight, B. Phillips, B. Hardgrave, "Which reduces IT turnover intention the most: Workplace characteristics or job characteristics?" *Information & Management*, Vol. 46, 2009, 167-174.

Computer Aided Design Tools in the Development of Surface Micromachined Mechanisms

Mohammad I. Kilani *

Mechanical Engineering Department, King Faisal University, Al-Ahsa 31982, Saudi Arabia

Abstract

This paper describes a number of computer aided design (CAD) tools that are used in the development of surface micromachined mechanisms. It investigates the application of parametric or constraint-based CAD in the design of these mechanisms. Parametric CAD facilities are compared with conventional CAD facilities in this paper. The advantages and limitations of conventional and parametric CAD are illustrated by describing their application in designing an electrostatically actuated crescent pump mechanism, which was fabricated in five levels of silicon using Sandia's Ultraplanner Multilevel Micromachining Technology (SUMMiT-V). The paper also describes the application of visualization and motion simulation tools in designing surface micromachined mechanisms.

© 2011 Jordan Journal of Mechanical and Industrial Engineering. All rights reserved

Keywords: CAD, MEMS, Surface Micromachining, Parametric Constraint-Based CAD.

1. Introduction

The past few decades have witnessed the emergence of the field of microelectromechanical systems (MEMS) as an outgrowth from the silicon revolution. MEMS systems are produced from the integration of mechanical elements with electronics on a common silicon substrate through microfabrication. The electronics on a MEMS system perform arithmetic, logical and intelligence functions and are fabricated using integrated circuit (IC) process sequences (e.g., CMOS, Bipolar, or BICMOS processes). On the other hand, the mechanical components perform sensing and/or actuation functions and are fabricated using photochemical lithographic processes that selectively etch away parts of the silicon wafer, or add new structural layers to form the mechanical and electromechanical devices. A number of MEMS mechanisms have been developed for applications ranging from accelerometers to mirror arrays [1-3]. More complex mechanisms have been developed for systems such as lab on a chip and micropumps [4-9]. These systems and are expected to impact disciplines such as biology, medical sciences, and others.

One particularly promising MEMS technology is surface micromachining [10], which leverages on the highly developed IC fabrication toolset, and provides the ability of batch fabricating hundreds to thousands of MEMS devices, together with drive and control electronics fully assembled on a single silicon substrate. In this

technology, MEMS devices are built from a number of stacked polycrystalline silicon (polysilicon) films, consecutively deposited and patterned on top of a silicon wafer. Layout and visualization CAD tools traditionally used for IC fabrication were employed in surface micromachined mechanism design [11, 12]. However, the increased number of mechanical layers, and the mechanical complexity of surface micromachined mechanisms, increased the demand on the MEMS mechanism designer. Unlike an IC designer, a MEMS mechanism designer must visualize the three dimensional geometry, and motion of the target device from a set of planar mask patterns, besides verifying its conformity with the proposed fabrication process.

The paper describes the facilities provided by the generic and customized layout and visualization CAD tools in developing surface micromachined mechanisms and investigates the application of parametric constraint-based CAD in surface micromachined mechanisms design. As a case study, the advantages, limitations and improvement prospects of these tools are illustrated by describing their application in designing an electrostatically actuated crescent pump mechanism, which was fabricated in five levels of silicon using Sandia's Ultraplanner Multilevel Micromachining Technology (SUMMiT-V) [9]. Section 2 provides an overview of the fabrication and design of surface micromachined mechanisms. Section 3 outlines the design, operation and fabrication of the surface micromachined crescent pump used as a case study in this work. Section 4 describes the application of conventional layout tools in the design of surface micromachined mechanisms and section 5 investigates the potential benefits of parametric CAD in

*Corresponding author. malkilani@kfu.edu.sa

the design of those mechanisms. Section 6 describes the visualization and motion simulation tools in surface micromachined mechanisms.

2. Overview of the Fabrication and Design of Surface Micromachined Mechanisms

Surface micromachined MEMS are built from a number of stacked polycrystalline silicon (polysilicon) films, consecutively deposited and patterned on top of a silicon wafer. The standard building-block fabrication process consists of depositing and photolithographically patterning alternate layers of low-stress polycrystalline silicon as the structural material and silicon dioxide as the sacrificial material. The sacrificial layers provide a temporary standoff for the structural layers and are selectively etched away in hydrofluoric acid (HF) at the end of the process, leaving the free-standing polysilicon layers. Holes etched through the sacrificial layers provide anchor points between the mechanical layers and the substrate. The use of the center-pin and the flange processes [13], [14] allow creating a revolute joint between two of the polysilicon levels. The result is a system of mechanical polysilicon structures capable of producing complex mechanical movement involving linear and angular translation, reciprocation, oscillation and continuous rotation.

Sandia's Ultra-planar Multi-level MEMS Technology (SUMMiT) is a standard surface micromachining process [15]. It uses five levels of stacked polysilicon films labelled POLY0 through POLY4 as structural material, and four levels of intervening silicon oxide layers labelled SOX1 through SOX4 as sacrificial material. Each sacrificial SOX n film resides between a POLY n and a POLY $n-1$ film and gets etched away in the final release process. This allows creating elaborate structures due to the great design freedom in defining the in-plane shapes of the structural and sacrificial films, and the provision of revolute joints between the POLY1 and POLY2 films. Freely rotating elements and free-spinning gears can be created. SUMMiT devices ranging from pressure sensors and gas sensors to complex gear trains and microengines have been demonstrated [16, 17].

The design of a device that is to be fabricated via SUMMiT fabrication process requires the designer to produce the layout drawings for the mask of each patterning step of the fabrication process. Depending on the number of structural and sacrificial levels used in the device, as many as 14 masks may be needed to produce a design. These include 9 masks for the structural polysilicon and the sacrificial oxide levels and 5 masks to produce dimples or pin joint cuts between the structural polysilicon levels. Pin joint cuts allow rotational freedom between two polysilicon levels, while dimples allow for creating protrusions to prevent the polysilicon films from sticking to one another during movement. A mask is a two-dimensional design representation that will be patterned and etched into the structural or sacrificial material to produce the desired artefact. The mask set is the interface between design engineer's information (i.e., design), and the fabrication process.

The SUMMiT design tool suite utilizes the two-dimensional geometric layout capabilities of AutoCAD,

which has the full set of geometric entities to facilitate complex mechanical design. To help the designer verify that the masks conform with the fabrication process, a number of design rules were developed. These rules are a set of requirements and advisements for the designer. Design rule checking tools were also developed and added to MEMS CAD systems [18]. These tools analyze the MEMS layout and examine if the size, spacing and overlap of geometry are correct for the fabrication process. After executing the design rule check, the results are loaded into the drawing session. Advisory rule violations and mandatory rule violations are displayed, and the design must be modified until no mandatory rules are violated.

3. Design, Operation and Fabrication of a Surface Micromachined Crescent Pump

The conceptual design and operation of the crescent pump used as a case study in this work may be described with reference to Figure 1. The pump utilizes a ring gear driven through teeth on its outer surface to drive the pumping mechanism through the triangular teeth on its inner surface. The outer teeth of the ring gear are not shown in the illustration of Figure 1. The inlet and outlet ports are located inside the ring gear and the pumped fluid is maintained in the inner vicinity of this gear. The ring gear has internally cut teeth, which mesh with the teeth of an externally cut idler gear that is set off-center from the ring gear. The crescent is fixed and divides the flow between the idler gear and the rotor. As the ring gear and the idler rotate in the counter clockwise direction, the gear teeth come out of mesh in the left side of the pump. This motion creates a partial vacuum, which draws fluid into the pump. The fluid is transferred to the right side of the pump between the rotating gear teeth and the fixed crescent. As the rotating gears mesh together in the right side of the pump, they generate an increase in pressure that forces the fluid into the outlet line. A gear pump can discharge fluid in either direction, depending on the direction of the gear rotation. Crescent pumps have two advantages. First, they can operate with no valves, simplifying their design and improving their reliability, and second, fluid is contained in the vicinity of the ring gear and is naturally sealed from the outer devices.

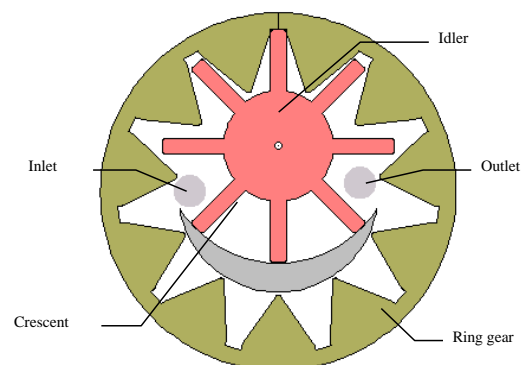


Figure 1. Crescent pump concept

A surface micromachined crescent pump fabricated from five levels of polysilicon is shown in Figure 2. The pump was produced using Sandia National Laboratory's Sandia Ultra-planar, Multilevel, Micromachining Technology (SUMMiT V) process and utilized all five layers of the technique. A torsional ratchet actuator in the

bottom of the figure combined with a transmission gear train provides the power needed to actuate the ring gear of them pump. Figure 3 illustrates the mask layouts for the five structural polysilicon levels used in the crescent pump mechanism shown in Figure 2.

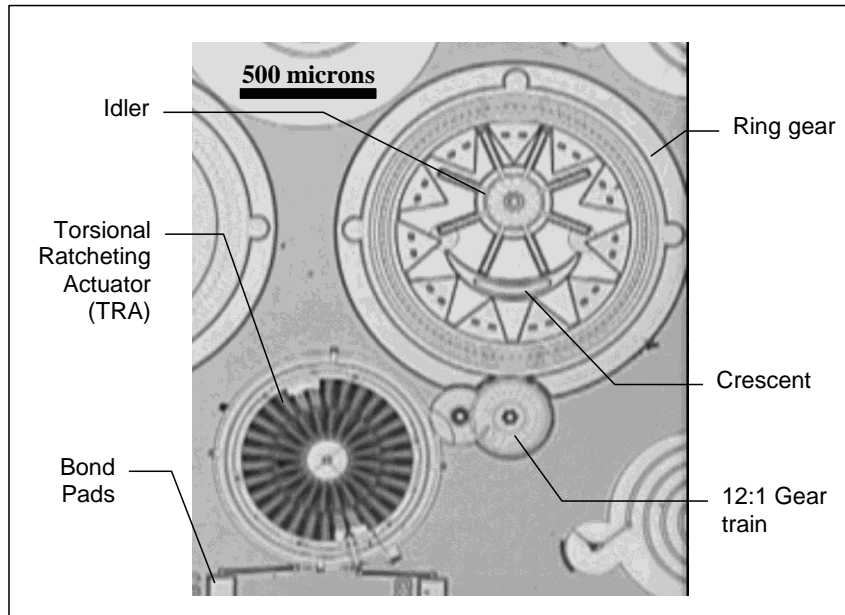


Figure 2. A Crescent mechanism fabricated in SUMMiT

4. Conventional Layout of Surface Micromachined MEMS

Construction, modification, inquiry and organization layout tools found in conventional CAD systems allow the creation of the geometric patterns in the masks of surface micromachined mechanisms. Construction commands are used to create the various geometric entities into the drawing database, including the lines, circles and arcs. Modification commands, such as scale, erase, move, array, etc. allow for the interactive modification of patterns to reach the desired mask layout. Inquiry commands are used to obtain information from the system on the locations, distances, angles, lengths and areas pertinent to the created geometry, and are useful for checking the correctness and accuracy of the design.

Organization tools allow the designer to group and/or separate certain geometric entities for the purpose of construction, modification or visualisation. Typical organization tools include layer tools and compound entity or block tools. Layer tools allow the designer to separate the design into different layers, which may be turned on or off, or assigned different colours or line types. One useful strategy in organizing surface micromachined MEMS is to group the entities belonging to each mask pattern on a different layer and assign different colour for that layer. Thus, a designer can edit, and examine each mask pattern separately, and can examine the pattern in relation with any other pattern or group of patterns on the complete mask set. In creating the mask layout for the crescent pump mechanism, geometric entities belonging to each polysilicon level or sacrificial oxide level were assigned to a different layer.

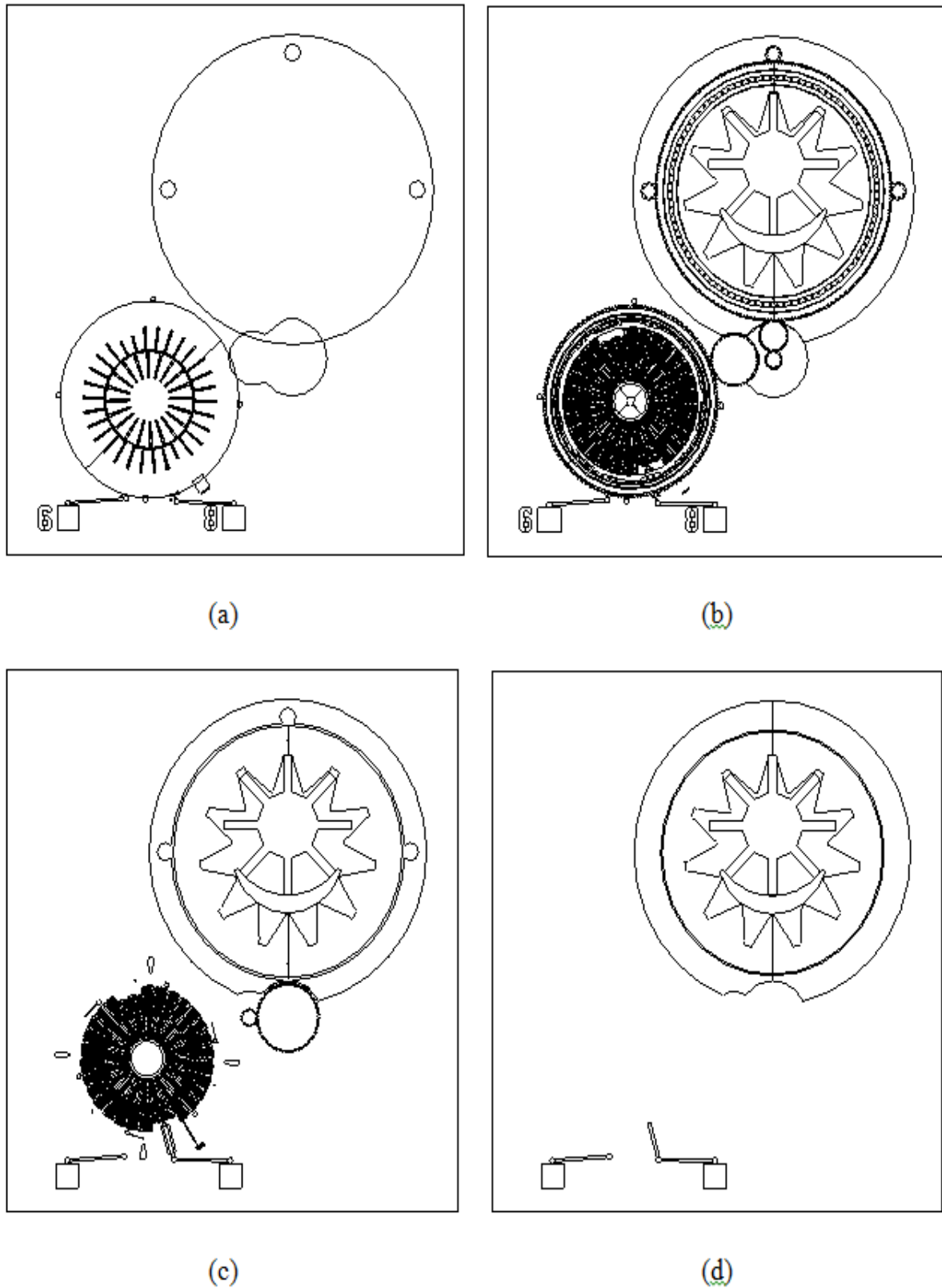


Figure 3. Mask layouts of the structural polysilicon levels for the pump in Fig. 2 (a) level 0 (Poly 0), (b) level 1 and level 2 (Poly 1 and Poly 2), (c) level 3 Poly 3 and (d) level 4 (Poly 4)

Compound entity tools of current CAD layout systems allow grouping a number of geometric entities together to create a new entity, which may be inserted into the drawing and manipulated as a single entity. This facility allows for the creation of standard component libraries for repeatedly used items and provides a convenient pick and place capability for such components. Current surface micromachined MEMS layout environments provide an assortment of library items for standard parts refined over the years by component designers. Selecting an item from the library automatically generates the entire mask layouts needed to produce that component on the wafer. This liberates the designer from 'reinventing' these components. Library items encompass a significant amount of design expertise, refined over the years by component designers. For a surface micromachined mechanism designer, a library component saves time and works as an important tool of experience sharing between designers.

Once in the drawing database, a library component may be translated and/or rotated according to the design requirements while still generating the mask layouts for the component in the new location, and without violating any of the design rules pertaining to the process. Scaling a library component in a traditional CAD system, however,

would scale all the dimensions uniformly, which may result in violating the minimum line/space design rules, and leads to missing, undersized, oversized or fused features.

A standard components library, integrated into the SUMMiT's design interface, was used in defining some of the basic components of the crescent pump mechanism of Figure 2. The gear train, the torsional ratcheting actuator (TRA), and the bond pads were accessed from that library. This helped ensure the correct operation of these components in the assembly.

When the design contains internal cuts or holes, it is convenient to place them on a negative mask layer in order to simplify the production of the needed layout. Consider for example the layout for the POLY2 level of the idler of the crescent pump mechanism. The idler has an annular cut for hub clearance and 12 etch release holes symmetrically located around its axis of rotation. Setting the complete layouts of the idler in one positive mask, requires the designer to define the shape of the idler as a number of solid parts, which when joint together would produce the desired hole or internal cut, as illustrated in Figure 4. In this case, the symmetry of the shape was utilised and a polar array of four elements was invoked to produce the desired region with the holes and cuts inside as shown in Figure 4(c).

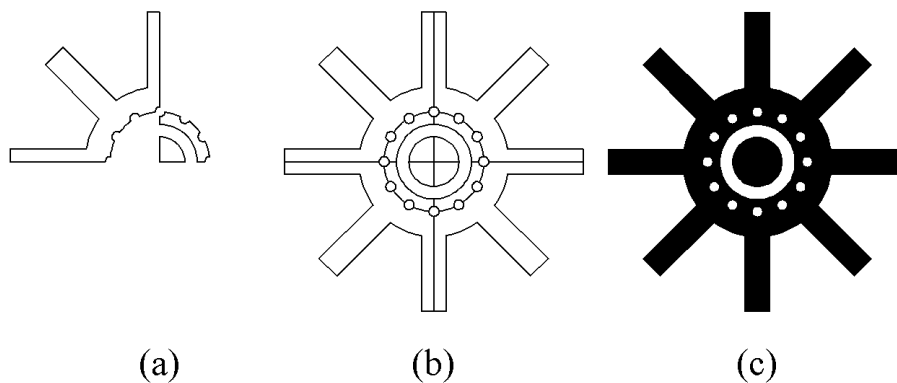


Figure 4. Defining the mask layout for the idler gear using only a positive mask set.

(a) positive mask regions. (b) polar array and (c) resulting region

Note that the polar symmetry property of the idler gear was utilized to simplify the generation of the layout in Figure 4. The production of this layout would be much more difficult if a larger number of etch release holes were needed and if polar symmetry did not exist. It is common to use as many as 100 etch release holes in some designs.

To deal with such cases, positive and negative masks would be conveniently used. As seen in Figure 5, the etch release holes and the hub clearance are defined in the negative mask and the external body of the idler is defined on a positive mask. The resulting mask shown in Figure 5 (c) is the same as that of Figure 4, but the construction procedure is simpler.

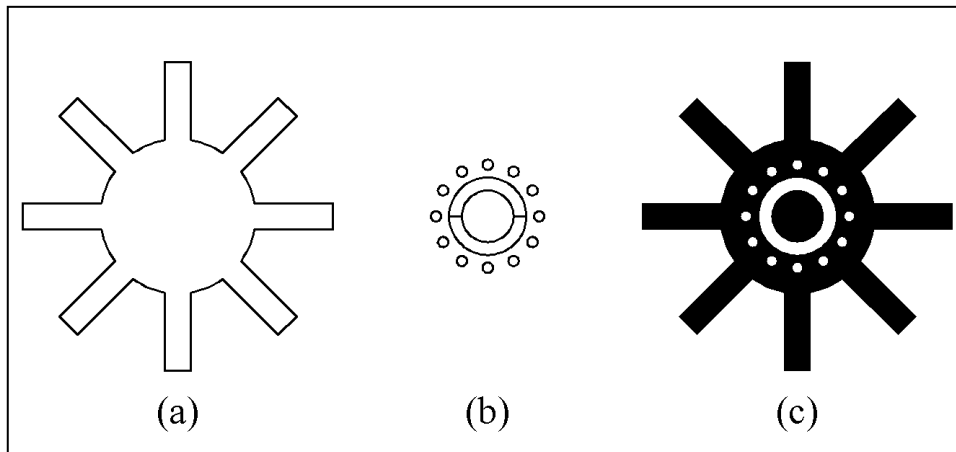


Figure 5. Defining the mask layout for the idler gear using positive and negative mask sets.

(a) positive mask regions. (b) negative mask and (c) resulting region

Some CAD systems provide facilities for converting closed polygons and circles into topological regions in order to perform union, difference and intersection operations. These operation can be employed as an alternative to using positive and negative mask sets. The result of applying a cut to the polysilicon level can be obtained by subtracting the regions of the cut from those on the body, resulting in the desired shape layout.

When laying out the design of a surface micromachined mechanism, the designer needs to verify that the resulting layout conforms with the proposed fabrication process. To help ensure the greatest possibility of successful fabrication, a number of design rules have evolved, which are a set of requirements and advisements for the designer defined by the capabilities of the individual process steps. In general, these rules are defined by the resolution and alignment capabilities of the lithography system. Both mandatory and advisory rules exist, and they define the minimum feature sizes and spaces for all levels and minimum overlap and spacing between relevant levels. The minimum line widths and spaces are mandatory rules. Violation of these rules will result in missing, undersized, oversized or fused features. Minimum overlap (enclosure, cut-in and cut-out rules) requirements reduce the effect of large topographies and prevent unnecessary etching of underlying layers. Minimum spacing between levels guarantees that features of two different levels can be delineated by photolithography and etch.

To help the designer confirming to the posted rules, design rule check tools were developed. The MEMS layout includes 2D polygons, arcs and circles placed on predefined layers, and a design rule check may be invoked in order to check that the developed design does not violate any of intended process design rules. As many of the rules are concerned with eliminating the overlap between the different polysilicon or sacrificial oxide layers, Boolean operations may be utilized in checking the validity of the design. Boolean operations may be invoked to check if an overlap exists, and its extent.

5. Parametric Layout of Surface Micromachined MEMS

When constructing the layout in a conventional CAD system, the user specifies the location of the individual entities in the drawing in absolute coordinates, or relative to other entities in the drawing, which the user can select on the screen using various snap techniques. The system stores only the absolute coordinate of the resulting entity with respect to a global or Word coordinate system. These coordinates are stored in the model's database and are used for editing, printing and other purposes. Besides storing absolute or relative coordinates, parametric CAD systems create and maintain a set of constraints between the geometric entities created by the designer. Tangency, perpendicularity, parallelism, concentricity, and other relations may are recognized [19, 20]. The internal representation of constraints may be expressed as a network of equations or predicates. A constraint solver is then used to evaluate the absolute coordinates of all the entities in the network.

When creating a layout in a parametric design system, the designer first defines the topology of each shape in the layout by sketching lines, arcs and other entities in approximate coordinates. The designer then creates a number of geometry or dimension constraints in order to accurately define the geometry of the sketch. Constraints may be applied to an individual entity such as the length of a line or the radius of a circle, or may be applied as a relation that defines a dependency between two or more of the sketched entities such as constraining two lines to be parallel, or three circles to be concentric. Relations between the entities in the sketch reduce the number of free dimensions needed to completely define it, and the remaining free dimensions are called *parameters* that the user is allowed to manipulate to complete the sketch. The designer may edit the shape by changing one or more of its defining parameters.

As an introductory example, consider the layout of the rectangle in Figure 6(a). In a parametric system, the rectangle may be defined by four lines and three perpendicularity constraints. Note that only three

perpendicularity constraints are needed as the perpendicularity condition between the right and bottom sides of the rectangle is implied due to the fact that the sum of the internal angles of a quadrilateral is equal to 360 degrees. The three constraints leave two free parameters, the length of the rectangle, d_1 , and its width d_2 , to fully define it. When the three perpendicularity constraints are enforced, the designer can create rectangles of different lengths and widths by simply changing the values of d_1 or d_2 . If an additional equality constraint is imposed between the right side and the bottom side of the rectangle, as shown in Figure 6(b), the shape is further constrained to become a square, fully defined by specifying the length of its side.

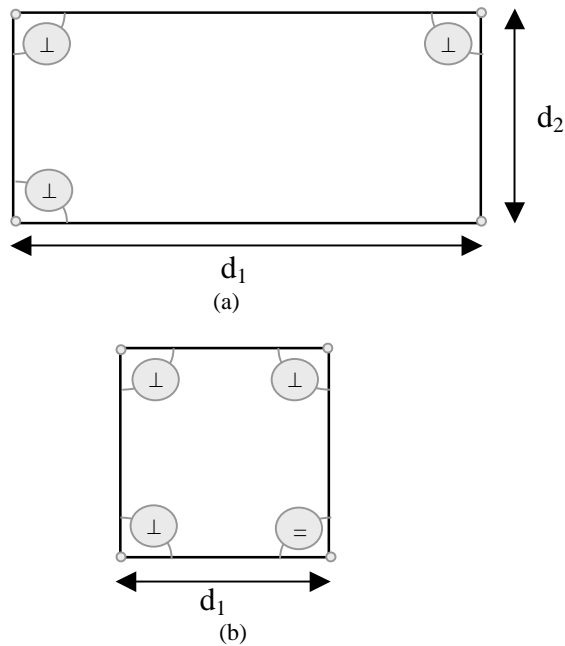


Figure 6 (a) Rectangular shape and (b) Square shape defined in a parametric CAD systems

The advantages of using a constraint based design system include faster creation of shapes because the designer specifies approximate rather than exact coordinates. Further editing and changes to the design is simplified because it is performed by changing few key parameters, while the constraints are observed. This reduces error possibility by propagating relations to other shapes in the design across layers.

A component is modified in those systems by changing one or more of its defining parameters, and the constraints will be observed in the result. This paradigm allows editing operations to be performed without running the risk of violating the design rules imposed. Additionally, a parametric or constraint-based design system affords an explicit representation of design rules in the item definition, leading to a richer and more transparent form of knowledge representation. Explicit constraints allow the designer to specify the mandatory or advisory rules in the form of constraints between its graphical entities. The designer can then change design parameters while the rules are satisfied.

An example of the application of parametric constraint-based layout tools in surface micromachined mechanisms design may be illustrated with reference to the layout of the idler gear of the crescent mechanism of Figure 5. The

hub clearance needed to provide the rotational freedom of the idler's hub consists of the two half rings adjacent to one another as seen in the Figure. The minimum spacing between the outer arc and the inner arc is specified in the design rules to be 3 microns, and we assume the designer has used a design with this minimum spacing. If the designer adjusts the inner radius in a conventional layout setting, he needs to explicitly adjust the outer radius while making sure that the minimum spacing condition is not violated. Attempting to scale down the ring will scale the spacing between the two arcs and the design rule will be violated. A parametric layout system, however, allows specifying the radius of the outer arc in terms of the inner arc. The constraint relationship may be $r_o = r_i + 3$, where r_o and r_i denote the outer radius, and the inner radius, respectively. The resulting layout for the hub clearance is thus effectively defined in terms of one parameter. If the inner radius is changed, the outer radius is updated based on the constraint imposed, and vice versa. Propagation of this parameter to other elements in the design, and may also be defined in terms of other elements.

Library components of surface micromachined design environments have evolved after many design iterations involving experimentation, modification and refinement. Employing a parametric design paradigm in a component library significantly increases its experience sharing value. Consider the process of scaling a library component without violating the design rules. This requires preserving the relational constraints embodied in these rules. In parametric CAD systems, the component designer can define a set of constraints on the dimensions of the group, and these constraints will be observed whenever the component is edited, which would allow scaling the component without violating the design rules. Additionally, the relations, associations and constraints defined in a parametric design system allows capturing a deeper form of design expertise into the component, significantly increasing the knowledge sharing value of the component libraries.

6. Visualization and Motion Simulation

The increased number of mechanical layers, and the mechanical complexity of surface micromachined mechanisms increases the demand on the designer, who is needed to visualize the three dimensional geometry, and motion of the target devices from a set of planar mask patterns, besides verifying its conformity with the proposed fabrication process.

MEMS designer needs to combine the fabrication process information with two-dimensional mask geometry to visualize the target MEMS device. The 2D mask set does not reveal the true three-dimensional structure of the target MEMS device, and the result is highly dependent on the employed process sequence. Custom-made visualization tools help the designer visualize the target MEMS structure during the design stage, and before fabrication by applying the process sequence to the mask set to produce a representation that reveals the target device to the designer. Commonly used visualization tools include cross-section visualizers and geometry modellers. A cross-section visualizer generates a cross sectional view

of the target MEMS structure at a location specified by the designer on the mask set. A geometry modeller generates a 3D solid model from the 2D mask layout allowing the designer to examine the target device from different angles and viewpoints. Those tools extract 2D mask geometry from the design layout and apply the process sequence to the mask set resulting in a representation that reveals the target device to the designer. A 2D visualizer generates a cross sectional view of the target MEMS structure at a location specified by the designer on the mask set. A 3D geometry modeller, on the other hand, generates a 3D solid model from the 2D mask layout allowing the designer to

examine the target device from different angles and viewpoints

Figure 7 demonstrates a cross sectional view for the crescent mechanism at the idler's centreline generated by a cross-section visualizer custom made for SUMMiT [21]. The section shows the different polysilicon levels used on the idler's body, and illustrate the formation of a hub in the central region of the idler to form a pin joint between the idler and the substrate. The cross section is generated from the entities on the layout and confirms that the idler will be physically separated from the hub, and free to rotate.

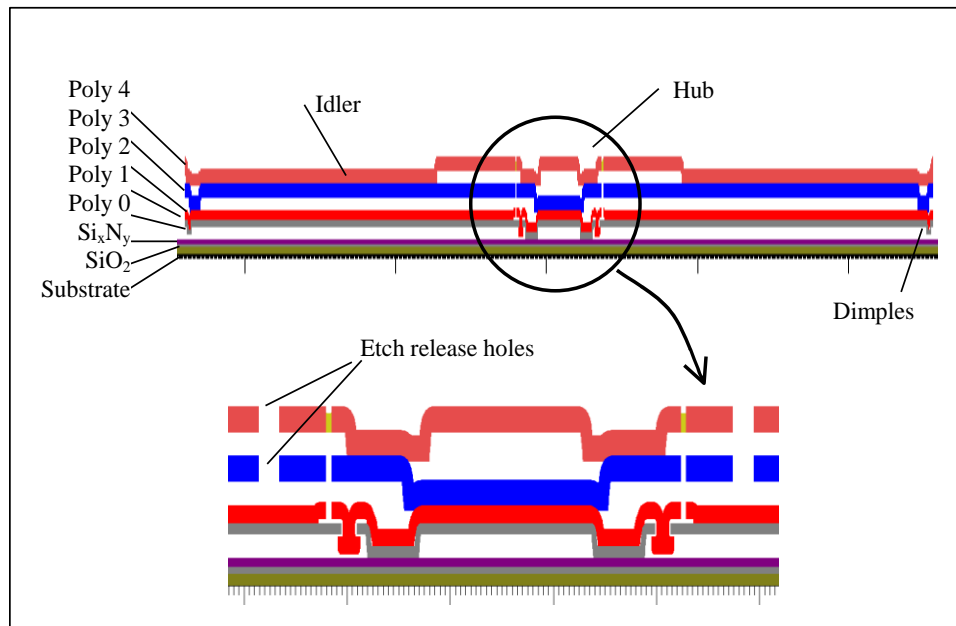


Figure 7. A section through the idler generated by A Cross Section Visualizer.

A geometry modeller generates a 3D solid model for the target MEMS device from the 2D mask layout [22]. Like a section visualizer, a geometry modeller works by interpreting the design layout based on the process definitions. The resulting interpretation is a 3D solid model of the target MEMS device which allows visualizing the true 3D geometry of the MEMS device. An example solid model generated for the crescent pump mechanism using a 3D geometry modeller is shown in Figure 8. The model shows the ring gear, the idler, the crescent, and the inlet and outlet holes. Because it generates a complete representation of the target MEMS device, a geometry modeller is capable of predicting process artefacts including stringers and trapped oxide.

Geometry modellers are convenient tools which help visualize the 3D geometry of the target MEMS device. An additional benefit of the generated solid model is that it can be used for finite element analysis, kinematic and dynamic simulation, rapid prototyping, and other downstream activities. This capability requires a complete and seamless integration between the geometry modeller and the different analysis programs.

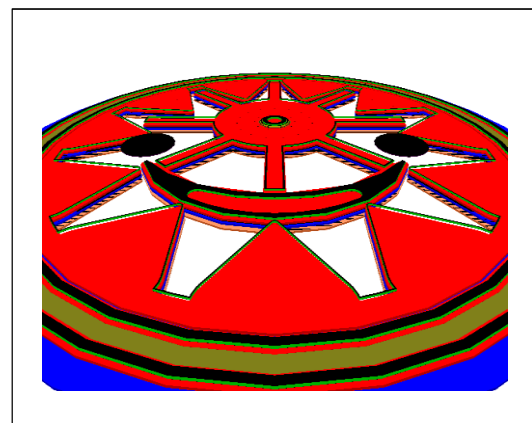


Figure 8. A model for the crescent mechanism generated by a geometry modeller

To help the surface micromachined mechanism designer visualize the motion of the target mechanism, motion simulation software tools are used. These are particularly useful when the mechanism includes revolute joints and gear pairs for continuous rotation. Object geometry may be imported into the simulation tool from

the layout drawings and the designer specifies motion constraints. The software can then simulate the resulting motion, which may be displayed in animation showing possible interference, jamming, or loss of contact between meshing objects.

Crescent mechanism operation relies on the continuous rotation of a ring gear, which has internally cut teeth that mesh with the externally cut teeth on the idler. Ensuring proper operation of the gears is complicated by the fact that non-standard gear form was used to increase the capacity of the pump. A 2D mechanical motion simulation was generated during the design phase of the crescent mechanism to ensure that continuous meshing between ring gear and the idler gear is maintained, and that no interference, jamming, or loss of contact takes place during the pumping cycle. The simulation was generated using the Working Model 2D[®] dynamics software, (MSC

Software Corporation, Redwood, CA, USA). The mask patterns for the ring gear, the idler and the crescent were imported into a 2D macroscale simulation package from the POLY2 level of the respective items, and the appropriate motion constraints were added.

The simulated motion and the actual motion of the crescent mechanism are shown in Figure 9. The top part of the figure shows four frames of the generated motion clip. The frames depict the engagement-disengagement of one pair of teeth between the idler and the ring gear during operation, and are repeated for each pair of teeth engagement. At the design stage, this simulation verified continuous meshing between the ring gear and the idler with no interference or jamming. The simulated motion was found to be in good agreement with that of the actual fabricated pump shown in the bottom of Figure 9.

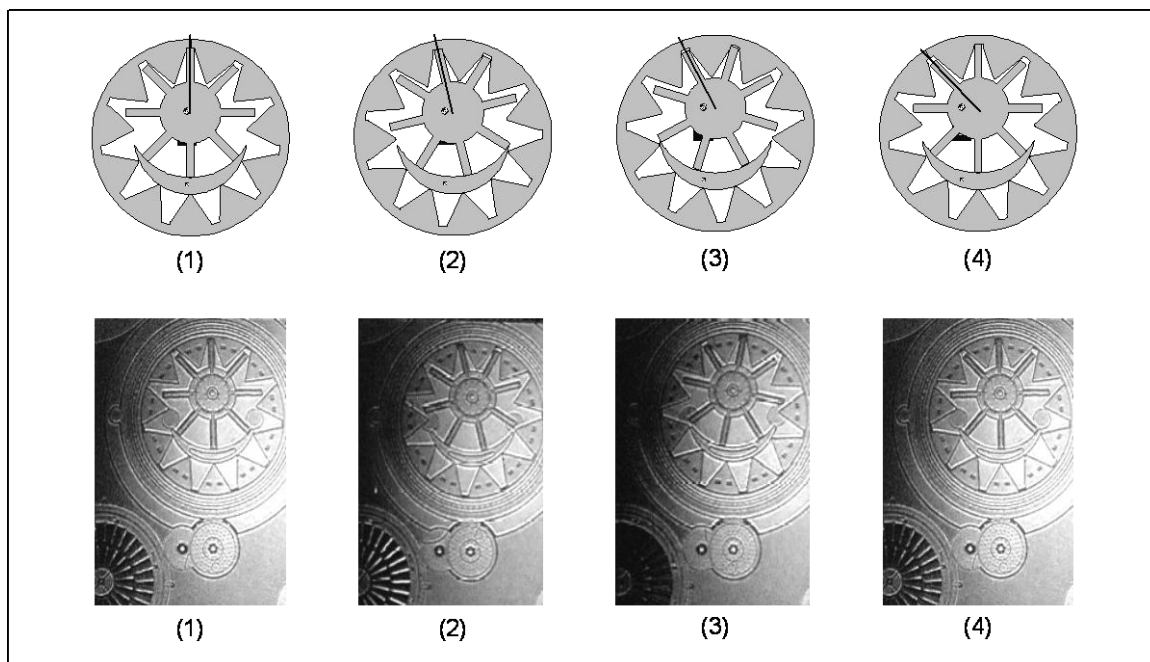


Figure 9. Crescent mechanism motion. Simulated (top) and actual (bottom)

2D motion simulation proved to be valuable in confirming the correct operation of the crescent pump mechanism. However, The POLY2 dimensions on which the simulation was based represent only the nominal dimensions of the crescent pump components, and the vertical topography resulting from additional SUMMiT layers were not included in the model. The cross section visualizer was used at different critical location on the mask layout to ensure that these artefacts cause no interference or jamming during actual motion. To show such effects, 3D motion simulation of surface micromachined mechanism is needed. This requires the integration between the 3D geometry modeller and the motion simulation routines and is not yet available.

Motion simulation confirms the kinematic correctness of the model, but does not include the dynamic effects of the forces and torques acting on the microstructure in operation. The software, for example would not calculate the forces acting on the components from the actuator

used, neither would it confirm that power available by the actuator is enough to overcome the friction forces resisting the motion. The designer must rely on his own judgment and experience in answering such questions. A physical model for the forces and torques developing during operation, which includes the forces of stiction, friction and surface tension, would help ensuring that the drivers used are adequate and would produce the intended motion of the designed mechanism.

7. Conclusions

The paper described the application of CAD tools used in the development of surface micromachined mechanism design and illustrated the utilization of these tools in the design of a crescent micropump mechanism. The potential benefits of parametric constraint-based CAD systems in surface micromachined mechanism design are discussed.

Construction and editing facilities provided by current layout CAD systems are convenient for producing the

lithographic masks of surface micromachined MEMS. Boolean operations may be used to expedite the layout process, and help in visualizing the result of using positive and negative lithographic masks in the design.

Parametric CAD systems allow imposing a set of constraints on the design, which may be derived from the mandatory or advisory rules of the fabrication process. This allows editing operation to be performed without running the risk of violating these rules. The explicit representation of design rules in parametric design systems leads to a more transparent form of knowledge representation, and allows for storing a deeper level of design expertise in library items.

Visualization tools help visualizing the target MEMS structure during the design stage, assuring the conformity of the mask to the intended process. Mechanical motion simulation tools may be adapted to micromechanism design to predict the kinematic behaviour of the mechanisms. A comprehensive surface micromachined design system requires integrating layout, visualization and motion simulation functions; a capability that may be provided by modern feature, based associative design systems. This would allow 3D motion simulation which considers vertical topography issues associated with the process artefacts. Additionally, these systems may provide a link to other downstream design activities including finite element analysis and rapid prototyping.

References

- [1] Kuehnel, W. and Sherman, S., "A surface micromachined silicon accelerometer with on-chip detection circuitry," *Sensors and Actuators A: Physical*, Volume 45, Issue 1, October 1994, 7-16
- [2] Yang, J., Jia, S. and Du Y., "Novel optical accelerometer based on Fresnel diffractive micro lens," *Sensors and Actuators A: Physical*, Volume 151, Issue 2, 29 April 2009, 133-140
- [3] Yang, J.P., Low, L.N. and Johnson, D., "A MEMS-based tracking milli-mirror for high-density optical disk drives," *Sensors and Actuators A: Physical* Volume 133, Issue 2, 12 Feb. 2007, 368-374
- [4] Barnes, S., Miller, S., Rodgers S., and Bistie F., "Torsional Ratcheting Actuating System," *Proc. of 3rd International Conference On Modelling and Simulation of Microsystems (MSM00)*, San Diego, CA, March 27-29, 2000, 273-276.
- [5] Kilani M. I., Galambos P. C., Haik Y. S., and Chen C-J., "Design and analysis of a surface micromachined spiral-channel viscous pump," *ASME Journal of Fluid Engineering*, Vol. 125, March 2003, 339-344.
- [6] Kilani M. I., Al-Halhouli A. T., Galambos P. C., Haik, Y. S. and Büttgenbach, S., "Development of a Surface Micromachined On-Chip Flat Disk Micropump," *Sensors and Transducers*, 107(8), 2009, 64-76
- [7] Al-Halhouli A. T., Kilani M. I., and Büttgenbach, S., "Development of a novel electromagnetic pump for biomedical applications," *Sensors and Actuators A: Phys.*, Feb. 2010
- [8] Al-Halhouli A. T., Kilani M. I. and Büttgenbach S., "Development of a Novel Meso-Scale Electromagnetic Pump for Biomedical Applications," *Procedia Chemistry*, 1(1), 2009, 349-352
- [9] Haik Y., Hendrix J., Galambos P. and Kilani, M. I., "Surface Micromachined Crescent Micropump," *Proceedings of the 7th International Symposium on Mechatronics and its Applications, ISMA '10*, April 20-22, 2010 Sharjah, United Arab Emirates
- [10] Bustillo, J. M., and Muller, R. S., "Surface micromachining for microelectro-mechanical systems", *Proc of the IEEE*, Vol.86, No.8, 1998, 1552-1573.
- [11] Kilani, M., "CAD in surface micromachined mechanisms design," *Proc. 11th Int. Conf. Machine Design and Production (UMTIK 2004)* 13-15 Oct. 2004, Antalya, Turkey.
- [12] Kilani, M., Galambos, P., Haik, Y., and Chen C-J., "University – National Laboratory Collaboration on MEMS Design Education," *Proceedings of the 2001 ASME IMECE*, November 2001, New York, NY.
- [13] Fan, L.-S., Tai, Y.-C., and Muller, R. S., "Pin joints, gears, springs, cranks, and other novel micromechanical structures," *Proc. 4th Int. Conf. Solid-State Sensors and Actuators (Transducers'87)*, Tokyo, Japan, June 2-5, 1987, 853-856.
- [14] Mehregany, M. and Tai, Y.-C., "Surface micromachined mechanisms and micromotors," *J. Micromech. Microeng.*, Vol.1, No.2, 1991, 73-853.
- [15] Sniegowski, J. J., and de Boer M. P., "IC-compatible polysilicon surface micromachining," *Annual Review of Materials Science*, Vol.30, 2000, 299-333.
- [16] Rodgers M. S., Sniegowski, J. J., Miller, S. L., and LaVigne, G., "Designing and Operating Electrostatically Driven Microengines," in *Proceedings of the 44th International Instrumentation Symposium*, Reno, NV, May 3-7, 1998, 56-65.
- [17] Polosky M. A., Plummer, D. W., Garcia, E. J., Shul, R. J., Holswade, S. C., Sullivan, C. T. and McBrayer J. D., "Surface micromachined components for a safety subsystem application," in *Proceedings of the International Symposium on Instrumentation in the Aerospace Industry*, 1999, 517-526.
- [18] Yarberr, V. C., "MEMS Design Rule Checking: a batch approach for remote operation," in *proceedings of the SPIE Smart Electronics and MEMS Conference*, San Diego, CA, 1998, 32-39.
- [19] Andrel, R. and Medgen, R., "Modelling with constraints: theoretical foundation and applications," *Computer Aided Design*, Vol.28, No.3, 1996, 155-168.
- [20] Haik, Y. S. and Kilani, M. I., *Essentials of Pro/Engineer*, CL-Engineering, 2001.
- [21] Yarberr, V. C. and Jorgensen, C. R., "A 2D Visualization Tool for SUMMiT V Designs," *Fourth International Conference on Modeling and Simulation of Microsystems*, Hilton Head, SC, 2001, 606-609.
- [22] Jorgensen, C. R. and Yarberr, V. C., "A 3D Geometry Modeler for the SUMMiT-V MEMS Designer," *Fourth International Conference on Modeling and Simulation of Microsystems*, Hilton Head, SC, 2001, 594-597.

Exploration Algorithm Technique for Multi-Robot Collaboration

Mohammad Al-Khawaldah^a, Omar Badran^b and Ibrahim Al-Adwan^a

^aDepartment of Mechatronics Engineering, Faculty of Engineering Technology, Al-Balqa` Applied University, Amman 11134- Jordan.

^bDepartment of Mechanical Engineering, Faculty of Engineering Technology, Al-Balqa` Applied University, Amman 11134- Jordan.

Abstract

This paper focuses on wall-following exploration algorithm using two cooperating mobile robots. The aim is to decrease the exploration time and energy consumption. The new technique is a combination of wall-following exploration algorithm and frontier-based exploration algorithm. The proposed algorithm is divided into two stages: Firstly, one of the robots follows (detects) the entire of the environment walls. And secondly, they employ frontier-based algorithm to complete exploring the remaining unexplored areas in the environment. During these two stages, the robots sweep the line-of-sight between them in each step to maximize the exploration efficiency. Numbers of simulation experiments are presented. Moreover, testing with real robots will be introduced. In these experiments, the negatives and shortcomings of this exploration algorithm will be overcome.

© 2011 Jordan Journal of Mechanical and Industrial Engineering. All rights reserved

Keywords: Robot, Exploration, Collaboration, Wall-following

1. Introduction

Exploration and mapping is an important issue in the robotics field. Its importance comes from the wide-range of beneficial applications such as path planning, search and rescue, accessing dangerous environments and cleaning. Many techniques were proposed to increase the exploration efficiency. Exploration efficiency depends on exploration time, energy consumption and exploration accuracy.

The two dimensional 2D environment is represented as occupancy grid map [1, 2]. Frontier-based exploration is proposed to minimize the overall exploration time by choosing appropriate target cell (frontier cells) for individual robots so that they explore different sections of the environment and the overlapping between them is minimized. The bidding function selects the cell with the maximum utility and the minimum cost with respect to each robot. A new different technique from those mentioned above was proposed by Ziparo *et al.* [3]. The goal is to reduce the size of the exploration area by using Radio Frequency Identification (RFID) tags as a coordination points between robots.

This paper focuses on testing the wall-following exploration algorithm through simulation and with real mobile robots. The aim is to assess the effectiveness of using the line-of-sight technique with grid-based maps to represent unknown environments in reality. Employing the line-of-sight technique to generate grid-based maps is innovative and it is the basis of the exploration algorithms proposed in this paper.

2. Wall-Following Exploration Algorithm Procedure

In this algorithm, the robots are directly guided to the environment walls to sweep cells as much as they can in each step. The new approach is an extension of the previous works [4-6]

The wall-following exploration algorithm can be briefly summarized as follows:

1. Call the two robots A & B. A is known as the "wall follower" and B as the "trouble shooter". Both of them start at one of the environment corners or walls.
2. The wall follower starts following the walls. During each step of its movement it sweeps the line-of-sight to the other robot. It can also potentially correct its location estimate by using the trouble shooter as an intelligent land mark. It continues following the walls until the line-of-sight between the two robots is lost. Then it moves one step back to regain the line-of-sight, and then it stops.
3. The trouble shooter starts moving toward the wall follower to discover the cause of the line-of-sight obstruction which would be either an obstacle or a wall. During this movement the line-of-sight would be available.
4. When the trouble shooter reaches the cause of the line-of sight blockage, it starts following the walls in a clockwise direction if the cause of obstruction is on its right hand side. On the other hand, if the cause of the obstruction is on its left hand side, it starts following the walls in a counter-clockwise direction. During the

trouble shooter wall following, if it meets its partner (the cause of line-of-sight obstruction in this case should be a wall) then the procedure goes to point number 2. Wall following by robot B (the trouble shooter) continues until the line-of-sight is lost again.

5. The trouble shooter moves one step back and regains the line-of-sight again.
6. The procedure points from 2-5 is repeated until the wall follower completes detection of all the environment walls.
7. The remained unexplored area is explored by using frontier-cells and line-of-sight. The robots' position estimates can also be corrected during this stage but it slows down the exploration to make the robots take turns to move.

3. Experimentation And Results

Webots® simulator is used for simulation and real world implementation. It allows testing the robot behavior in simulation before implementation in reality, in order to debug. This helps to fix problems that may appear, like code mistakes, during the simulation stage. After the robot's behavior is tested in simulation and all of the problems are solved then real exploration can be implemented.

To switch the control to real robots, there is an option in the Webots software to switch the control from virtual simulated robots to real robots. Once the control is switched to real robots, the real robots should behave the same as they behave in simulation.

In summary, the first step of real robots exploration with Webots® is to perform a simulation run then to switch the control to real robots.

3.1 Simulation

In the wall-following algorithm, the robots start at any point on an environment wall. The wall follower starts following the walls in a clockwise direction while the trouble-shooter watches it. The trouble shooter checks if it can see the wall follower in each step. If the trouble shooter can see the wall follower, all the cells between them are assigned as free. This method helps the robots to explore the free spaces in the environment quickly.

Three environments are tested with Webots simulator. These environments are shown in Figures 1 to 4. Figure 2 shows different exploration progressive snapshots for this environment.

The three environments in Figures (1, 3 and 4) are the same, but in Figures (3 & 4) the environment is partitioned (halved) in different ways to show how the generated maps are related to different environment sizes and shapes.

The results of these experiments are given below:
The environment shown in figure 1

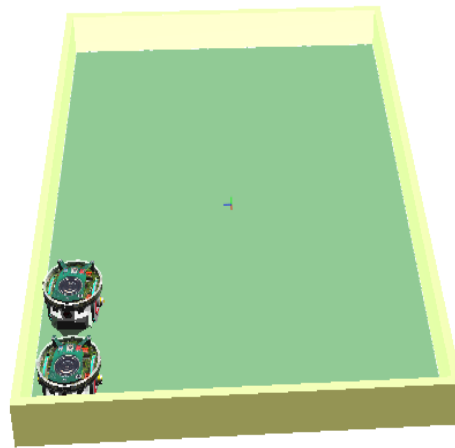
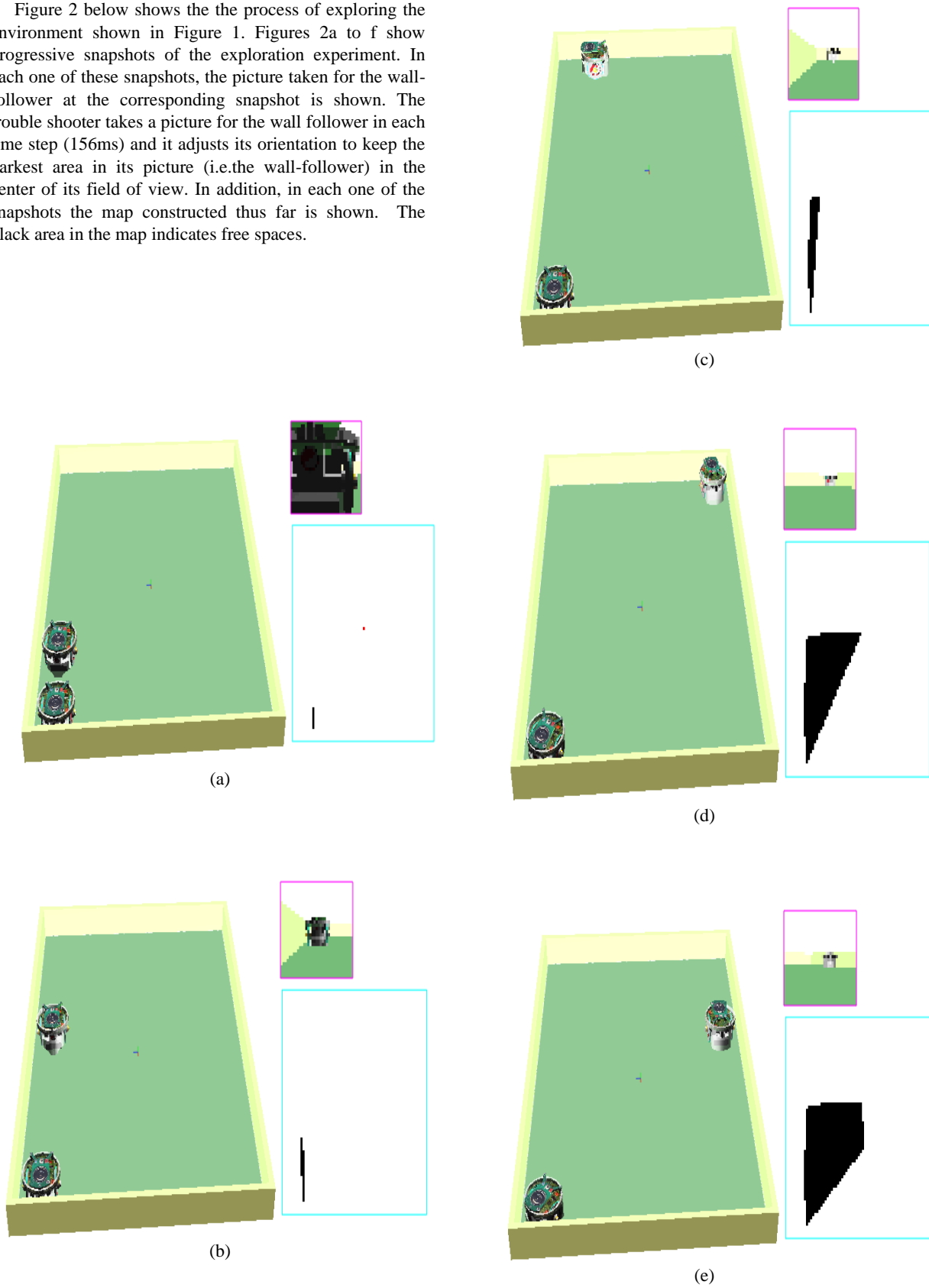


Figure 1: A rectangular environment to be explored by two Epuck robots with Wall-following exploration algorithm

The two Epuck robots start at the left bottom corner of the environment as shown in figure 1. The trouble shooter (the one very close to the corner) tries to keep looking at the wall follower while it is following the walls. If it can see the wall follower then there are no obstacles between the two robots and the area between them is assigned as free. In particular, the trouble shooter uses its camera to check if it can see the wall follower. The robots color is very dark compared to the environment (background) color. Therefore, when a picture is taken by the trouble shooter camera, this picture is checked for a dark area of higher intensity than the threshold. The threshold is chosen after an accurate calibration of the camera has been performed. Furthermore, when the trouble shooter finds a dark area in the picture, it adjusts its orientation to keep that dark area in the middle of the picture. This orientation adjustment is necessary to keep the wall follower in the field of view of the camera. As a result of the orientation adjustment, when the wall follower moves during the exploration, the trouble shooter keeps looking to it.

Figure 2 below shows the the process of exploring the environment shown in Figure 1. Figures 2a to f show progressive snapshots of the exploration experiment. In each one of these snapshots, the picture taken for the wall-follower at the corresponding snapshot is shown. The trouble shooter takes a picture for the wall follower in each time step (156ms) and it adjusts its orientation to keep the darkest area in its picture (i.e.the wall-follower) in the center of its field of view. In addition, in each one of the snapshots the map constructed thus far is shown. The black area in the map indicates free spaces.



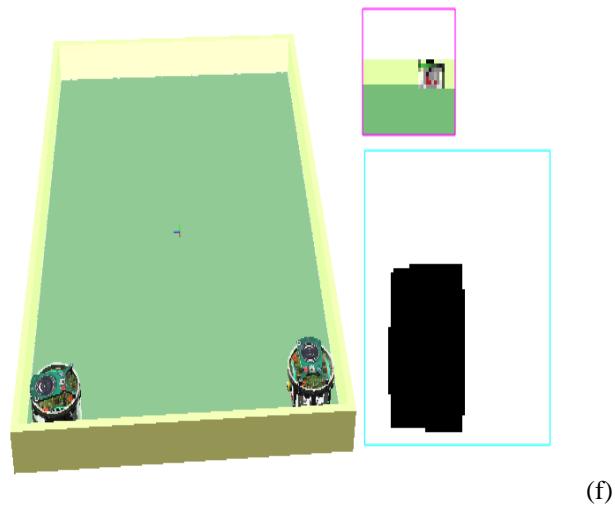


Figure 2: Wall-following exploration progressive snapshots with camera image and the constructed map thus far

Looking at the exploration snapshots in Figures 2a to f, it is clear that the trouble shooter adjusts its orientation to keep the wall follower in the centre of its field of view. The trouble shooter has to be fast enough to adjust its orientation to achieve that.

Figure 3 a shows a snapshot of the exploration when the wall follower is about to finish following the environment walls at a speed of 300cm/min. While Figure 3 b shows the generated map when robot's speed is 200cm/min

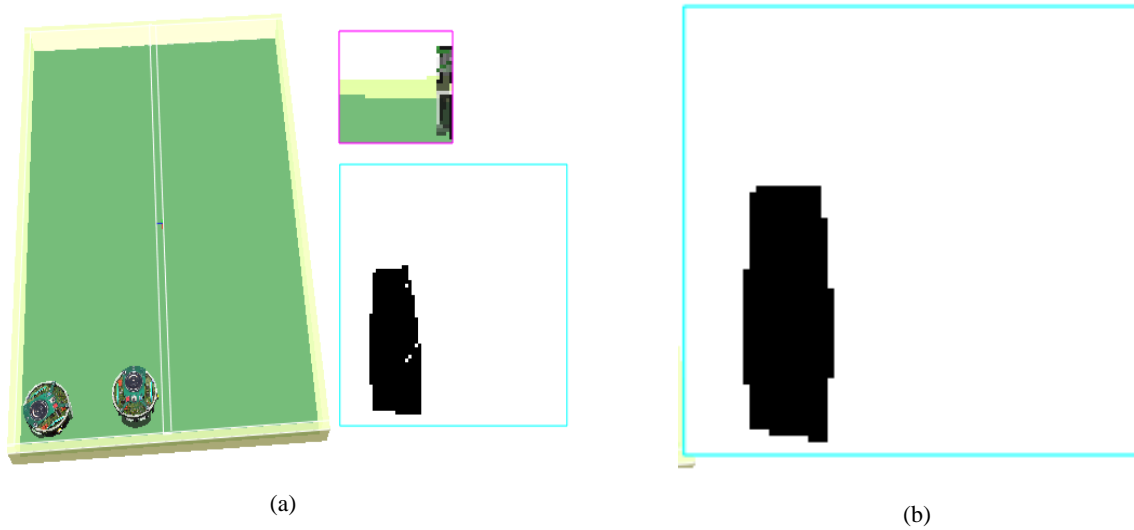


Figure 3: (a) Wall-following exploration experiment with camera image and constructed map thus far (robot speed is 300cm/minute), (b) Map generated at speed of 200cm/minute

The map shown in Figure 3 a shows that the robots missed few cells that have not been swept with line-of-sight. It seems that this is due to the fact that robots need to sweep the line-of-sight between them more frequently to reduce the probability of missing some cells. The other solution is to reduce the robot speed. Therefore, robots will continuously sweep the line-of-sight between them in shorter distances. Figure 3 b shows a map generated at 200cm/minute for the same environment. It is clear that the problem has been solved and there are no unexplored cells in the map.

Figure 4 shows a snapshot of the exploration when the wall follower is about to finish following the environment walls.

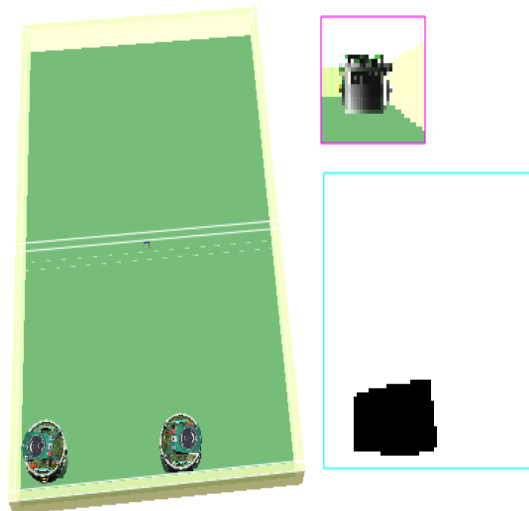


Figure 4: Wall-following exploration experiment with camera image and the constructed map thus far

The system is checked with different environments to check its ability to cope with different environments configurations. After the successful Webots® simulation runs of wall-following exploration, the system is now ready for testing with real robots.

3.2 Real Robots Exploration

Number of exploration experiments with real robots are presented. Following are some environments and their generated maps. As before, the black area in the maps represents the free space in the environment.

Figure 5a shows a sketch of the real-environment boundaries, and Figure 5b shows the generated map of the environment.

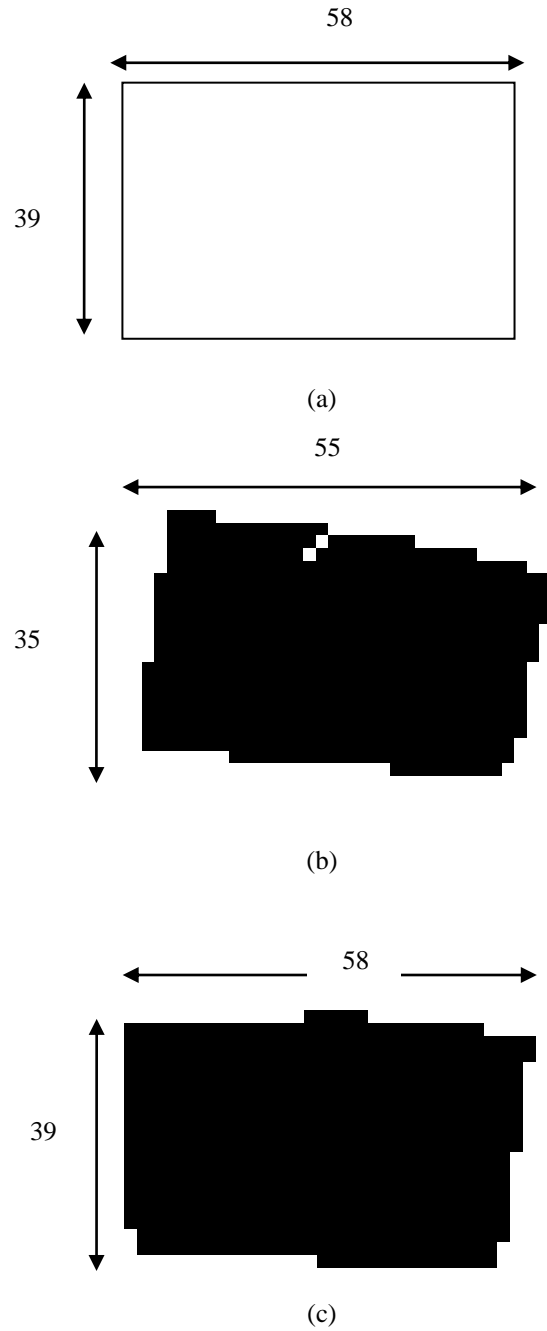
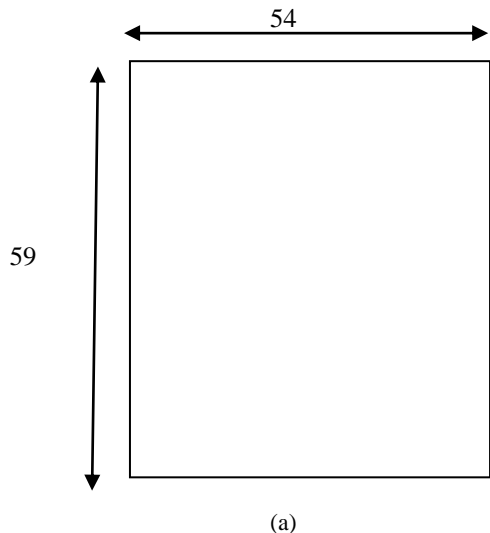


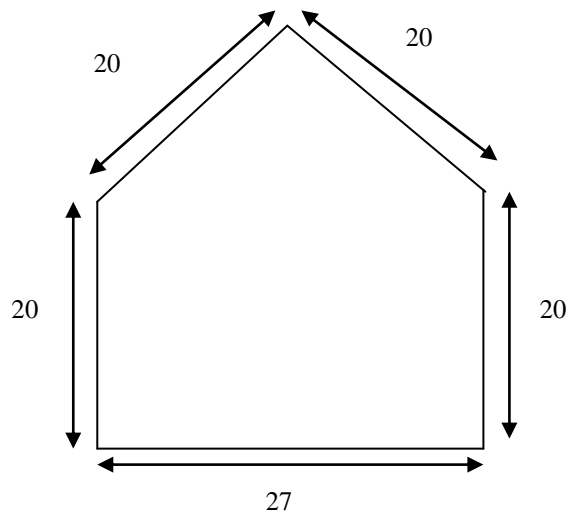
Figure 5: Exploration with real robots. Environment of 37-by-58 cm. (a) is the environment to be explored, (b) is the environment map generated at speed of 300 cm/min, (c) is the environment map generated at speed of 200 cm/minute. The dimensions shown are in centimeters.

In the map shown in Figure 5b, it is clear that the robots missed two cells that have not been swept with line-of-sight. As before, this appears to be due to the fact that robots need to sweep the line-of-sight between them more frequently in order to reduce the probability of missing some cells. The other solution is to reduce the speed. Figure 5c shows a new map for the same environment generated at a speed of 200cm/min.

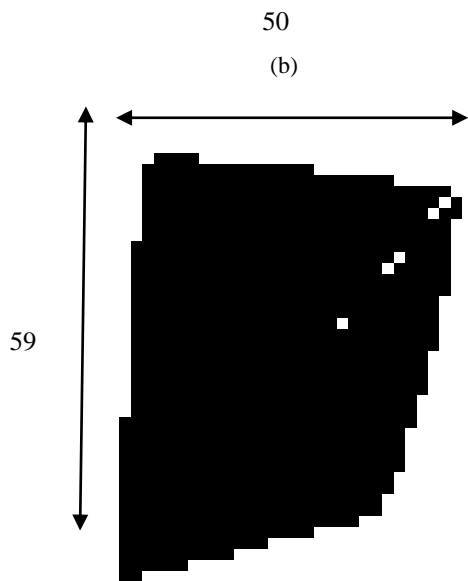
Figure 6a shows a sketch of the real-environment boundaries, and Figure 6b shows the generated map of the environment.



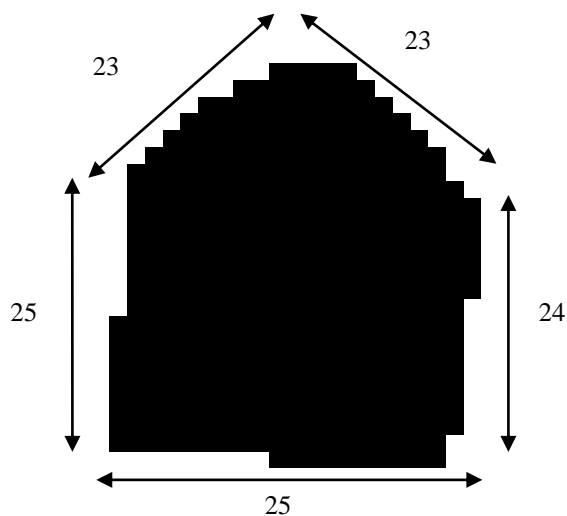
(a)



(a)



(b)



(b)

Figure 6: Exploration with real robots. Environment of 59-by-50 cm. (a) is the environment to be explored, (b) is the environment map generated at speed of 300 cm/min. The dimensions shown are in centimeters.

Figure 7: Exploration with real robots. (a) is the environment to be explored, (b) is the generated map. The dimensions shown are in centimeters.

Figure 7a shows a sketch of the real-environment boundaries, and Figure 7b shows the generated map of the environment.

Figure 8a shows a sketch of the real-environment boundaries, and Figure 8b shows the generated map for the environment.

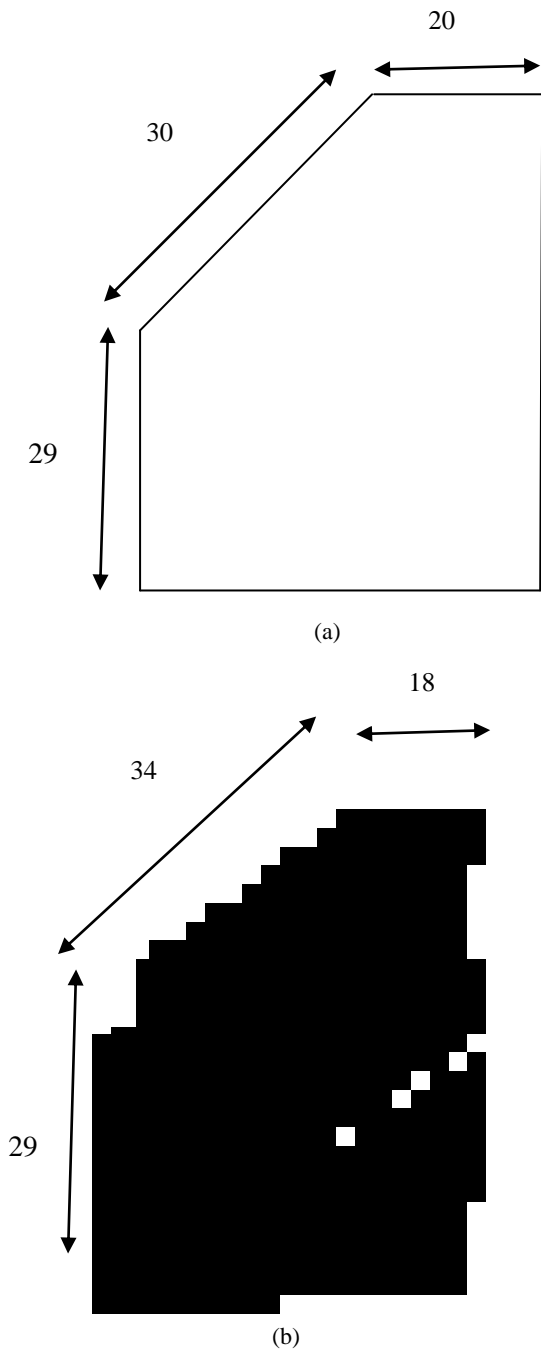


Figure 8: Exploration with real robots. (a) is the environment to be explored, (b) is the generated map. The shown dimensions are in centimeters

Figure 9a shows a sketch of the real-environment boundaries, and Figure 9b shows the generated map for the environment.

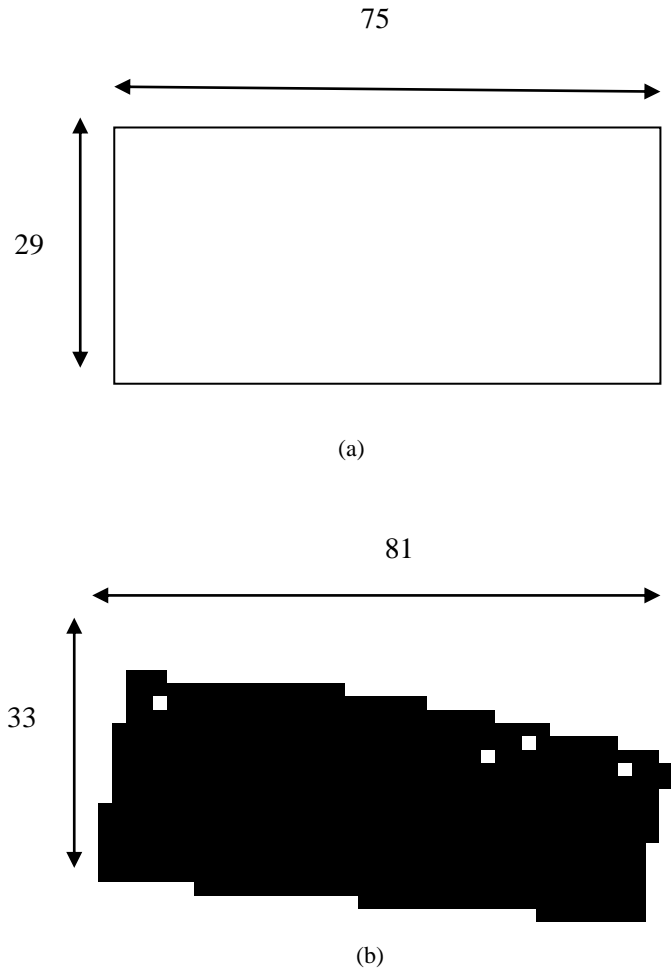


Figure 9: Exploration with real robots. (a) is the environment to be explored, (b) is the generated map. The dimensions shown are in centimeters.

The difference between the real environments and their maps is due to the localization problem. During the exploration, robots are not localized precisely. They depend on odometry to localize themselves. Therefore, the errors in position estimates are accumulated during the exploration.

4. Conclusions

In this research the exploration experiments with real robots have been successfully implemented to verify the robot behavior using the line-of-sight technique with grid-based maps. The results were very promising. The proposed wall-following algorithm has been successfully implemented in reality to produce representative maps for the real environment. Wall-following exploration algorithm dependency on accurate robots positions is less than other exploration algorithms.

References

- [1] Burgard, W., Moors, M., Stachniss, C. and Schneider, F.E. "Coordinated multi-robot exploration", *IEEE Trans. Robot. Autom.* (2005), 21(3), pp. 376-386
- [2] Sheng, W., Yang, Q. and Tan, J, Xi,. "Distributed multi-robot coordination in area exploration", *Robot. Auto. Syst.* (2006), 54(12), 945-955
- [3] Ziparo, V.A., Kleiner, A., Nebel, B. and Nardi, D. "RFID-based exploration for large robot teams", In: *Proc. of the IEEE Int. Conf. on Robotics and Automation* (2007), 4606-4613. IEEE, Roma.
- [4] Rekleitis, I., V. Lee-Shue, A.P. New and H. Choset "Limited Communication, Multi-Robot Team Based Coverage", *IEEE International Conference On Robotics And Automation.* (2004)
- [5] Rekleitis, I., G. Dudek and E. Milios "Multi-robot collaboration for robust exploration", *Annals of Mathematics and Artificial Intelligence*, (2001), 31(1): p. 7-40.
- [6] Rekleitis, I.M., G. Dudek and E.E. Milios "On multiagent exploration", *Visual Interface* (1998), p. 455-461.

A Hybrid Power-plant System To Reduce Carbon Emissions

Munzer S. Y. Ebaid^a, Mohamad Y. Mustafa^b

^a ASME, SAE, Amman – Jordan, ^b Amman – JORDAN

Abstract

Emissions of CO and CO₂ are understood to be the main cause of global warming, melting of glaciers, heavy rain fall in some areas resulting in catastrophic floods and severe draughts in others. Introduction of national quotas is a political solution to limit carbon emissions; however, it cannot provide answers to the complex problem of climatic change. A permanent solution would require combustion free technologies for converting the chemical energy of fuels directly into electricity. In this respect, devices such as fuel cells are highly efficient direct energy conversion devices which have the true potential to reduce carbon emissions. This paper describes a conceptual hybrid power plant comprising a solid oxide fuel cell (SOFC) and a closed cycle gas turbine. A simple analysis of the plant has been carried out to demonstrate that significant gains can be made in reducing carbon emissions, increasing energy utilisation efficiency and minimising the impact of thermal loading on the environment.

© 2011 Jordan Journal of Mechanical and Industrial Engineering. All rights reserved

Keywords: Fuel Cell, Combined power plant, Hydrogen energy, Energy conservation, Protection of the environment.

Nomenclature

<i>SOFC</i>	Solid oxide fuel cell
C_p	Specific heat at constant pressure
γ	Ratio of specific heat
\dot{m}	Mass flow rate
R	Universal gas constant, <u>Electrical resistance</u>
E	Potential energy
w	Specific work output
W	Work output
P	Pressure
T	Temperature
Q_r	Heat rejected
Q_a	Heat added
ε_{HE}	Effectiveness of the heat exchanger
η	Efficiency, <u>Overvoltage</u>
i	Current density
F	Faraday's constant
α	<i>Charge transfer coefficient</i>
n	<i>Number of transferred electrons per mole</i>

Subscripts

1	Compressor inlet
2	Compressor exit

3	Nozzle inlet
4	Nozzle exit
o	Stagnation, exchange current density
a	Air
c	Compressor, cathode, cell
j	Jet
<i>FCGT</i>	Combined fuel cell-gas turbine
<i>FC</i>	Fuel cell
<i>HE</i>	Heat Exchanger
<i>overall</i>	Over-all (Efficiency)
<i>pt</i>	Power turbine
<i>gt</i>	Gas turbine
<i>act</i>	Activation
<i>con</i>	Concentration
<i>ohmic</i>	Ohmic
<i>int</i>	Internal currents
H_2	Denotes partial pressure for Hydrogen
O_2	Denotes partial pressure for Oxygen

1. Introduction

Global public concern about the impact of the emissions of combustion gases on the environment is growing sharply as a consequence of disastrous flooding in various parts of the world. Hence, national quotas are being introduced for the emissions of carbon based combustion gases (CO and CO₂) as a political solution for a complex technical problem.

The permanent solution of the problems of energy conservation and protection of the environment would be

* Corresponding author. siva_appisetty1@yahoo.co.in

the fuel cell; a highly efficient device that can convert the chemical energy of the fuel directly into electricity. However, as fuel cells of various types are under development to make them commercially viable, alternative solutions are needed in the short and the mid term to meet the ever increasing demand for clean energy.

Fuel cells and hybrid systems have emerged as advanced thermodynamic systems with great promise in achieving high energy/power efficiency with reduced environmental loads. In particular, due to the synergistic effect of using integrated solid oxide fuel cell (SOFC) and classical thermodynamic cycle technologies, the efficiency of the integrated system can be significantly improved (Zhang, Chan et al. 2010).

On account of the many advantages offered by the hybrid SOFC system, it is considered to be a key technology in improving power generation efficiency and reducing harmful emissions. First, there are no moving components in the fuel cell (except for balance of plant (BoP) components). Noise and vibrations associated with mechanical motion during operation are practically non-existent. This makes it possible to install the system in urban or suburban areas as a distributed power generation plant. Without moving parts, we would expect enhanced reliability and lower maintenance cost. Secondly, SOFCs (by virtue of high-temperature operation) can extract hydrogen from a variety of fuels. SOFC is the most sulfur-resistant (such as H_2S and COS) fuel cell. It can tolerate sulfur-containing compounds at concentrations higher than other types of fuel cells. In addition, it is not poisoned by carbon monoxide (CO); in fact, CO can be used as a fuel (Zhang, Chan et al. 2010).

Recently there have been various efforts to design and analyse the performance of pressurized SOFC hybrid systems considering various parameters and configurations. Park et al. (Park, Oh et al. 2007) simulated the design of a pressurized SOFC hybrid system using an existing (fixed) gas turbine and provided useful fundamental design characteristics as well as potential critical problems. Marko Santin et al. (Santin, Traversoa et al. 2009) presented a study of SOFC-GT hybrids for operation with liquid fuels. Thermodynamic and investment analysis performances were calculated based on zero-dimensional component models. The economic assessment was performed with a through-life cost analysis approach.

Bhinder et al (Bhinder, Ebaid et al. 2006) presented a parametric study of the fuel cell-gas turbine combined cycle power plant. They concluded that even when using a conservative figure of 55% for the fuel cell efficiency, the overall efficiency can be increased to approximately 65%; this increase in energy efficiency offers a solution to the two serious problems facing the power generation industry.

Calise et al (Calise, Accadia et al. 2007) presented an optimization method of a hybrid solid oxide fuel cell-gas turbine (SOFC-GT) power plant. The plant layout was based on an internal reforming SOFC stack; it also consisted of a radial gas turbine, centrifugal compressors and plate-fin heat exchangers. The results of their study showed that the design of a hybrid SOFC-GT power plant must focus on all its components, paying special attention to their coupling.

In the present work; a parametric study has been carried out to investigate the influence of the principal design variables of a hybrid power plant on its overall performance, in particular reduction of carbon based emissions (CO and CO_2), increase in energy utilisation efficiency and the impact of thermal loading on the environment. The plant comprises a closed cycle gas turbine and a high temperature fuel cell. This type of fuel cell is well developed and many plants have already been built around the world to meet the commercial and technical criteria (Zhang, Chan et al. 2010).

As the world is facing the challenges of rapidly depleting global reserves of fossil fuels and increasing impact of carbon based combustion gases on the environment, the paper should be of considerable interest to the Energy Industry and should lead to a stimulating discussion.

2. Theoretical Background of the Fuel Cell-Turbomachinery Propulsion Engine

A combined cycle power plant comprising a solid oxide fuel cell and a closed cycle gas turbine is shown in Figure 1. As the operating temperature of this type of fuel cell lies in the range from $800\text{ }^\circ\text{C}$ to $1000\text{ }^\circ\text{C}$, it must be cooled in order to protect it from structural failure. On the other hand, low grade heat must be extracted from the hot air coming out from the gas turbine before it enters the compressor. This cooling is achieved with the help of a regenerative heat exchanger. Cooling the air before it enters the compressor reduces compression work; thereby improves the plant efficiency further with only a marginal increase in capital cost. The main feature of the proposed combined cycle plant is that it does not rely on burning the hydrocarbon fuel in order to use its chemical energy to generate electricity. Therefore, the combustion chamber of the gas turbine can be replaced by a heat exchanger to remove heat coming from the fuel cell and transfer it to the pressurised air that drives the closed cycle gas turbine. The aim of this paper is to show that the proposed hybrid plant can achieve:

- i. Substantial increase in the overall energy utilisation efficiency.
- ii. Reduction in emissions of CO and CO_2 .
- iii. Significant drop in thermal loading on the environment.

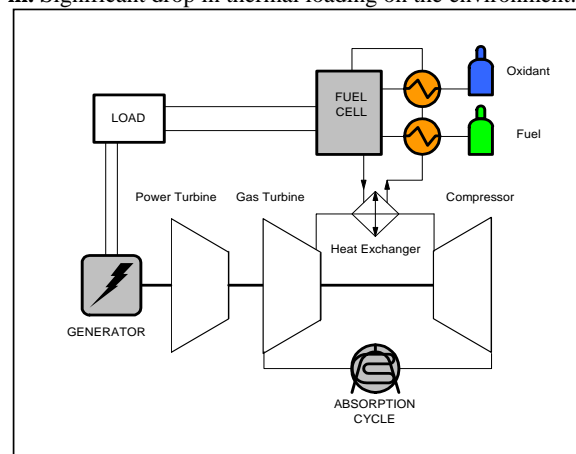


Figure 1. A Schematic Diagram of Hybrid Power Plant

3. The Solid Oxide Fuel Cell (SOFC)

Fuel cells are highly efficient electrochemical energy conversion devices that use the chemical energy of fuels to generate electricity. There are several types of fuel cells; in general, they all comprise four functional components: the anode, the cathode, the electrolyte and two chambers, one on each side, that allow the flows of fuel and oxidant. Since none of these components has any moving parts; fuel cells are simpler and quieter power generators than other devices such as steam turbines, gas turbines, reciprocating and rotary engines.

The type of fuel cell under consideration is the Solid Oxide Fuel Cell which is shown schematically in Fig. 2. It operates at temperatures ranging from 800 °C to 1000 °C and offers many advantages such as:

1. The kinetics of the chemical reaction are improved due to the high temperatures, hence precious metal catalyst are not needed, which means a considerable reduction in fuel cell cost.
2. Pressurising the fuel cell does not have much significant effect on performance.
3. Both hydrogen and carbon monoxide can be used as fuels in the SOFC.
4. The anode of the SOFC is usually a zirconia cermet (ceramic and metal); the metallic component is nickel. Due to high conductivity and stability of nickel under chemically reducing conditions, it can be used as an internal reforming catalyst. This characteristic allows internal reforming in the SOFC directly on the anode.
5. The high operating temperature of the cell implies that the heat emitted is good grade thermal energy that can be used in the fuel cell-gas turbine or steam turbine combined cycle (Zhang, Chan et al. 2010).

The primary fuel for fuel cells is hydrogen; a light and combustible gas which is present in water, hydrocarbon fuels and bio fuels. Hydrogen may be derived from water with the help of electrolysis and from hydro carbon and bio fuels by reforming or thermal cracking. In the case of a solid oxide fuel cell; reforming can be performed internally because of its high operating temperatures. Heat rejected by the fuel cell can be used in the closed cycle gas turbine to generate additional electricity.

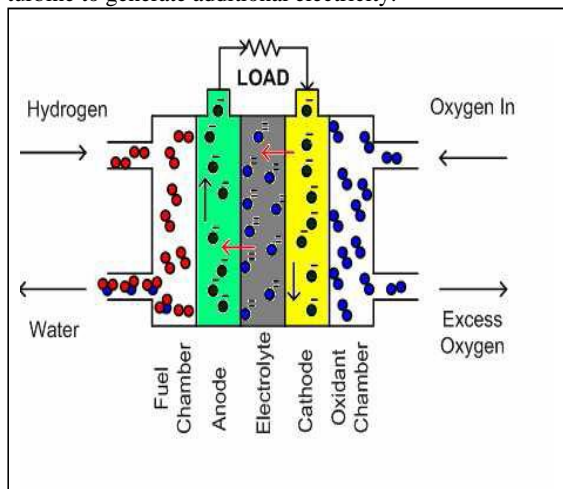


Figure 1. A schematic diagram of a single solid oxide fuel cell (not to scale).

The outputs of a High-Temperature Fuel Cell can be identified as follows:

1. Electric Power.
2. Heat Energy.
3. Hot gas emissions coming out of the electrode compartments as unused fuel and oxidant (air is used as an oxidant; so most of this gas will be Nitrogen with small amounts of Oxygen); in addition to water emissions which come out as superheated steam.

The performance of a fuel cell is given usually by the Current Density vs. Voltage curve, known as the polarisation curve shown in Fig. 3. The theoretical curve, which represents open circuit voltage, is a straight line parallel to the X-axis. The difference between the actual curve and the theoretical curve is due to four main sources of losses defined as follows:

4. Activation loss

Activation losses are caused by the slowness of the reaction taking place on the surface of the electrodes. A proportion of the voltage generated is lost in driving the chemical reaction that transfers the electrons to and from the electrode (J. Larminie 2003).

$$\eta_{act} = b \log \left(\frac{i_c}{i_o} \right) \quad (1)$$

Where:

$$b = -\frac{RT}{\alpha nF} \alpha \quad (2)$$

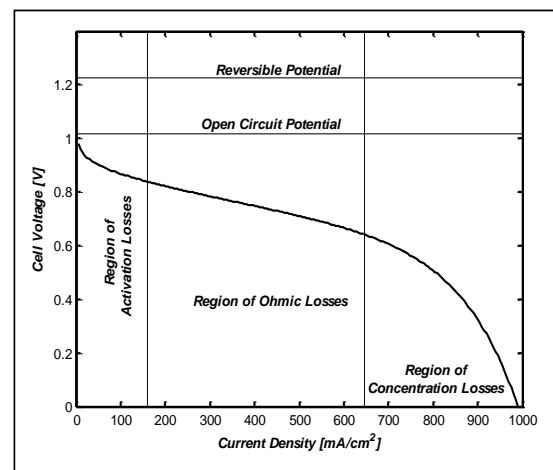


Figure 2. Typical power density and voltage versus current density curves

5. Ohmic loss

Ohmic losses are sometimes called "resistive losses", as they stem from the straightforward resistance to the flow of electrons in the various fuel cell components, as well as the resistance to the flow of ions in the electrolyte. This voltage drop is approximately linear and proportional to current density. Mathematically, the Ohmic resistance can be represented as (Mustafa 2009):

$$\eta_{ohmic} = R_i i \quad (3)$$

Where ' R_i ' is the internal current resistance which comprises both electronic and protonic resistances caused by membrane and contact losses

6. Concentration loss

Concentration overvoltage or Mass transport losses result from the change in the concentration of one of the reactants at the surfaces of the electrolyte, which occurs when a chemical species participating in the reaction is in short supply due to obstruction in the pathway of this species. This type of loss is sometimes called "Nernstian" because of its connection with concentration effects which are modelled by the Nernst equation; the expression for this loss is given as follows (Mustafa 2009):

$$\eta_{con} = -\frac{RT}{nF} \ln \left\{ 1 - \frac{i}{i_l} \right\} \quad (4)$$

Where ' n ' is the number of electrons transferred per molecule in the reaction (in the case of Hydrogen-Oxygen Fuel cell $n = 2$ for Hydrogen, and $n = 4$ for Oxygen), ' R ' is the universal gas constant (8.314 KJ/kmol .K), ' T ' is the temperature of operation in Kelvin, and ' F ' is Faraday's constant.

7. Fuel Cross-Over and Internal Currents

Although the proton exchange membrane in the fuel cell is an electronic insulator, it will support very small amounts of electron cross-over. It will also allow some hydrogen to pass through diffusion from the anode to the cathode. This hydrogen will react with oxygen at the cathode in the presence of the catalyst to produce water and heat, but without producing electric current.

It is assumed here that the internal currents are equal to fuel cross-over. An empirical value for the internal currents suggested by (J. Larminie 2003) is (3.00 mA/cm²). Substituting this value in equation (4) above, gives a value of fuel consumption due to fuel crossover equal to: (0.314 × 10⁻¹⁰ kg/s.cm²) of hydrogen.

The value of the internal current has to be added to the fuel cell current when measuring fuel cell performance.

The total output voltage of a fuel cell, taking these losses into account, is given by the following expression:

$$V = E + (\mathcal{G}_{act+int} + \mathcal{G}_{ohmic+int} + \mathcal{G}_{con+int}) \quad (5)$$

Where:

$$E = 1.229 - \beta_2 (T - T^o) + \varphi T \left\{ \ln(P_{H_2}^*) + \frac{1}{2} \ln(P_{O_2}^*) \right\}$$

This expression represents the *thermodynamic potential for a hydrogen/oxygen fuel cell on the basis of the Nernst equation* where the values of the constant terms $\beta_2 = 0.85 \times 10^{-3} [VK^{-1}]$ and $\varphi = 4.3085 \times 10^{-5} [VK^{-1}]$. And P^* is the partial pressures of the reactant gases denoted by the respective subscript, ' T^o ' is the standard state temperature (298.15 K).

Fuel cell voltage is plotted against the fuel cell current for various values of temperature in accordance with equation (5), the oxygen partial pressure ($P_{O_2}^*$) is considered constant at 1 atm. Different current densities [A] are plotted on the same graph to get an idea about the effect of this parameter on the fuel cell voltage under different operating temperatures.

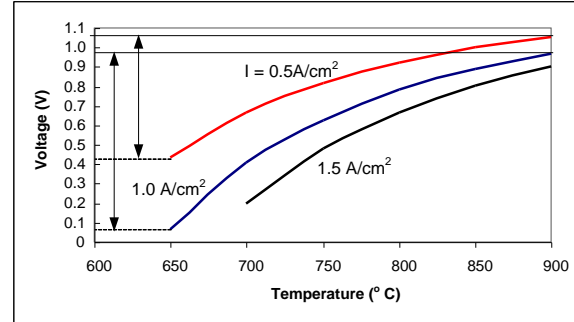


Figure 3. The effect of temperature on cell voltage

The effect of temperature on cell voltage [V] is obvious from the graph. It is noted that the influence of temperature is more prominent at higher current densities, however at temperatures higher than 750 °C the effect of temperature becomes small as can be seen from the graph.

8. Efficiency of the Fuel Cell

The current generated by a fuel cell that uses hydrocarbon fuel depends on the number of electrons contained in a given mass of that fuel. Current is the rate of flow of charge.

The current generated by \dot{m}_f (moles of fuel) can be written as follows: Since one mole of electrons contains the number of coulombs given by Faradays constant; definition of current is in coulombs/s, then:

$$I = \frac{\dot{m}_f}{M_f} nF \quad (6)$$

Where M_f is the molecular weight of the fuel (kg-mole); I is the fuel cell current (Amp) and $F = 96495$ is the Faraday constant (C/mol).

The electrical power output ζ_e of the fuel cell can be written as follows:

$$\zeta_e = \frac{\dot{m}_f}{M_f} nF \times V \quad (7)$$

In this expression n is the number of hydrogen atoms in a molecule of the fuel.

The electrical efficiency of the cell is given by the following expression:

$$\varepsilon_{fc} = \frac{\text{Electrical Power Output}}{\text{Rate of Energy Available}} \quad (8)$$

$$\varepsilon_{fc} = \frac{V_{cell} \times 2F}{M_{H_2} \times \text{Calorific value (HCV)}} \times 100\% \quad (9)$$

Where $V = E + (\mathcal{G}_{act+int} + \mathcal{G}_{ohmic+int} + \mathcal{G}_{con+int})$, HCV is the higher calorific value of the fuel used in the fuel cell, typically hydrogen. Substituting the values for Faraday's constant, molar mass of hydrogen and the interpolated calorific value for hydrogen, the efficiency of the fuel cell becomes:

$$\varepsilon_{fc} = \frac{V_{cell}}{1.38} \times 100\% \quad (10)$$

Following the same lines, the electrical efficiency is the ratio of measured electrical output to actual electrical input, which can be written as:

$$\varepsilon_e = \frac{iV_{cell}}{(i + i_{int})E^o} \quad (11)$$

Where ' i ' is the current density, ' i_{int} ' is the cross over current which is assumed to be equivalent to internal currents; both are considered as currents defining the input power together with the theoretical reversible voltage of the fuel cell. From equations (6 - 11) and the definition of maximum thermal efficiency, the efficiency of the fuel cell becomes:

$$\varepsilon = \frac{0.87 \times iV_{cell}}{(i + i_{int})E^o} \quad (12)$$

Calculated Efficiency vs. Power Output for one MW fuel cell is plotted in Fig. 5 based on equation (12). The relationship with T is embedded in the expression for the standard cell voltage E^o .

It should be noted from the graph that a very attractive feature of the fuel cell is that its part load performance is superior compared with combustion engines. This can be seen from the rising efficiency curve as power output is reduced. IN the case of combustion engines, the efficiency increases as temperature increases, which clearly indicates the dependence of efficiency on temperature.

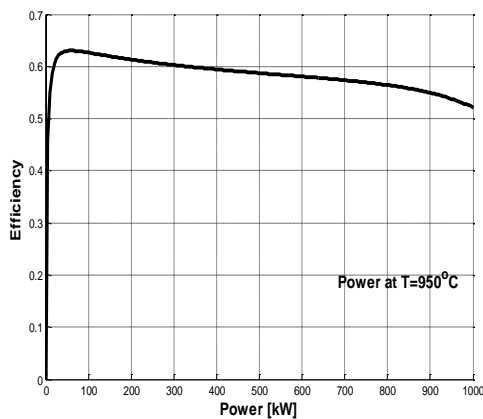


Figure 4. Fuel cell efficiency vs. power output

9. Efficiency vs. Fuel Type

The ratio of the mass of hydrogen and the total mass of a specific fuel depends on the chemical formula of the fuel

($C_m H_n$) where m and n are constants for a hydrogen fuel. Since hydrogen is very light compared with carbon, the ratio decreases as carbon atoms increases, hence electrons which can be separated from hydrogen decrease. Since flow of electrons is the source of flow of electrical energy, the available electrical energy compared with thermal energy (i.e. calorific value) reduces. The effect of this ratio on the efficiency of the fuel cell is shown in Fig. 6 which is plotted on the bases of equation (9) and the calorific values of the relevant fuels from standard tables of material properties.

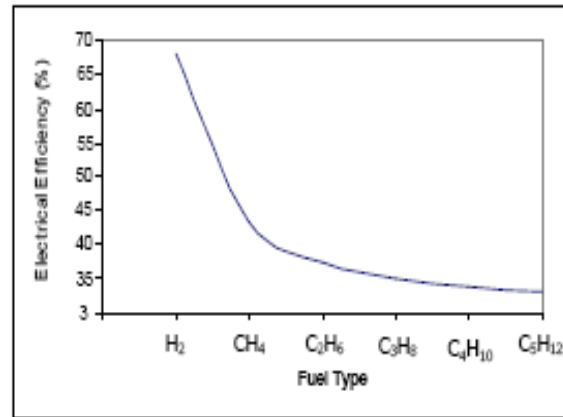


Figure 5. The effect of fuels on the efficiency of the fuel cell

10. Closed Cycle Gas Turbine

The gas turbine cycle is shown on T-S diagram, Fig. 7. Air at Temperature T_{01} and pressure P_{01} the working fluid is compressed by the compressor to pressure P_{02} ; the corresponding temperature of air is T_{02} . While flowing through the heat exchanger air is heated to Temperature T_{03} . From point 3, compressed hot air expands through the gasifier turbine to point 4 while its pressure and temperature drop to P_{04} and T_{04} respectively. Hot gasifier turbine exhaust flows through the free power turbine down to P_{05} and T_{05} , point 5.

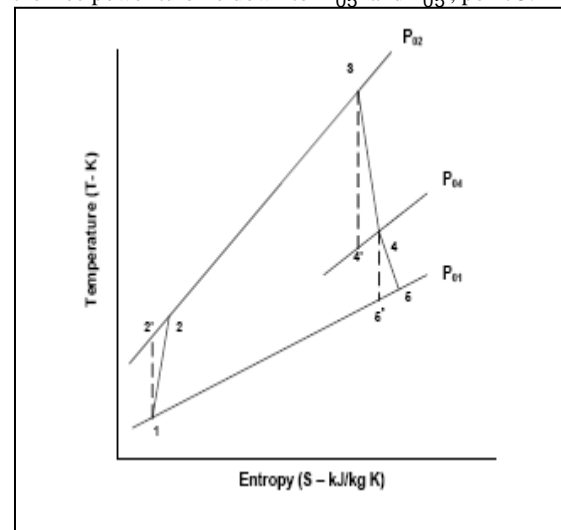


Figure 6. T-S Diagram of the gas turbine cycle

In order to calculate the shaft work produced by the free power turbine, it is necessary to carry out

thermodynamic analysis of the cycle. The analysis is based on the assumptions that ($C_p = \text{constant}$) over the range of temperatures considered and pressure drop from point 2 to point 3, is negligible. Thus

expansion ratio across the free power turbine (P_{04}/P_{05}) can be written in terms of cycle pressure ratio, maximum to minimum temperature ratio and isentropic efficiencies of the gasifier compressor and turbine. The final expression (P_{04}/P_{05}) is given below:

$$\frac{P_{04}}{P_{05}} = \frac{P_{02}}{P_{01}} \left\{ 1 - \frac{\left(\frac{P_{02}}{P_{01}} \right)^{\frac{\gamma-1}{\gamma}} - 1}{\frac{T_{03}}{T_{01}} \eta_c \eta_t} \right\}^{\frac{\gamma}{\gamma-1}} \quad (13)$$

Finally the specific work output (i.e. work output per unit mass of air) of the free power turbine as a function of the expansion ratio is given by the following expression:

$$\frac{w}{m} = \eta_t c_p T_{04} \left\{ 1 - \left(\frac{P_{04}}{P_{05}} \right)^{-\left(\frac{\gamma-1}{\gamma} \right)} \right\} \quad (14)$$

From equations (13) and (14) an expression for specific work output can be written as:

$$\text{Specific work} = C_p T_{01} \left[\eta_t \frac{T_{03}}{T_{01}} \left(1 - \left(\frac{P_{01}}{P_{02}} \right)^{\frac{\gamma-1}{\gamma}} \right) - \frac{1}{\eta_c} \left(\left(\frac{P_{02}}{P_{01}} \right)^{\frac{\gamma-1}{\gamma}} - 1 \right) \right] \quad (15)$$

The thermal efficiency of the system can be defined in the substituting for the thermal efficiency from the following equation involving the air to fuel ratio (A/F) as follows:

$$\eta_{th} = \frac{(A/F) C_p \Delta T_{02-03}}{C.V.} \quad (16)$$

This equation can be used to find a relationship between turbine inlet temperature and compressor inlet temperature in terms of air to fuel ratio as follows:

$$\frac{T_{03}}{T_{01}} = \frac{C.V.}{(A/F) C_p T_{01}} + \frac{1}{\eta_c} \left\{ \left(\frac{P_{02}}{P_{01}} \right)^{\frac{\gamma-1}{\gamma}} - 1 \right\} + 1 \quad (17)$$

Substituting the temperature ratios in the equation for specific work output (15) a graph for Specific work output vs. compression ratio can be plotted. The result is given in Fig. 8 which it shows that for maximum specific work output, the cycle pressure ratio higher than 13:1 is needed. At this pressure ratio and Air/Fuel ratio (A/F) of 55 the specific work output is approximately 175 kJ/kg.

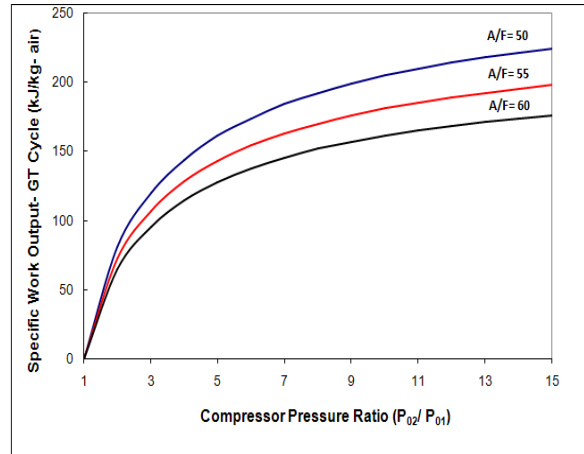


Figure 7. Specific Work Output vs. Cycle Pressure Ratio proposed

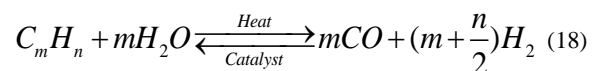
11. The combined cycle hybrid plant

The proposed hybrid plant was shown diagrammatically in Fig. 1 and it was claimed that carbon emissions could be reduced significantly by combining a solid oxide fuel cell and a closed cycle gas turbine (Kuchonthara, Bhattacharya et al. 2003). In addition the proposed hybrid plant would also achieve higher energy utilisation efficiency and minimise the impact of thermal loading on the environment. Those claims have been quantified by calculations.

12. Flow of mass and heat in an internally reformed SOFC

So as to derive a relationship to relate the work output of the power turbine to the fuel input of the fuel cell, the fuel cell- reformer arrangement is considered. The following reactions take place in the reformer-fuel cell system; this is tackled in a general form below and is applicable to any hydrocarbon.

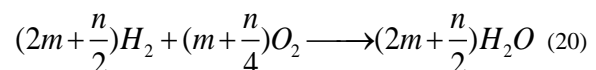
Steam reforming of fuel in the reformer is an endothermic reaction (energy consuming reaction):



The Gas shift reaction, this is an exothermic reaction (energy producing reaction):



Fuel cell reaction:



It is noted that the amount of steam generated by the fuel cell is sufficient for the reformation of the hydrocarbon. It is assumed that the heat enquired for the steam reformer (SR) is provided by the preheating of the fuel and steam input to the reformer and through the heat generated in the water gas shift (WGS) reaction.

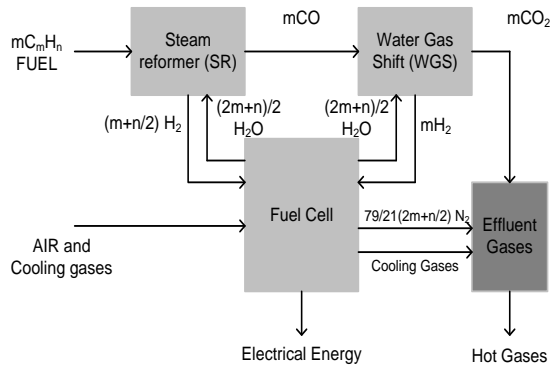


Figure 8. flow chart of the flow of gases in a self reforming fuel cell system

A flow chart of the flow of gases in an internally reforming fuel cell system. The molar weight of the fuel is: $M = 12m + n$ (g/mole), while the molar weight of Carbon dioxide is 28 g/mole. (Larminie and Dicks 2003)

The electrical current can be calculated on the bases of the number of electrons available which is (n) electrons. This is based on the assumption that all the hydrogen in the fuel has been extracted.

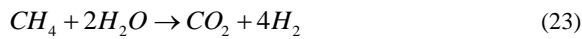
The proposed solid oxide fuel cell (SOFC) uses methane (CH₄) (molar weight = 16 g/mole) as the fuel. The steam reforming reaction (SR) for this fuel is given below (Larminie and Dicks 2003):



Gas shift reaction (GS)



From this reaction; hydrogen is utilised in the fuel cell and carbon dioxide is emitted to the environment. Summation of equations (21) and (22) yields:



Hydrogen is utilised in the fuel cell to produce water and electricity as well as heat output:



Which means that for each mole of methane, one mole of carbon dioxide is produced, in terms of mass: for each 16 g of methane an amount of 28 g of carbon dioxide is produced. The amount of carbon dioxide emissions is a direct factor of efficiency of the system.

Methane is supplied as fuel to the fuel cell with energy content of 1000 kJ/s (1 MW). The fuel has the design point efficiency of 55%. Hence;

Table 1. Efficiency calculation for the plant

Calculated parameter	Value	Unit or Justification
Electrical output of the fuel cell	550	kJ/s
Heat rejected to the cooling fluid	450	kJ/s
The working temperature of cell	1173	K
The heat exchanger effectiveness	0.8	Ratio
Heat available to the gas turbine	450	kJ/s
Cycle pressure ratio	12:1	Ratio
Turbine entry temperature	1173	K
The mass flow rate of air in the closed cycle	0.7	kg/s
The output of the gas turbine	160	kJ/s
Total output	710	kJ/s
The overall energy utilisation efficiency	71 %	(550 + 160)/1000

It should be noted that the effectiveness of the heat exchanger was used for calculating the mass flow of air in the closed cycle gas turbine.

Using the calculated value of the efficiency of the hybrid system, and a value of 35% for the IC engine, the information presented above in equation (23) is used to calculate CO₂ emissions for both systems.

Carbon dioxide emissions vs. power output are shown in Fig. 9 for the proposed hybrid power plant and for conventional combustion. It should be remembered that for a given power output, the amount of fuel used depends on the efficiency of the energy conversion process. The hybrid plant proposed in this paper has reached energy utilisation efficiency of 71%. The combustion engine, at best, may reach an efficiency of 45%. Hence, the hybrid can reduce emissions almost to half the level of combustion engines.

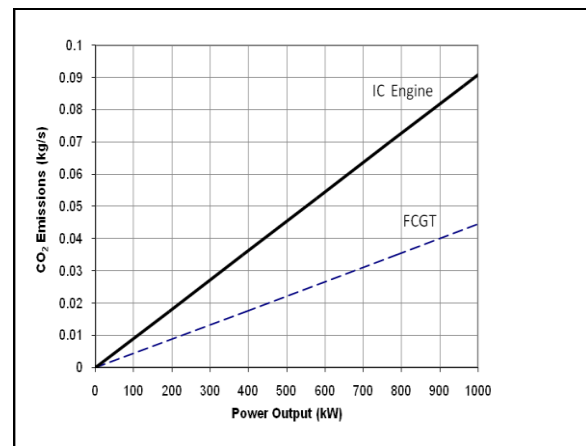


Figure 9. Emission of CO₂ vs. power output (kg/kW. s)

Conclusions

1. The potential of a hybrid power plant comprising a solid oxide fuel cell and a closed cycle gas turbine has been studied. The results show that the combined plant efficiency can be raised to 71%.
2. The emission of greenhouse gases (CO and CO₂) from any plant depends primarily on the mass of fuel consumed per kW which, in turn, depends on the efficiency of converting the chemical energy (kJ/kg) of the fuel into electricity. Therefore, reduction in emissions would be directly proportional to the increase in efficiency. The results of this study confirm this hypothesis.
3. Since the energy utilisation efficiency is defined as the (energy converted to electricity/energy available in the fuel). The unavailable energy is converted to heat; rejection of that heat creates thermal loading on the environment. Therefore, thermal loading would reduce as efficiency increases. Since the efficiency of the hybrid plant has risen to 71%, there would be corresponding reduction in thermal loading.
4. At long last, the disastrous consequences of carbon emission are being taken seriously. Urgent steps are needed to bring carbon emissions under control in order to meet the targets set by the United Nations. This paper has shown the technical feasibility of a hybrid

plant which can achieve drastic reduction in carbon emissions.

References

- [1] Bhinder, F. S., M. Ebaid, et al.. "Parametric study of the fuel cell-gas turbine combined cycle power plant". Proceedings of TURBO EXPO. Barcelona, Spain, ASME, 2006.
 - [2] Calise, F., M. D. d. Accadia, et al. "Full load synthesis/design optimization of a hybrid SOFC-GT power plant." *Energy* 32 (4): 446-458,2007.
 - [3] Kuchonthara, P., S. Bhattacharya, et al. . "Combinations of solid oxide fuel cell and several enhanced gas turbine cycles." *Journal of Power Sources* 124 (1): 65-75, 21003
 - [4] Larmine, J. and A. Dicks . *Fuel Cell Systems Explained*. Chichester, John Wiley & Sons Ltd, 2003
 - [5] Mustafa, M. *Design and Manufacturing of a PEM Fuel Cell*. UK, Coventry University. PhD Thesis: 220,2009
 - [6] Park, S. K., K. S. Oh, et al. "Analysis of the design of a pressurized SOFC hybrid system using a fixed gas turbine design." *Journal of Power Source* 170 (1): 130-139,2007
 - [7] Santin, M., A. Traversoa, et al. "Liquid fuel utilization in SOFCnext term hybrid systems." *Applied Energy* 86 (10): 2204-2212,2009
 - [8] Zhang, X., S. H. Chan, et al. "A review of integration strategies for solid oxide fuel cells." *Journal of Power Sources* 195 (3): 685-702,2010.
- [9]
- [10]

Decision Making Using Multiple Rates of Return: An Alternative Approach

Ahmad Jaradat ^{a,*} and Khaldoun K. Tahboub ^b

^a Industrial Engineering Department, Faculty of Engineering & Technology, University of Jordan, Amman, Jordan.

^b Mechanical and Industrial Engineering Department, Faculty of Engineering, Applied Science University, Amman, Jordan. On leave from Industrial Engineering Department, University of Jordan.

Abstract

Internal rate of return (IROR) method as a decision making tool receives widespread use and acceptance in economic analysis. When performing economic analysis using IROR method, multiple rates might exist, in such cases these rates might be misleading. This research aims at presenting a realistic approach for resolving the multiple rate of return (MROR) problem. A Proposed approach is presented and illustrated through demonstrative cases. The key advantage of the proposed approach is that it reflects real life opportunities and its decisions are consistent with worth methods as well as with other approaches. Relevant approaches of well-known authors are presented discussed and critiqued.

© 2011 Jordan Journal of Mechanical and Industrial Engineering. All rights reserved

Keywords: Internal rate of return, external reinvestment rate, return on internal investment, and multiple rates of return.

1. Introduction

Economic analysis is inevitably an important tool in the decision making process. One engineering economy aspect is devoted to decision making among alternatives. When comparing mutually exclusive alternatives, the main commonly methods used as a basis for comparison are worth methods such as present worth (PW), annual worth (AW), and future worth (FW). Except for the payback period method, other methods such as PW, AW, FW, rate of return (ROR), and benefit-cost ratio (B/C) provide consistent results in terms of the best decision. These methods are widely used but with different preferences in organizations of different forms and types since each method has its own merits of advantages and disadvantages.

The main advantage of worth methods is that they are an absolute measure of investment. On the contrary, ROR and B/C ratio methods ignore the scale of investment and each is used only as an index for profitability in making the accept/reject decisions. This explains why worth methods are applicable on both total and incremental basis, while both ROR and B/C ratio are applicable only on incremental basis.

The key advantage of the ROR method is its widespread acceptance by industry [1, 2]. Decision makers and financial managers prefer ROR analysis to PW method because they find it intuitively more appealing to analyze investments in terms of percentage ROR rather than in PW

[3]. This paper aims at presenting a practical solution to the multiple rate of return (MROR) problem taking into consideration real life practices.

2. Literature Review

Although some difficulties are encountered in solving certain types of cash flows for ROR, it is the most widely used method that has wide acceptance and preference especially in industry and business sectors; it is intuitively appealing and understood.

There are several definitions for ROR, however, all are the same in spirit, since the same set of equations are used in solving for ROR; net worth of cash flow (i^*) = 0. The first is a mathematical definition: ROR is the breakeven interest rate i^* , which makes the worth of cash outflows equal to the worth of cash inflows of the same project.

The second definition is concerned with loan transactions: ROR is the interest paid on the unpaid balance of a loan such that the payment schedule making the unpaid loan balance equal to zero when the final payment is made. This always complies with reality, and its cash flow has a single internal ROR (IROR) simply because loan transactions are based upon a predefined and agreed (contracted) interest rate usually minimum attractive rate of return (MARR) for the lender paid on the unpaid balance of the loan.

* Corresponding author. Jaradat_ahmad@yahoo.com

The third definition is concerned with project return: ROR is the interest rate charged on the un-recovered project balance of the investment such that, when the project terminates, the un-recovered project balance will be zero [3, 4]. This definition is not always consistent with reality, simply because projects' cash flows are mainly based upon feasibility studies and future expectations or contracts rather than a predefined or agreed upon interest rate, where cash flows may reverse signs more than once, which explains the possibility that MROR might exist.

The major difficulty encountered with the ROR method is the occurrence of MROR. Different authors presented different perspectives about MROR. When there are MROR, none of them should be considered a suitable measure for the ROR or attractiveness of the cash flow [5]. MROR are not meaningful for decision making purposes, it is likely that none is correct [1, 2], some of the MROR values seem ridiculous and difficult to use in practical decision making [6]. MROR fail to provide an appropriate measure of profitability for an investment project [3], controversial [7], constitute severe drawbacks [8], unreasonable [9], and there is no rational means for judging which of them is most appropriate for determining economic desirability [10]. In [11, 12] contrary to previous consensus, stated that MROR, even complex-valued each has a meaningful interpretation as a ROR. Next, a new approach for dealing with MROR is presented.

3. Methodology

External reinvestment rate (EIR) is the interest rate at which released (receipts) money from the project over its life can be reinvested. The reinvestment rate in reality represents the opportunity cost usually MARR. "EIR is the interest rate at which the money can in fact be invested outside the project" [4].

The key point of the proposed methodology is based on calculating the return on actual capital portions that remain invested internally, while cash released (receipts) from the project is reinvested externally at EIR. The following represent the steps of the proposed approach:

Step 1

All positive cash flows (released money) that are followed by the first negative cash flow, say at the end of period (m) are invested at EIR to be returned to the project at the end of period (m).

Step 2

If the compound amount at the end of period (m) resulting from step 1 is negative, then the negative value indicates that it is a portion of invested capital, and

remains negative at that point of time. But if the compound amount is positive, then it will be invested again at EIR with the next negative value of cash flow since it represents actual money at hand (released money).

Step 3

Step 1 and step 2 are repeated until there are no more negative cash flows that are preceded by positive cash flows.

Step 4

All remaining positive cash flows that are preceded by negative cash flows are invested at the reinvestment rate and compounded with the last positive cash flow in the project. Now, the project cash flow has either no sign changes or only one sign change. If the cash flow has no sign changes, it means that there is no ROR.

Step 5

Solve the modified cash flow for (i^*).

4. Case Studies

Ten cases will be studied and compared with other known approaches. The first case is next discussed in detail. The same analysis applies for all others.

Consider the following CF and assume that the received money from the project earns 10% interest, i.e. MARR is 10%. This CF has three sign changes, hence, MROR might exist.

Table 1: Cash flow for 1st case.

EOY	0	1	2	3	4	5
CF	-75	250	-100	-500	400	150

As discussed earlier, positive CF at EOY 1 of 250, is reinvested to EOY 2 using EIR of 10%. This available fund is returned to the project at the EOY 2. Hence, the compound amount at the EOY 2 equals $\{250 \times (F/P, 10\%, 1) - 100\}$, which is +175.

Now, the available +175 will be reinvested again externally at EIR of 10% to be returned to the project at the EOY 3. The compound amount at EOY 3 equals $\{175 \times (F/P, 10\%, 1) - 500\}$, which is -307.5. The negative sign indicates that the amount -307.5 is a portion of the invested capital.

At EOY 4, available funds released from the project, i.e. 400, will be externally invested at EIR of 10% to EOY 5. Compound amount at EOY 5 is equal to $\{400 \times (F/P, 10\%, 1) + 150\}$, which is 590. Now the modified cash flow has one sign change, which means that there exists either zero or one positive ROR.

Table 2: Modified cash flow for 1st case.

EOY	0	1	2	3	4	5
CF	-75	0	0	-307.5	0	590

Solving for $i^* \cong 16.94\%$. Comparison of this result with [1, 3-5] is shown in Table (3):

Table 3: Comparison of results for the 1st cash flow.

No.	Approach	$i^* \%$
1	proposed	16.94
2	Newnan	17.41
3	Sullivan	12.14
4	Park	25.60

Table 4 shows the cash flows for all cases along with the 1st case.

Table 4: Cash flows for the ten cases using the proposed approach.

CF No.	EOY												EIR%	
	0	1	2	3	4	5	6	7	8	9	10	11		12
1	-75	250	-100	-500	400	150	-	-	-	-	-	-	-	10
2	30	-60	50	-80	20	70	-	-	-	-	-	-	-	10
3	-40	30	22.5	15	7.5	0	-7.5	-15	-22.5	-	-	-	-	12
4	20	60	-100	-100	0	50	60	0	-150	100	130	-	-	6
5	50	-80	100	0	-300	0	150	0	200	0	-30	0	-50	10
6	-500	300	300	300	-600	200	135.66	-	-	-	-	-	-	6
7	0	100	200	-600	-200	300	300	-50	-	-	-	-	-	15
8	-100	330	-362	132	-	-	-	-	-	-	-	-	-	12
9	-100	380	-527	313	-66	-	-	-	-	-	-	-	-	15
10	20	60	-100	-100	0	50	60	0	-150	100	130	-	-	15

5. Discussions

The proposed approach provides realistic results when compared with other known approaches. It is based upon a simple real life practiced fact that cash released (generated) from the project is reinvested externally at the best available rate at that time which is the EIR (usually MARR) since it is actual cash money at hand with the investor, and returned to the project (wholly or partially) when needed. In this approach the true IROR on money actually invested in the project is computed.

Worth methods assume implicitly that both cash outflows and inflows are reinvested at MARR during the

study period, while *ROR method* assumes that both cash outflows and inflows are reinvested at *IROR*, which might not be realistic for some problems, hence may not be valid. The reinvestment assumption of the IROR method noted previously may not be valid in an engineering economy study [1, 2]. There can be no particular reason why we would assume that the external investments earn the same ROR as internal investments [4, 5]. In reality, it is not always possible for cash borrowed (released) from a project to be reinvested to yield a rate ROR equal to that received from the project [3]. Table (5) shows comparison results of the proposed approach with [2-4].

Table 5: Comparison of proposed approach results with others.

Approach	$i^* \%$ for the different cash flows									
	1	2	3	4	5	6	7	8	9	10
proposed	16.94	20.00	12.17	8.87	10.27	8.40	13.72	12.00	15.00	13.31
Newnan	17.41	20.90	13.03	9.081	10.67	11.10	12.73	12.00	15.00	13.15
Sullivan	12.14	12.53	12.12	6.804	9.73	7.26	14.67	12.00	15.00	14.58
Park	25.6	23.90	13.03	9.081	11.35	13.13	12.73	12.00	15.00	12.41

In finding (i^*), Table (5), [3] discounted the project balance (PB) if positive at MARR, while discounting PB if negative at IROR even though the cash flow may be positive at that time. This might not always be realistic simply because PB is not an available fund at hand of the investor. A realistic case that complies with this approach is loan transactions, not because the approach itself, but because of the nature of loan transactions where it is contracted in real life on the basis of a predefined (agreed upon) interest rate that should be paid on the unpaid balance also because of the stability of the interest rate being agreed upon. [4, 5] approaches in essence are the same as [3], though different expressions and terminology have been used, hence, same comments apply.

In [1, 2] approach for finding (i^*), Table (5), all cash receipts from the project are compounded to period N (the future) at EIR, ignoring the possibility that some of these funds may be returned to the project when needed. Also, all disbursements are compounded to time zero (the present) at EIR, again ignoring the fact that some of these disbursements (or portions) should be discounted at IROR and not at EIR. Next, solving the resulting balanced CF for ERR to be compared with firm's MARR in making the accept/reject decision, which might not comply with real life opportunities. If a firm needs to know what ROR will be achieved it is unclear what does the calculated ERR represents in reality. The main advantage of his approach is that it always has a single ERR that works as an index for profitability and consistent with worth methods in making the accept/reject decision.

6. Conclusions

ROR method is a powerful tool in making accept/reject decisions. The term ROR is intuitively appealing and understood and has widespread acceptance in business and organizations. It is routinely used in daily financial transactions.

The proposed approach is reliable, and reflects the real life opportunities simply because it calculates the return on actual capital portions that remain invested internally while cash released from the project is reinvested

externally at the only available rate (real life) at that point of time which is the EIR.

So the proposed approach presents more than a mathematical solution or remedy; hence the calculated ROR is reliable, trusted and beside its simplicity, its decisions are always consistent with worth methods as well as with other approaches.

Even projects that have a single ROR, the proposed approach can be applied since it completely consistent with real life practices.

References

- [1] Sullivan, W. G.; Wicks E. M.; and Luxhoj, J. T., Engineering Economy, 13th Edition. Prentice-Hall, New Jersey, 2006.
- [2] Sullivan, W.G., Wicks, E.M., and Koelling, C.P., Engineering Economy, 14th ed., Prentice-Hall, 2009.
- [3] Park, C. S., Contemporary Engineering Economics, 3rd Edition. Prentice-Hall, New Jersey, 2010.
- [4] Newnan, D.G., Whittaker, J., Eschenbach, T.G., and Lavelle, J.P., Engineering Economic Analysis, Engineering Press, 2nd Canadian ed., 2010.
- [5] Newnan, D. G., Engineering Economic Analysis, 6th Edition. Engineering Press, San Jose, California, 2004.
- [6] Blank, L. T. and Tarquin, A. J., Engineering Economy, 5th Edition. McGraw-Hill, New York, 2005.
- [7] Steiner, H. M., Engineering Economic Principles, 2nd Edition. McGraw-Hill, New York, 1992.
- [8] White, J. A.; Case, K. E.; Pratt, D. B.; and Agee, M. H., Principles of Engineering, Economic Analysis, Wiley, New York, 1998.
- [9] Cannaday, R. E.; Colwell, P. F.; and Paley, H., "Relevant and Irrelevant Internal Rates of Return. Engineering Economist, Vol. 32, pp. 17-38, 1986.
- [10] Thuesen, G. J. and Fabrycky W. J., Engineering Economy, 9th Edition. Prentice-Hall, Englewood Cliffs, New Jersey, 2001.
- [11] Hazen, G. B., A new Perspective on Multiple Internal Rates of Return. The Engineering Economist, Vol. 48, pp. 31-51, 2003.
- [12] Hartman, J.C. and Schafrick, IC., The Relevant Internal Rate of Return, Engineering Economist, summer 2004.



الجامعة الهاشمية



المملكة الأردنية الهاشمية

المجلة الأردنية
للهندسة الميكانيكية والصناعية

JJIMIE

مجلة علمية عالمية محكمة

<http://jjmie.hu.edu.jo/>

ISSN 1995-6665

المجلة الأردنية للهندسة الميكانيكية والصناعية

مجلة علمية عالمية محكمة

المجلة الأردنية للهندسة الميكانيكية والصناعية: مجلة علمية عالمية محكمة تصدر عن عمادة البحث العلمي والدراسات العليا في الجامعة الهاشمية بالتعاون مع صندوق دعم البحث العلمي في الأردن.

هيئة التحرير

رئيس التحرير:

الأستاذ الدكتور موسى محسن
قسم الهندسة الميكانيكية، الجامعة الهاشمية، الزرقاء، الأردن .

الأعضاء:

الأستاذ الدكتور عدنان الكيلاني الجامعة الأردنية	الأستاذ الدكتور بلال العكش الجامعة الهاشمية
الأستاذ الدكتور أيمن المعاينة جامعة مؤتة	الأستاذ الدكتور علي بدران الجامعة الأردنية
الأستاذ الدكتور محمد النمر جامعة العلوم والتكنولوجيا الأردنية	الأستاذ الدكتور نسيم سواق جامعة مؤتة

مساعد رئيس هيئة التحرير:

الدكتور أحمد الغندور
الجامعة الهاشمية

فريق الدعم:

تنفيذ وإخراج
م. أسامة الشريط

المحرر اللغوي
الدكتور عبدالله جرادات

ترسل البحوث إلى العنوان التالي :

ترسل البحوث إلى العنوان التالي:
رئيس تحرير المجلة الأردنية للهندسة الميكانيكية والصناعية
عمادة البحث العلمي والدراسات العليا
الجامعة الهاشمية
الزرقاء - الأردن

هاتف : 00962 5 3903333 فرعي 4147

Email: jjmie@hu.edu.jo

Website: www.jjmie.hu.edu.jo